ISSN (print) 0205-9614
ISSN (online) 3034-5405

Российская Академия Наук

No. 1 January-February 2025

ЖУРНАЛ РОССИЙСКОЙ АКАДЕМИИ НАУК

ИССЛЕДОВАНИЕ ЗЕМЛИ ИЗ КОСМОСА

EARTH RESEARCH FROM SPACE

NAUKA
1727

Russian Academy of Sciences

ИССЛЕДОВАНИЕ ЗЕМЛИ ИЗ КОСМОСА / EARTH RESEARCH FROM SPACE

No. 1 2025 January - February

Founded in 1980.
Published bimonthly.
ISSN (print) 0205-9614
ISSN (online) 3034-5405

The journal publication is guided by the Presidium of the Russian Academy of Sciences

Editorial office: Moscow, 119991, Leninsky pr., 14;
tel.: +7(495) 632-16-54, +7(495) 632-11-78;
e-mail: izk.journal1980@gmail.com;
Web: http://www.jizk.ru

Moscow
"Nauka" Publishers"

CONTENTS

No. 1, 2025

Using Satellite Information about the Earth

EARTH RESEARCH FROM SPACE, 2025, No. 1, pp. 3–14

USING SATELLITE INFORMATION ABOUT THE EARTH

VERTICAL STRUCTURE OF THE ANTARCTIC POLAR VORTEX DURING SUDDEN STRATOSPHERIC WARMINGS IN 1988, 2002 AND 2019 ACCORDING TO SATELLITE OBSERVATIONS

© 2025 V. V. Zuev[a], E. S. Savelieva[a, b, *], and A. V. Pavlinsky[a]

[a] *Institute of Monitoring of Climatic and Ecological Systems of the Siberian Branch of the Russian Academy of Sciences, Tomsk, Russia*

[b] *A. M. Obukhov Institute of Atmospheric Physics of the Russian Academy of Sciences, Moscow, Russia*

**e-mail: esav.pv@gmail.com*

Received June 03, 2024

Abstract. Using the MERRA-2 satellite data and ERA5 reanalysis data, we examined the vertical structure of the Antarctic polar vortex during the sudden stratospheric warming events (SSWs) of 1988, 2002 and 2019. The significant displacements of the polar vortex were observed in 1988 and 2019, and the vortex splitting occurred in 2002. Differences in the vertical dynamics of the Antarctic polar vortex during SSWs recorded due to displacement (1988 and 2019) or vortex splitting (2002) are shown. The weakening, displacement and subsequent breakdown of the polar vortex in 1988 and 2019 was observed first in the upper stratosphere, and then gradually spread into the middle and lower stratosphere within a month. Thus, the SSW in the lower stratosphere was preceded by a significant displacement of the polar vortex in the upper stratosphere a month before the event. While in 2002, before the split, the polar vortex was strong and stable at all stratospheric levels, the split was observed simultaneously in the middle and upper stratosphere, after which the vortex collapsed in the upper stratosphere, and existed for another month in the lower and middle stratosphere. In all cases, a decrease in wind speed along the vortex edge, an increase in temperature inside the vortex, melting of particles of polar stratospheric clouds and a decrease in ozone hole area were observed starting in late August. The earlier recovery of ozone hole occurred on 30 October 1988, 9 November 2002 and 6 November 2019, respectively.

Keywords: *Antarctic polar vortex, sudden stratospheric warming, polar stratospheric clouds, dynamic barrier*

DOI: 10.31857/S02059614250101e1

INTRODUCTION

Stratospheric polar vortices formed over polar regions in late spring are large-scale cyclonic formations propagating from the tropopause into the mesosphere and existing through spring (Waugh and Polvani, 2010; Waugh et al., 2017). The persistence of the polar vortex during the winter-spring period determines the extent and depth of the spring polar ozone depletion (Newman et al., 2004). The boundaries of the polar vortex represent a dynamic barrier preventing the meridional transport of stratospheric ozone from tropical and middle latitudes to the polar region (Manney et al., 2022). At the same time, polar stratospheric clouds (PSCs) are formed inside the polar vortex at extremely low temperatures (< -78 °C), on the surface and in the volume of which heterogeneous reactions with the release of molecular chlorine occur. When solar radiation appears over the polar region, molecular chlorine photodissociates to form chlorine radicals, which enter the catalytic cycle of ozone destruction (Solomon, 1999).

Sudden stratospheric warming (SSW) is an abrupt warming in the polar stratosphere as a result of strong displacement or splitting of the stratospheric polar vortex by vertically propagating planetary waves (Ayarzagüena et al., 2019). Planetary waves propagate into the middle stratosphere where they move in an easterly direction opposite to the westward motion of the polar vortex, resulting in perturbation of the polar vortex and its subsequent displacement or splitting accompanied by SSW (Kuttippurath and Nikulin, 2012). The Arctic polar vortex is almost annually affected by planetary waves, marked by SSW (Ageyeva et al., 2017). In turn, in the Antarctic, during the period from 1979 to 2023, the SSW was recorded only three times. SSW was

recorded only three times — in 1988, 2002, and 2019 (Roy et al., 2022). The first of these is often not taken into account in the statistics of SSW events over Antarctica, because the significant displacement of the polar vortex in 1988 was observed during its weakening phase with decreasing area. However, the polar vortex dynamics in 1988 and 2019 have many similarities, with the second one being a recognized SSW event (Safieddine et al., 2020; Kogure et al., 2021; Noguchi et al., 2020).

An earlier weakening and destruction of the Antarctic polar vortex in the spring of 2019 was considered in a number of papers (Goncharenko et al., 2020; Klekociuk et al., 2021; Eswaraiah et al., 2020; Shen et al., 2022). An anomalous weakening of the polar vortex in 2019 was observed from September through October, followed by a recorded SSW in early November and subsequent vortex collapse in the first half of November, about a month earlier than the 40–year average (Wargan et al., 2020; Milinevsky et al., 2019). The dynamics of the weakening of the polar vortex in 2019 was comparable to the dynamics of the vortex in 2002, when its splitting occurred (Lim et al., 2021). In 2002, the Antarctic polar vortex splitting and subsequent SSW were observed on September 25 (Newman and Nash, 2005; Stolarski et al., 2005; Hoppel et al., 2003; Grooß et al., 2005). An irreversible character in the dynamic changes of the polar vortex in spring 2002 was observed from the second part of September, with the first signs of subsequent changes observed already from the end of August (Charlton et al., 2005; Feng et al., 2005; Manney et al., 2005). The dynamics of the polar vortex in the spring of 1988 had a similar nature of weakening as in 2019, with the vortex shift signaled by the SSW observed in the first days of November (Hirota et al., 1990; Grytsai et al., 2008). The aim of this work is to investigate the vertical structure of the Antarctic polar vortex during the 1988, 2002 and 2019 SSWs, as well as the dynamics of the PSCs and ozone hole from satellite observations.

DATA AND METHODS

Daily averages of zonal wind speed at 60°S, minimum temperature in the 50–90°S region at 50 hPa, PSC volume in the 60–90°S region, and ozone hole area (an area characterized by total ozone content (TOC) values below 220 DU) in the 40–90°S region from 1983 to 2022 are obtained from the Modern-Era Retrospective analysis for Research and Applications, Version 2 (MERRA-2) archive created by the Goddard Earth Observing System Data Assimilation System (GEOS DAS) based on NASA Goddard Space Flight Center (GSFC) satellite data, http://ozonewatch.gsfc.nasa.gov. MERRA-2 is the first long-term global reanalysis that assimilates space-based observations of aerosols and represents their interactions with other physical processes in the climate system (Gelaro et al, 2017). Daily mean geopotential and zonal and meridional wind speed data for the region 30–90°S with a horizontal resolution of 0.25° × 0.25° at levels between 100 and 5 hPa for 1988, 2002, and 2019 were obtained from the ERA5 European Centre for Medium-Range Weather Forecasts reanalysis (Hersbach et al., 2020), https://doi.org/10.24381/cds.bd0915c6. To analyze the vertical dynamics of the Antarctic polar vortex during the SSW 1988, 2002 and 2019, the fields of geopotential and wind speed at the levels from 100 to 5 hPa were considered in indices. The indices were calculated using the formula (x–y)/y, where x is the value of geopotential (wind speed) at a point, y is the value of geopotential characterizing the polar vortex boundary (the value of wind speed at which the dynamic barrier is formed) at the considered level (Zuev and Savelieva, 2024). The dynamics of the considered parameters in the studied years was compared with the 40–year climatic averages for 1983–2022, obtained with standard deviations of mean (SD, σ) and smoothed FFT-filter for 15 points.

RESULTS, THEIR ANALYSIS AND DISCUSSION

Fig. 1 presents the dynamics of the Antarctic polar vortex characteristics during the winter-spring period of 1988, 2002 and 2019. In all cases, one observed a decrease of the zonal velocity, the minimum temperature increase, a decrease of the PSC volume and the area of the ozone hole beginning from the end of August. Earlier "collapse" of the ozone hole occurred on October 30, 1988, November 9, 2002, and November 6, 2019, respectively. Table 1 shows the averaged September, October and November characteristics of the Antarctic polar vortex in 1988, 2002 and 2019. There was a more significant weakening of the polar vortex in 2002 and 2019 than in 1988: wind speed and PSC volume were on average 40% and 30% lower, despite higher ozone hole area values (Fig. 1, Table 1). Figures 2–7 show the geopotential and wind speed fields in indices at levels from 100 to 5 hPa for dates before, during, and after the 1988, 2002, and 2019 SSW events. In the geopotential fields, the contour marks the inferred polar vortex boundary, and in the wind speed fields, the dynamic barrier (corresponding to the value "0" on the scale in the indices). Table 2 summarizes the values of vortex area and mean wind speed along the vortex boundary for the considered dates before, during, and after the 1988, 2002, and 2019 SSW events at levels from 100 to 5 hPa.

Table 1. Monthly averages of zonal wind speed near 60°S, minimum temperature in the 50–90°S region at 50 hPa, PSC volume in the 60–90°S region, and ozone hole area in the 50–90°S region from September through November 1988, 2002, and 2019

	Zonal wind, m/s			Minimum temperature, °C			PSC volume, 10^7 km^3			Ozone hole area, 10^6 km^2		
	1988	2002	2019	1988	2002	2019	1988	2002	2019	1988	2002	2019
September	48.7	34.4	40.4	−84.2	−85.9	−81.8	14.4	12.8	9.3	9.2	14.3	10.4
October	32.5	22.0	24.9	−73.6	−71.1	−71.6	0.9	0.1	0.2	6.4	7.7	7.9
November	11.0	6.1	4.9	−59.0	−62.7	−62.7	0.0	0.0	0.0	0.0	0.5	0.5

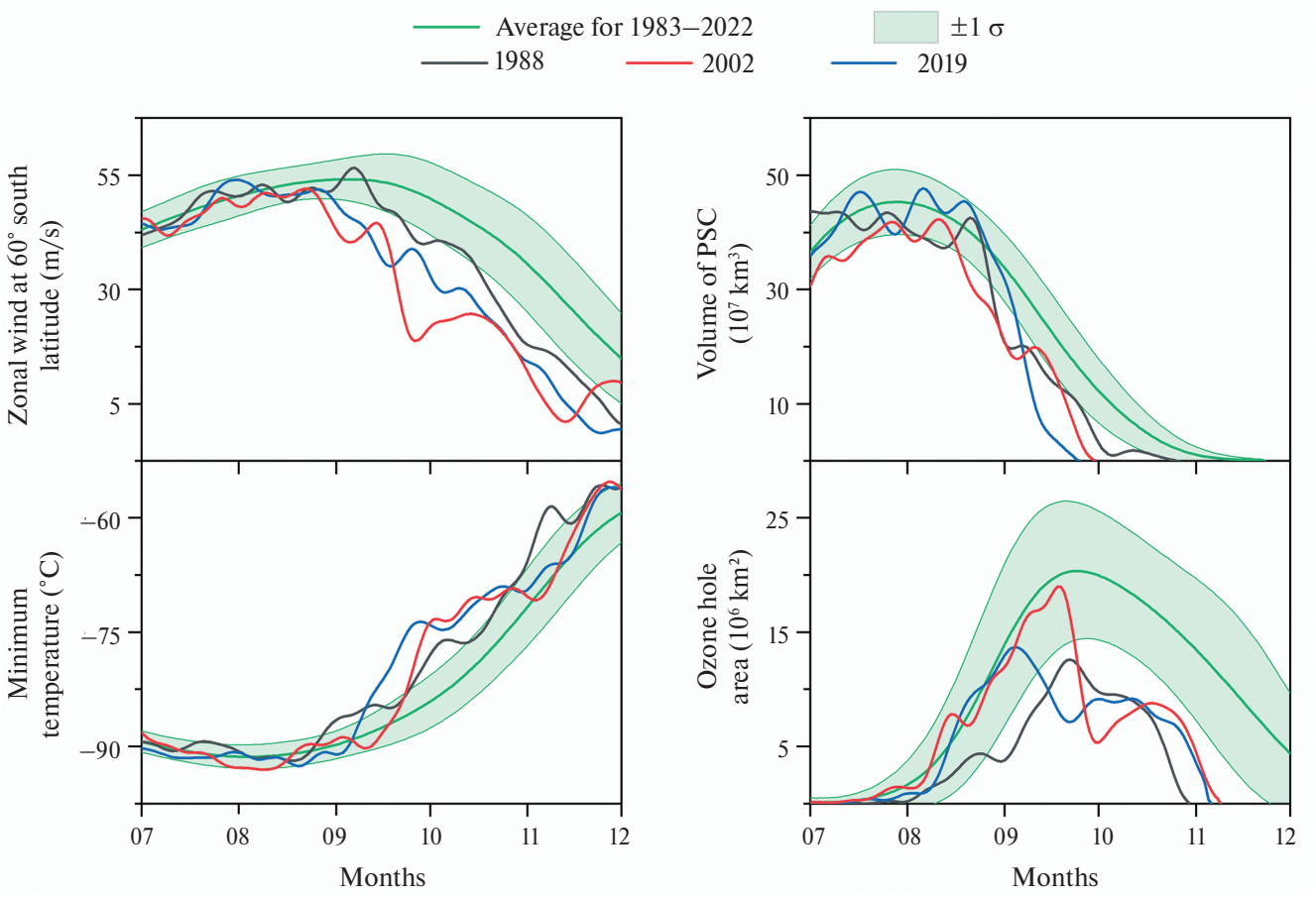

Fig. 1. Intra-annual variations of zonal wind speed near 60°S, minimum temperature in the 50–90°S region at 50 hPa, PSC volume in the 60–90°S region, and ozone hole area in the 40–90°S region from July to November 1988 2002, and 2019 against the 1983–2022 averages with SD (±1 σ).

In spring **1988,** a significant displacement of the polar vortex marked by the SSW was observed on November 1 in the lower stratosphere (Figs. 2, 3). In the middle and upper stratosphere, a significant displacement of the vortex was manifested already in the second part of October, while in early November at the levels of 10 hPa and higher, the polar vortex was no longer traced (Table 2). The weakening of the polar vortex in 1988 began in the first days of October in the upper stratosphere. One can see in Figs. 2, 3 how the displacement and weakening of the polar vortex, which began in the upper stratosphere, gradually

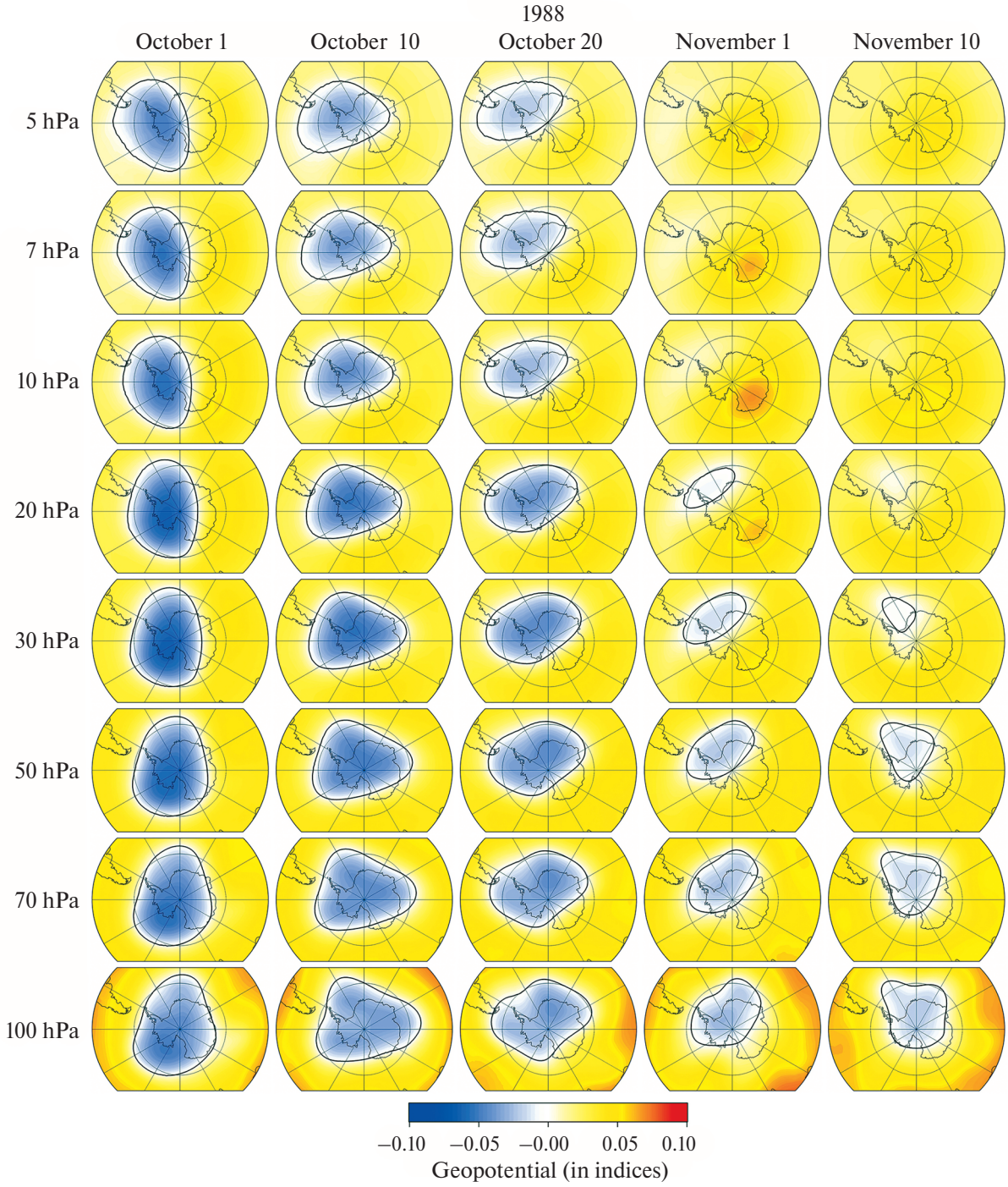

Fig. 2. Geopotential fields at the levels from 100 to 5 hPa over the Antarctic from October 1 to November 10, 1988.

manifested at the levels below until it reached the lower stratosphere in early November.

In the first part of September **2002,** the polar vortex was sufficiently strong and stable and was characterized by a greater area and wind speed along the vortex boundary in the upper and middle stratosphere as compared to the lower stratosphere (Table 2, Figs. 4, 5). On September 25, the vortex splitting occurred in the middle and upper stratosphere (at the levels from 20 hPa and above), with the polar vortex in the lower stratosphere taking the form of a "figure eight". After splitting in the upper stratosphere, a small anticyclone was formed, one of the parts of the polar vortex "dissolved" and the second part gradually collapsed. In its turn

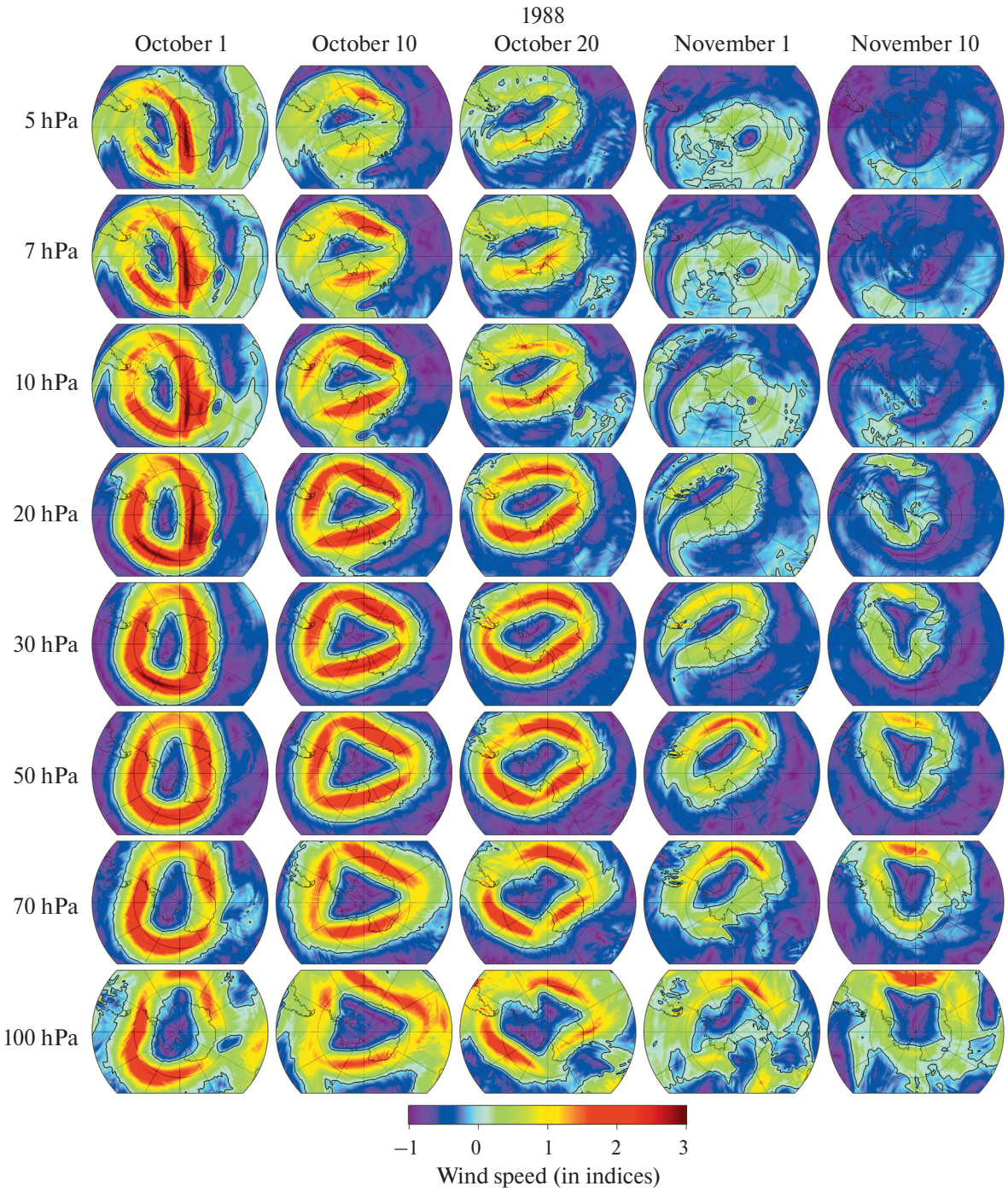

Fig. 3. Wind speed fields at the levels from 100 to 5 hPa over the Antarctic from October 1 to November 10, 1988.

in the lower and middle stratosphere, the polar vortex was partially restored and existed for another month.

The vortex dynamics in the spring of **2019** was to a large extent similar to the dynamics at the SSW of 1988. The vortex weakening and displacement began to manifest in the upper stratosphere as early as in early October and gradually spread to the middle and lower stratosphere (Figs. 6, 7). The SSW was observed on November 1 at the levels of 20 hPa and below, while at the levels from 10 hPa and above a significant displacement of the polar vortex was observed as early as in the second part of October (Table 2, Figs. 6, 7).

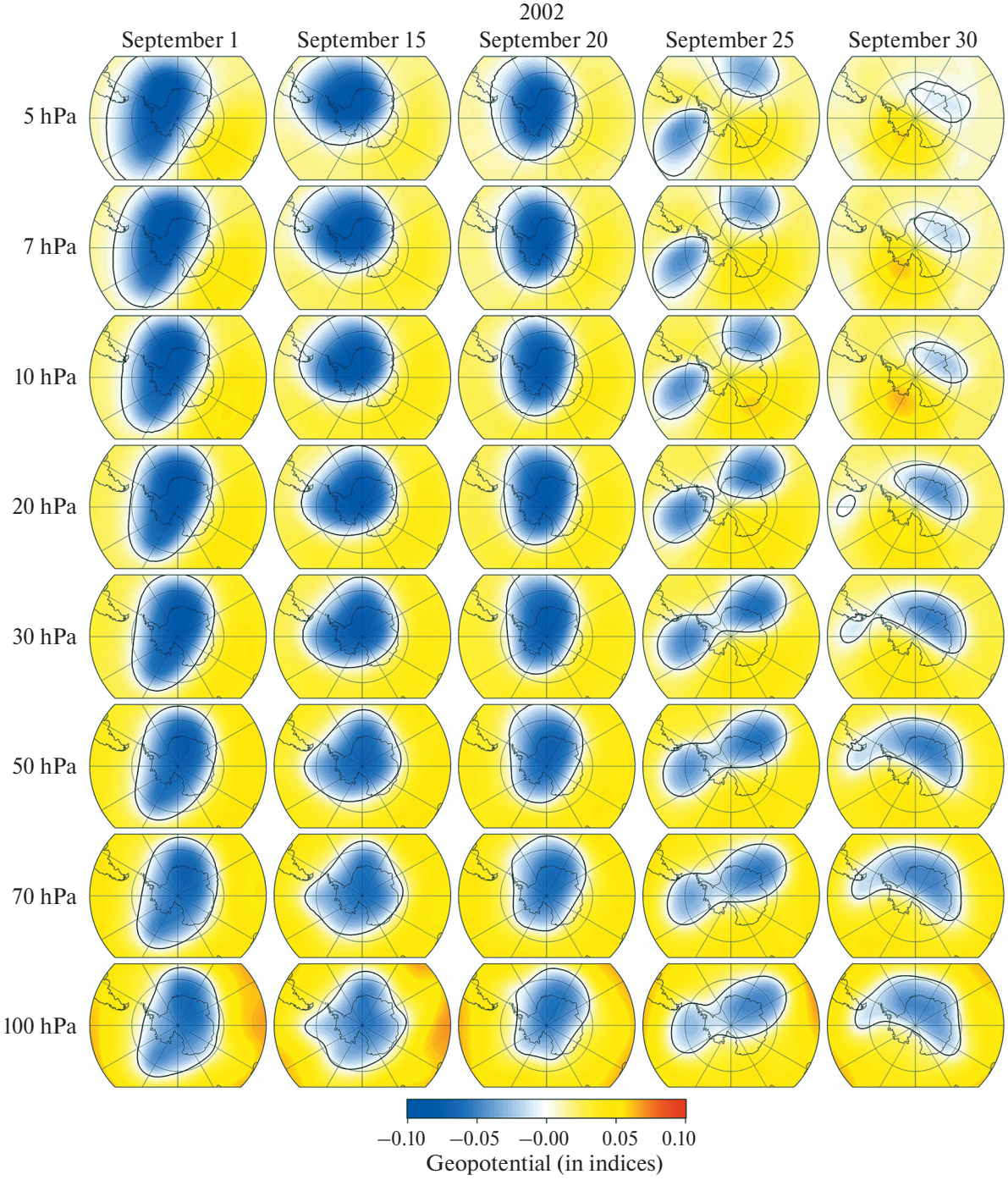

Fig. 4. Geopotential fields at the levels from 100 to 5 hPa over the Antarctic from September 1 to 30, 2002.

CONCLUSION

The paper considers the vertical structure of the Antarctic polar vortex during the SSW 1988, 2002 and 2019 and the dynamics of the PSC volume and the ozone hole area from satellite observations. A significant displacement of the polar vortex was observed in 1988 and 2019, and a cleavage in 2002. The volume of the PSC and the area of the ozone hole are indirect characteristics of the polar vortex dynamics. In the years under consideration, one observed almost simultaneously beginning from the end of August a decrease of wind speed along the

Table 2. Vortex area and mean wind speed along the vortex boundary before, during, and after the 1988, 2002, and 2019 SSWs

	Vortex area, mln. km^2					Wind speed at the vortex boundary, m/s				
	01.10.1988	10.10.1988	20.10.1988	01.11.1988	10.11.1988	01.10.1988	10.10.1988	20.10.1988	01.11.1988	10.11.1988
5 hPa	28.8	26.1	20.7			66.8	49.5	46.4		
7 hPa	28.0	24.8	20.1			66.4	56.7	52.9		
10 hPa	27.1	23.8	19.4			72.3	65.8	54.7		
20 hPa	30.2	28.4	25.3			70.3	69.9	60.8		
30 hPa	31.2	30.2	27.2	11.5		66.1	66.8	60.0	33.8	
50 hPa	32.4	31.7	28.4	14.9	11.7	57.5	57.0	53.6	35.3	22.1
70 hPa	32.9	32.7	28.8	16.5	15.2	50.8	48.6	46.4	31.1	24.3
100 hPa	50.8	50.5	45.4	37.8	36.3	37.9	37.5	35.5	27.8	28.0
	01.09.2002	15.09.2002	20.09.2002	25.09.2002	30.09.2002	01.09.2002	15.09.2002	20.09.2002	25.09.2002	30.09.2002
5 hPa	56.8	40.7	39.2	29.6		59.7	65.8	64.7	66.6	
7 hPa	50.6	38.4	35.3	27.5		62.6	67.9	71.4	70.4	
10 hPa	44.0	35.3	32.2	25.5		69.8	72.5	80.3	72.0	
20 hPa	42.0	35.5	33.7	29.6	16.2	66.8	67.2	75.3	62.4	56.7
30 hPa	40.6	35.2	33.6	30.6	22.2	63.2	63.7	69.2	60.4	57.0
50 hPa	38.9	34.7	32.2	29.8	26.5	56.8	55.0	57.2	54.3	56.6
70 hPa	37.8	34.3	30.5	29.1	27.3	51.3	47.7	49.5	46.9	50.8
100 hPa	54.3	52.1	45.4	46.7	47.1	38.0	35.0	30.8	31.1	30.8
	01.10.2019	10.10.2019	20.10.2019	01.11.2019	10.11.2019	01.10.2019	10.10.2019	20.10.2019	01.11.2019	10.11.2019
5 hPa	22.6	18.2	12.6			45.8	42.7	32.3		
7 hPa	19.3	16.9	12.6			51.8	47.1	37.1		
10 hPa	17.5	15.8	12.2			57.6	53.4	43.0		
20 hPa	21.5	19.9	17.2	11.7		59.7	58.4	52.5	41.1	
30 hPa	23.4	22.1	19.5	14.4		59.3	57.3	51.7	45.0	
50 hPa	25.1	24.6	21.7	16.1	9.2	56.0	54.3	48.9	44.5	31.2
70 hPa	26.0	26.3	23.0	16.3	10.7	52.3	50.2	43.6	37.4	33.0
100 hPa	42.0	42.8	42.1	34.6	27.7	33.2	34.3	28.4	25.4	25.9

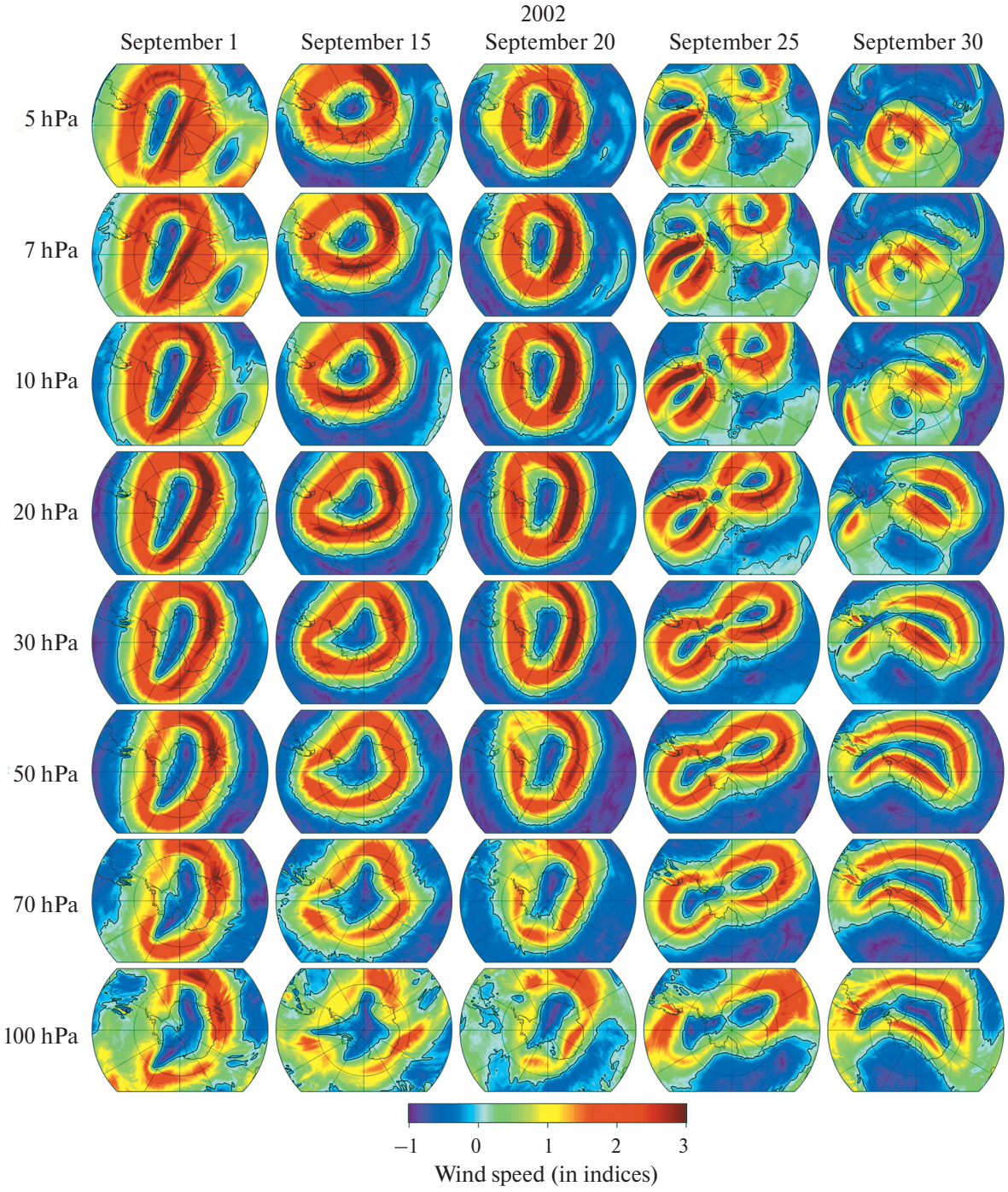

Fig. 5. Wind speed fields at the levels from 100 to 5 hPa over the Antarctic from September 1 to 30, 2002.

vortex boundary, an increase of temperature inside the vortex, destruction of PSC particles and decrease of the ozone hole area. The earlier tightening of the ozone hole occurred on October 30, 1988, November 9, 2002 and November 6, 2019, respectively. At the same time in 2002 and 2019, a more significant weakening of the polar vortex was observed: the wind speed and the PSC volume were on average by 40% and 30% lower than in 1988.

Different trends in the vertical dynamics of the Antarctic polar vortex at SSW recorded due to the displacement (1988 and 2019), or vortex splitting

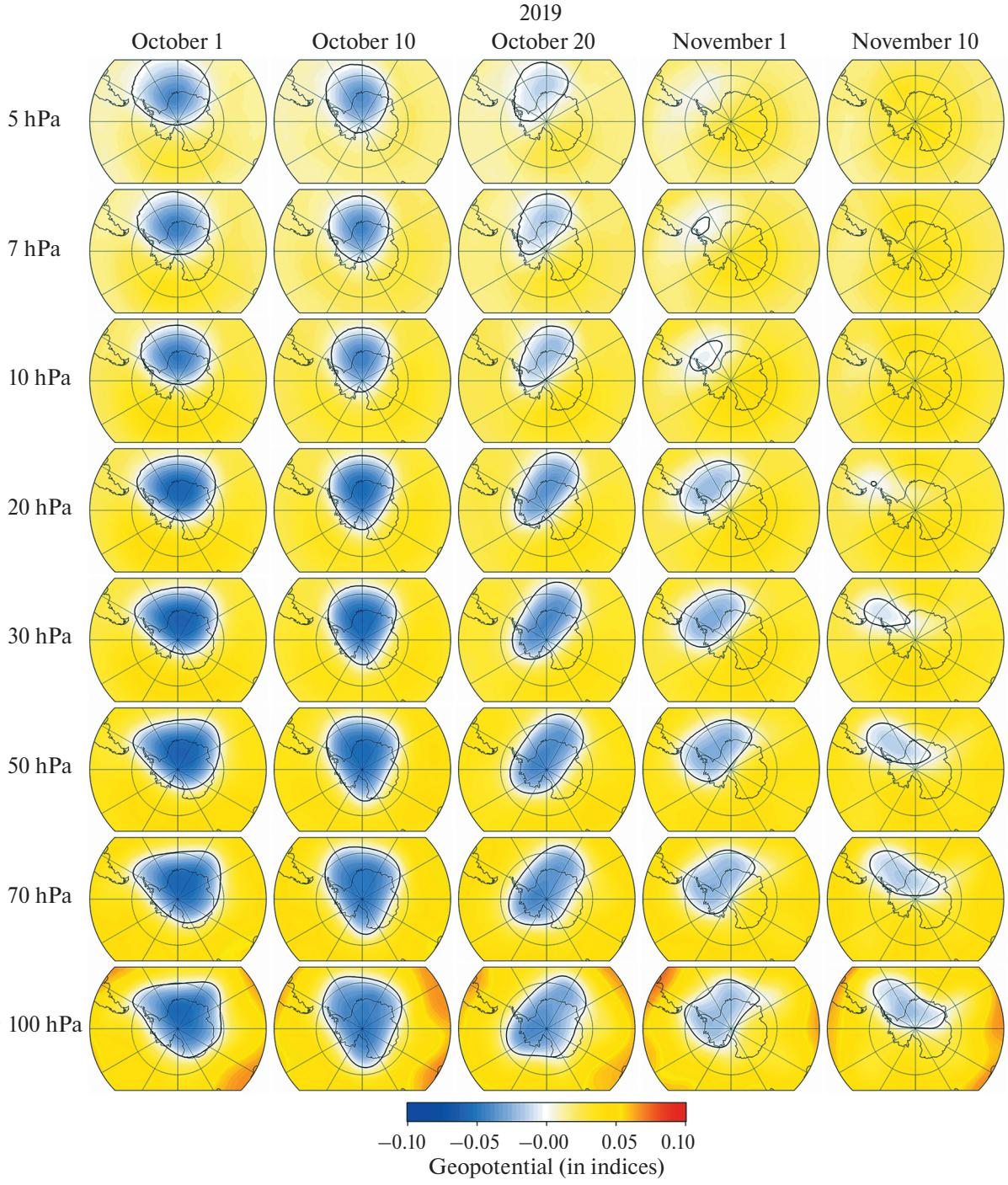

Fig. 6. Geopotential fields at levels from 100 to 5 hPa over Antarctica from October 1 to November 10, 2019.

(2002) were revealed. Weakening, displacement, and subsequent polar vortex breakup in 1988 and 2019 were observed first in the upper stratosphere and then gradually propagated into the middle and lower stratosphere over the course of a month. At the same time, the SSW in the lower stratosphere was preceded by a significant vortex displacement in the upper stratosphere one month before the event. In its turn in 2002 before splitting the polar vortex was sufficiently strong and stable at all stratospheric levels, splitting occurred in the middle and upper stratosphere, after which the vortex collapsed in the upper stratosphere

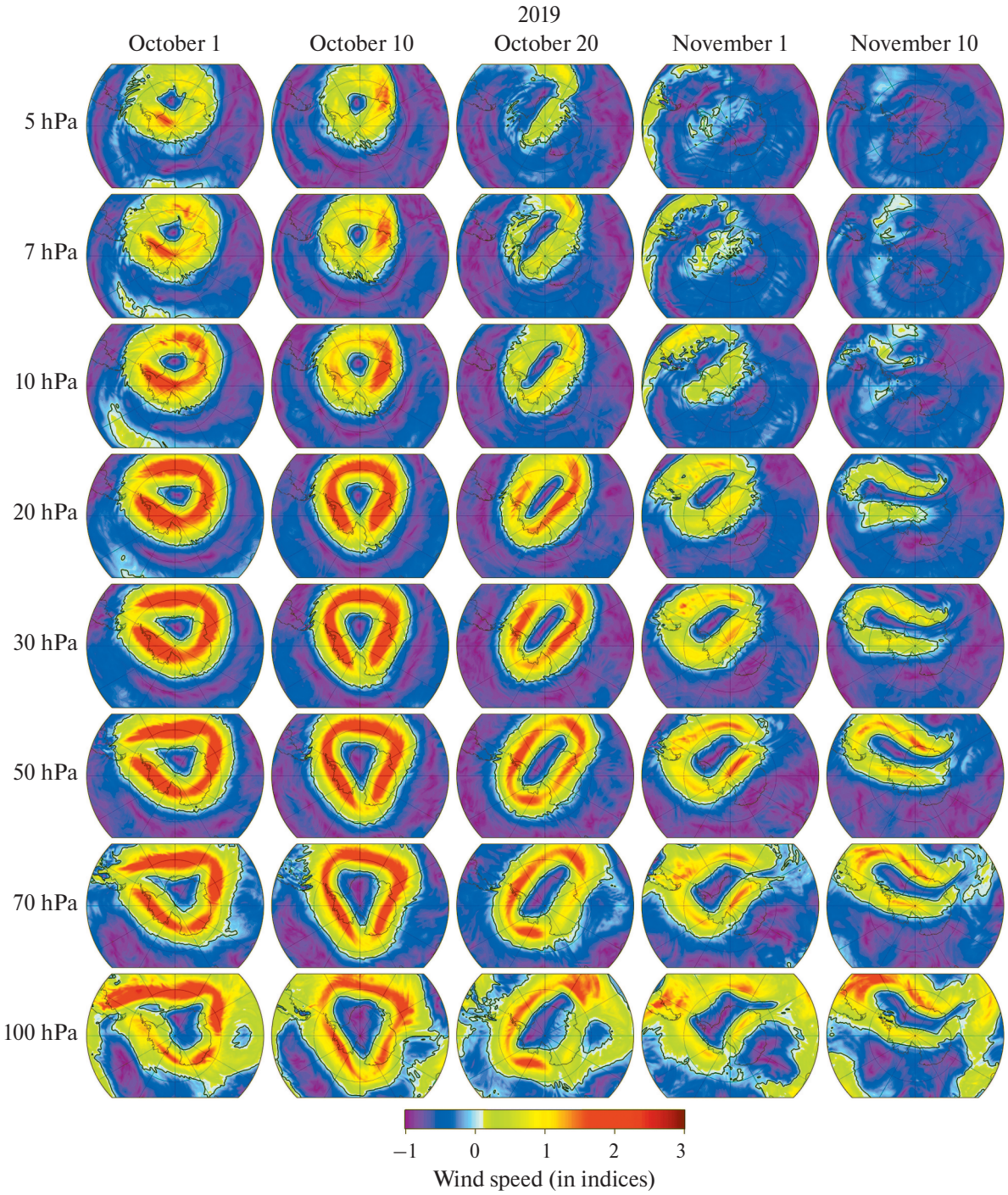

Fig. 7. Wind speed fields at levels from 100 to 5 hPa over Antarctica from October 1 to November 10, 2019.

and existed in the lower and middle stratosphere for another 1 month.

FUNDING

The research was supported by the Russian Science Foundation grant No. 23-17-00273, https://rscf.ru/project/23-17-00273/.

REFERENCES

1. *Ageeva V.Yu., Gruzdev A.N., Elokhov A.S., Mokhov I.I.* Sudden stratospheric warmings: statistical characteristics and impact on the total content of NO_2 and O_3 // Izv. RAS. Atmospheric and Oceanic Physics. 2017. Vol. 53. No. 5. Pp. 545–555. DOI: 10.7868/S0003351517050014. (In Russian).

2. *Ayarzagüena B., Palmeiro F.M., Barriopedro D., Calvo N., Langematz U., Shibata K.* On the representation of major

stratospheric warmings in reanalyses // Atmos. Chem. Phys. 2019. Vol. 19. No. 14. Pp. 9469–9484. DOI: 10.5194/acp-19-9469-2019.

3. *Charlton A.J., O'Neill A., Lahoz W.A., Berrisford P.* The splitting of the stratospheric polar vortex in the Southern Hemisphere, September 2002: Dynamical evolution // J. Atmos. Sci. 2005. Vol. 62. No. 3. Pp. 590–602. DOI: 10.1175/JAS-3318.1.

4. *Eswaraiah S., Kim J.-H., Lee W., Hwang J., Kumar K.N., Kim Y.H.* Unusual changes in the Antarctic middle atmosphere during the 2019 warming in the Southern Hemisphere // Geophys. Res. Lett. 2020. Vol. 47. No. 19. P. e2020GL089199. DOI: 10.1029/2020GL089199.

5. *Feng W., Chipperfield M.P., Roscoe H.K., Remedios J.J., Waterfall A.M., Stiller G.P., Glatthor N., Höpfner M., Wang D.-Y.* Three-dimensional model study of the Antarctic ozone hole in 2002 and comparison with 2000 // J. Atmos. Sci. 2005. Vol. 62. No. 3. Pp. 822–837. DOI: 10.1175/JAS-3335.1.

6. *Gelaro R., McCarty W., Suárez M.J., Todling R., Molod A., Takacs L., Randles C.A., Darmenov A., Bosilovich M.G., Reichle R., Wargan K., Coy L., Cullather R., Draper C., Akella S., Buchard V., Conaty A., da Silva A.M., Gu W., Kim G.-K., Koster R., Lucchesi R., Merkova D., Nielsen J.E., Partyka G., Pawson S., Putman W., Rienecker M., Schubert S.D., Sienkiewicz M., Zhao B.* The Modern-Era Retrospective Analysis for Research and Applications, Version 2 (MERRA-2) // J. Climate. 2017. Vol. 30. No. 14. Pp. 5419–5454. DOI: 10.1175/JCLI-D-16–0758.1.

7. *Goncharenko L.P., Harvey V.L., Greer K.R., Zhang S.-R., Coster A.J.* Longitudinally dependent low-latitude ionospheric disturbances linked to the Antarctic sudden stratospheric warming of September 2019 // J. Geophys. Res. 2020. Vol. 125. No. 8. P. e2020JA028199. DOI: 10.1029/2020JA028199.

8. *Grooß J.-U., Konopka P., Müller R.* Ozone chemistry during the 2002 Antarctic vortex split // J. Atmos. Sci. 2005. Vol. 62. No. 3. Pp. 860–870. DOI: 10.1175/JAS-3330.1.

9. *Grytsai A.V., Evtushevsky O.M., Milinevsky G.P.* Anomalous quasi-stationary planetary waves over the Antarctic region in 1988 and 2002 // Ann. Geophys. 2008. Vol. 26. No. 5. Pp. 1101–1108. DOI: 10.5194/angeo-26–1101–2008.

10. *Hersbach H., Bell B., Berrisford P., Hirahara S., Horányi A., Muñoz-Sabater J., Nicolas J., Peubey C., Radu R., Schepers D., Simmons A., Soci C., Abdalla S., Abellan X., Balsamo G., Bechtold P., Biavati G., Bidlot J., Bonavita M., de Chiara G., Dahlgren P., Dee D., Diamantakis M., Dragani R., Flemming J., Forbes R., Fuentes M., Geer A., Haimberger L., Healy S., Hogan R.J., Hólm E., Janisková M., Keeley S., Laloyaux P., Lopez P., Lupu C., Radnoti G., de Rosnay P., Rozum I., Vamborg F., Villaume S., Thépaut J.-N.* The ERA5 global reanalysis // Q. J. Roy. Meteor. Soc. 2020. Vol. 146. No. 730. Pp. 1999–2049. DOI: 10.1002/qj.3803.

11. *Hirota I., Kuroi K., Shiotani M.* Midwinter warmings in the southern hemisphere stratosphere in 1988 // Q. J. Roy. Meteor. Soc. 1990. Vol. 116. No. 494. Pp. 929–941. DOI: 10.1002/qj.49711649407.

12. *Hoppel K., Bevilacqua R., Allen D., Nedoluha G., Randall C.* POAM III observations of the anomalous 2002 Antarctic ozone hole // Geophys. Res. Lett. 2003. Vol. 30. No. 7. P. 1394. DOI: 10.1029/2003GL016899.

13. *Klekociuk A.R., Tully M.B., Krummel P.B., Henderson S.I., Smale D., Querel R., Nichol S., Alexander S.P., Fraser P.J., Nedoluha G.* The Antarctic ozone hole during 2018 and 2019 // J. South. Hemisph. Earth Syst. Sci. 2021. Vol. 71. No. 1. Pp. 66–91. DOI: 10.1071/ES20010.

14. *Kogure M., Yue J., Liu H.* Gravity wave weakening during the 2019 Antarctic stratospheric sudden warming // Geophys. Res. Lett. 2021. Vol. 48. No. 8. P. e2021GL092537. DOI: 10.1029/2021GL092537.

15. *Kuttippurath J., Nikulin G.* A comparative study of the major sudden stratospheric warmings in the Arctic winters 2003/2004–2009/2010 // Atmos. Chem. Phys. 2012. Vol. 12. No. 17. Pp. 8115–8129. DOI: 10.5194/acp-12–8115–2012.

16. *Lim E.-P., Hendon H.H., Butler A.H., Thompson D.W.J., Lawrence Z.D., Scaife A.A., Shepherd T.G., Polichtchouk I., Nakamura H., Kobayashi C., Comer R., Coy L., Dowdy A., Garreaud R.D., Newman P.A., Wang G.* The 2019 Southern Hemisphere stratospheric polar vortex weakening and its impacts // B. Am. Meteorol. Soc. 2021. Vol. 102. No. 6. Pp. E1150–E1171. DOI: 10.1175/BAMS-D-20–0112.1.

17. *Manney G.L., Sabutis J.L., Allen D.R., Lahoz W.A., Scaife A.A., Randall C.E., Pawson S., Naujokat B., Swinbank R.* Simulations of dynamics and transport during the September 2002 Antarctic major warming // J. Atmos. Sci. 2005. Vol. 62. No. 3. Pp. 690–707. DOI: 10.1175/JAS-3313.1.

18. *Manney G.L., Millán L.F., Santee M.L., Wargan K., Lambert A., Neu J.L., Werner F., Lawrence Z.D., Schwartz M.J., Livesey N.J., Read W.G.* Signatures of anomalous transport in the 2019/2020 Arctic stratospheric polar vortex // J. Geophys. Res. 2022. Vol. 127. No. 20. P. e2022JD037407. DOI: 10.1029/2022JD037407.

19. *Milinevsky G., Evtushevsky O., Klekociuk A., Wang Y., Grytsai A., Shulga V., Ivaniha O.* Early indications of anomalous behaviour in the 2019 spring ozone hole over Antarctica // Int. J. Remote Sens. 2019. Vol. 41. No. 19. Pp. 7530–7540. DOI: 10.1080/2150704X.2020.1763497.

20. *Newman P.A., Kawa S.R., Nash E.R.* On the size of the Antarctic ozone hole // Geophys. Res. Lett. 2004. Vol. 31. No. 21. P. L21104. DOI: 10.1029/2004GL020596.

21. *Newman P.A., Nash E.R.* The unusual Southern Hemisphere stratosphere winter of 2002 // J. Atmos. Sci. 2005. Vol. 62. No. 3. Pp. 614–628. DOI: 10.1175/JAS-3323.1.

22. *Noguchi S., Kuroda Y., Kodera K., Watanabe S.* Robust enhancement of tropical convective activity by the 2019 Antarctic sudden stratospheric warming // Geophys. Res. Lett. 2020. Vol. 47. No. 15. P. e2020GL088743. DOI: 10.1029/2020GL088743.

23. *Roy R., Kuttippurath J., Lefèvre F., Raj S., Kumar P.* The sudden stratospheric warming and chemical ozone loss in the Antarctic winter 2019: comparison with the winters of 1988 and 2002 // Theor. Appl. Climatol. 2022. Vol. 149. Pp. 119–130. DOI: 10.1007/s00704–022–04031–6.

24. *Safieddine S., Bouillon M., Paracho A.-C., Jumelet J., Tencé F., Pazmino A., Goutail F., Wespes C., Bekki S., Boynard A., Hadji-Lazaro J., Coheur P.-F., Hurtmans D., Clerbaux C.* Antarctic ozone enhancement during the 2019 sudden stratospheric warming event // Geophys. Res. Lett. 2020. Vol. 47. No. 14. P. e2020GL087810. DOI: 10.1029/2020GL087810.

25. *Shen X., Wang L., Osprey S., Hardiman S.C., Scaife A.A., Ma J.* The life cycle and variability of Antarctic weak polar vortex events // J. Climate. 2022. Vol. 35. No. 6. Pp. 2075–2092. DOI: 10.1175/JCLI-D-21–0500.1.

26. *Solomon S.* Stratospheric ozone depletion: a review of concepts and history // Rev. Geophys. 1999. Vol. 37. No. 3. Pp. 275–316. DOI: 10.1029/1999RG900008.

27. *Stolarski R.S., McPeters R.D., Newman P.A.* The ozone hole of 2002 as measured by TOMS // J. Atmos. Sci. 2005. Vol. 62. No. 3. Pp. 716–720. DOI: 10.1175/JAS-3338.1.

28. *Wargan K., Weir B., Manney G.L., Cohn S.E., Livesey N.J.* The anomalous 2019 Antarctic ozone hole in the GEOS constituent data assimilation system with MLS observations // J. Geophys. Res. 2020. Vol. 125. No. 18. P. e2020JD033335. DOI: 10.1029/2020JD033335.

29. *Waugh D.W., Polvani L.M.* Stratospheric polar vortices. In: Polvani L.M., Sobel A.H., Waugh D.W. (Eds.). The Stratosphere: Dynamics, Transport, and Chemistry // Geophysical Monograph Series. 2010. Vol. 190. Pp. 43–57. DOI: 10.1002/9781118666630.ch3.

30. *Waugh D.W., Sobel A.H., Polvani L.M.* What is the polar vortex and how does it influence weather? // Bull. Amer. Meteor. Soc. 2017. Vol. 98. No. 1. Pp. 37–44. DOI: 10.1175/BAMS-D-15–00212.1.

31. *Zuev V.V., Savelieva E.S.* Dynamic characteristics of the stratospheric polar vortices // Dokl. Earth Sci. 2024. Vol. 517. No. 1. Pp. 1240–1248. DOI: 10.1134/S1028334X24601895.

EARTH RESEARCH FROM SPACE, 2025, No. 1, pp. 15–22

USING SATELLITE INFORMATION ABOUT THE EARTH

IMPACT OF A MAJOR ERUPTION OF THE SHIVELUCH VOLCANO (APRIL 2023, KAMCHATKA) ON ECOSYSTEMS: THE EXTENT OF BURIAL AND DESTRUCTION OF FORESTS ACCORDING TO SATELLITE DATA

© 2025 S. Yu. Grishin*

Federal Scientific Center of the East Asia Terrestrial Biodiversity, Far East Branch, Russian Academy of Sciences, Vladivostok, Russia

**e-mail: grishin@biosoil.ru*

Received July 31, 2024

Abstract. During large-scale eruption of the Shiveluch volcano in April 2023, the active dome collapsed and intense ash fall occurred. Based on the Sentinel-2 satellite images, the scale of burial of the territory by volcanic deposits was determined — ~60 km^2, and the diversity of buried and dead ecosystems was also estimated. The high-temperature deposits of the collapse blocked the southeastern sector of the volcano over an area of more than 50 km^2 in the altitude range of ~2000–500 m a.s.l. Below, up to ~150 m, pyroclastic flows descended, the lower mark of one of the 5 tongues is located at a distance of 22 km from the eruptive center. The deposits of these 5 flows occupied an area of 12 km^2. Forest and dwarf vegetation was destroyed in an area of ~24 km^2, and was mostly buried (up to 90% of the area), and also died due to the flooding of trees by plumes of pyroclastic flows and the impact of pyroclastic surges. In the zone of pyroclastic flows, the destroyed forests are formed mainly by stone birch and larch, as well as thickets of dwarf alder. Ash fallout thick covered the territory of central Kamchatka by deposits more than 1 cm with an area of more than 10,000 km^2; thickness of freshly deposited ash was 6–10 cm in the forest belt of the Shiveluch volcano; woody plants mostly survived. Post-eruption phenomena in the form of secondary ash transfer and redeposition of pyroclastics washed out by watercourses will last for many years and will lead to the formation of new zones of damage and destruction of vegetation.

Keywords: *volcanism, eruption, environmental dynamics, forest vegetation, pyroclastic flows, Kamchatka*

DOI: 10.31857/S02059614250102e7

INTRODUCTION

On April 10–13, 2023, a paroxysmal eruption of the Shiveluch volcano (central Kamchatka) occurred. According to the first eyewitness reports, an intense ash fall in the Klyuchi settlement (45 km south of the volcano) resulted in an ash layer up to 8 cm thick (Grishin et al., 2024). It was later discovered that the eruption was accompanied by the collapse of pyroclastic flows, the deposits of which covered an extensive area. After the appearance of satellite images, it became obvious that the environmental impact of the eruption was particularly large and that it was the largest volcanic event of the last decades in Kamchatka. The first data on the ash fall parameters and its environmental impact were published (Girina et al., 2023; Grishin et al., 2024). In this work, the area of pyroclastic flow deposits was determined using satellite images from the Sentinel-2 satellite imagery, and the extent of the eruption's impact on the nature of the area, including burial and forest damage, was revealed, and the diversity of destroyed vegetation was assessed. In addition to the analysis of satellite data, the materials of brief field studies conducted in the area in August 2023 and earlier, in 1996 and 2012 (Grishin et al., 2000, 2015) were used.

CURRENT ACTIVITY OF SHIVELUCH VOLCANO

Shiveluch volcano (height — 3283 m) is the northernmost, one of the largest and most active volcanoes in Kamchatka. The erupted products are andesites, which determines the explosive nature of eruptions with large-scale destructive consequences. Over the last centuries, particularly powerful eruptions occurred in ~1430, ~1650, 1854, and 1964 (Melekestsev *et al.*, 1991; *Ponomareva et al., 2015*). The catastrophic eruption of 1964 resulted in the formation of a volcanic desert on the southern slope of the volcano (Fig. 1) with an area of about 100 km^2 (Gorshkov and Dubik, 1969; Belousov and Belousova, 1995). Beginning in 1980,

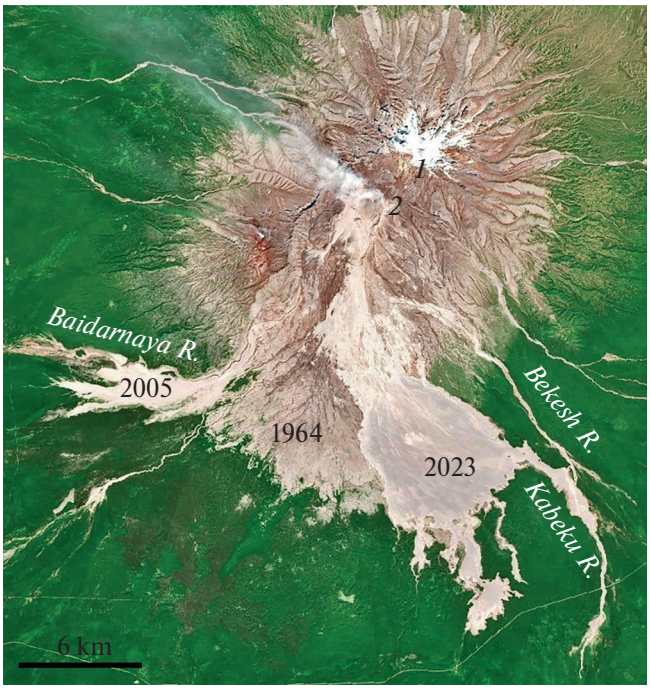

Fig. 1. Shiveluch volcano massif. Areas overlain by deposits of large recent eruptions (numbers correspond to the year of eruption). *1* — Stary Shiveluch summit (height 3283 m); *2* — active dome. Image from the Sentinel-2 satellite from July 1, 2023.

a large active dome grew in the crater of the volcano. Periodic moderate eruptions (in 1993, 2001, 2004, etc.) were accompanied by collapses of dome parts, ash falls, red-hot avalanches and pyroclastic flows. Due to the peculiarities of the volcano morphology, the main directions of collapses, glowing avalanches, pyroclastic flows and waves are oriented in the direction of the southern slopes of Shiveluch. A significant part of volcanics rushes along the valley of the Baidarnaya River in the southwestern sector of the volcano, as well as the Kabeku River in the southeastern sector. Large eruptions with pyroclastic flows (Fig. 1) occurred in 2005 and 2010 (Zharinov and Demyanchuk, 2013). Pyroclastic flows are a mixture of hot (>500 °C) debris and gas; the flows roll at high velocity down the depressions on the volcano slopes, burying river beds and valleys with their sediments. The flows are accompanied by pyroclastic surges, gas-saturated turbulent eddies of sandy material. The speed of the surges is tens of meters per second, and the temperature is several hundred degrees Celsius.

VEGETATION STATE BEFORE THE 2023 ERUPTION

The vegetation of the area is distributed on sediments of heterogeneous genesis and age. The area affected by the 2023 eruption is characterized by two main natural complexes. The first complex was located above 500 m a.s.l. and until April 2023 represented a volcanic desert with extremely sparse vegetation cover (Grishin et al., 2000). This part of the impact zone is formed by the deposits of the 1964 eruption and the deposits of the 2010 eruption located to the east (Figs. 1; *2a*). The former were collapse cold since the eruption; the latter were collapse / pyroclastic hot (locally hot, judging from thawing snow cover, they remained until April 2023). The second complex was located below 500 m; it was dominated by forest and partly meadow and shrub vegetation on old (about 600 years old) sediments of the previous volcanic catastrophes. In the altitudinal interval of 200–460 m a.s.l., forest vegetation of stone birch *Betula ermanii* and larch *Larix cajanderi* is located on hilly deposits of a giant collapse that occurred during a catastrophic eruption in the Late Pleistocene (*Ponomareva et al., 2015*). The upper parts of the hillsides are dominated by thickets of alder shrub *Alnus fruticosa*. Below 300 m, larch forests dominate, often with the participation of stone birch and other species of deciduous trees (Fig. *2a*). The array of spruce (*Picea jezoensis*) forests is located on the southwestern foothills of Shiveluch, and in the southeastern sector of the volcano, spruce forests occur only in places and, as a rule, sparsely.

EXTENT OF DEPOSITS OF VOLCANIC MATERIAL

During the eruption, in addition to intense ash fall, the active dome collapsed. The materials composing the dome collapsed by a hot avalanche to the south of the dome, and then passed through and were deposited on the southeastern slope of the volcano (Figs. 1; *2b*). The altitudinal range of the eruption products passage from the dome to the lower point of the deposits was about 2000 m vertically, and the maximum length was about 22 km. We can conditionally distinguish 3 zones (Fig. *2b*), which we will call zones of transit (zone I), accumulation (II), and long-range passage of pyroclastic flows (III).

The transit zone extends 7–8 km south of the active dome. Its upper half extends to a height of ~1300 m a.s.l. along a lifeless slope overlain by volcanic deposits of previous eruptions, which have been repeatedly deposited over the last decades. Between 1300–800 m a.s.l., the slope turns to the south-southeast, and areas of fresh sediments appear on the slope in sections, strips and ridges. Toward the lower boundary of Zone I, these areas become more numerous and interlock in some places, covering up to 70–80% of the territory. The area of visible deposits of 2023 in Zone I, according to the image from April 29, 2023 is about 10.5 km^2.

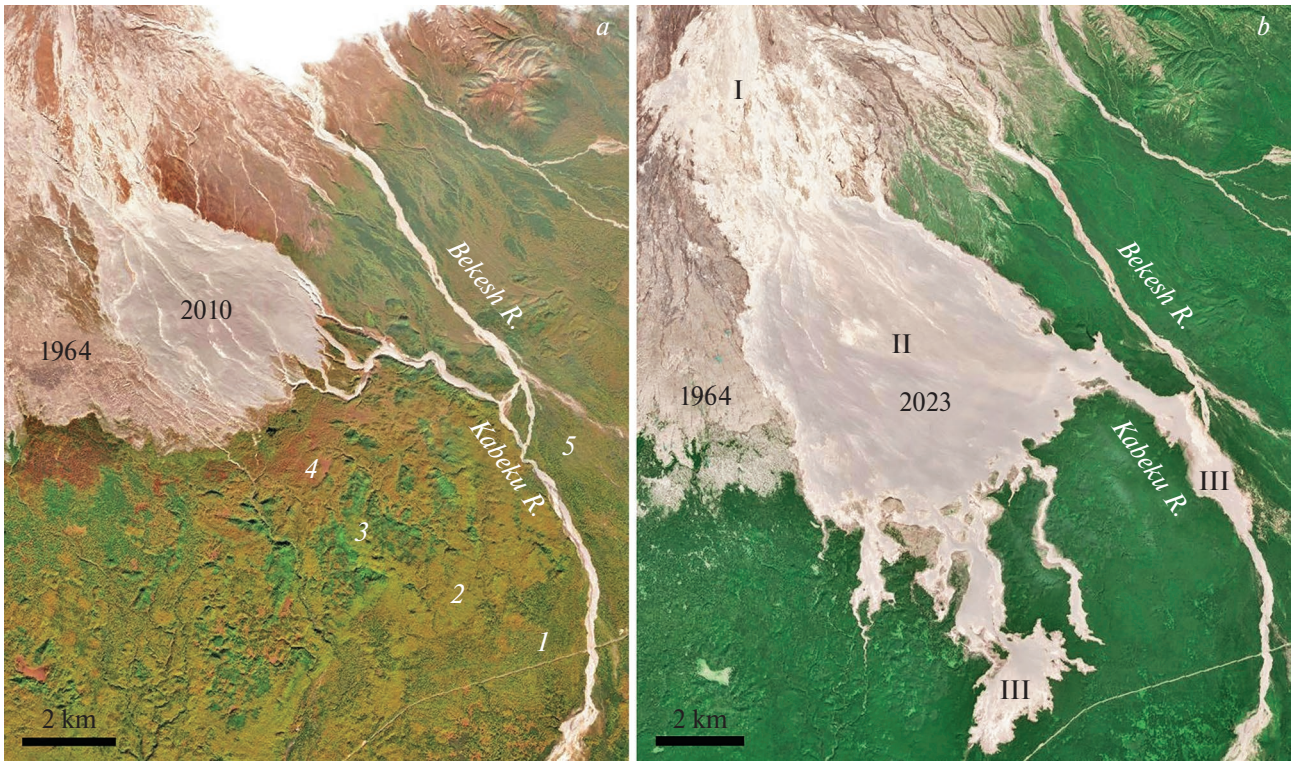

Fig. 2. Southeastern slope of Shiveluch volcano: *a* – condition before the eruption in 2023. Figures show the predominant vegetation: *1* — larch forests, *2* — stone birch forests, *3* — alder thickets, *4* — complex of meadows, shrubs and forests, *5* — mixed valley forests and shrubs. The year of eruption is indicated on the territories overlaid with volcanic deposits. Image from the Sentinel-2 satellite from September 24, 2023; *b* — deposits of the eruption of 2023, deposit zones: I – zone of transit, II — zone of large-scale accumulation of pyroclastic deposits, III — zone of long-distance passage of pyroclastic flows. Image from the Sentinel-2 satellite from July 1, 2023.

The accumulation zone is a field with an area of ~38 km^2 covered with deposits. The deposits lie on the southeastern slope, in the altitude range from 800 m to 400–500 m asl. The field extends from top to bottom for almost 8 km, expanding in a bell shape, and is ~7 km wide at the bottom. In the lower part of Zone II, sediments completely covered the valleys of the Kabeku River and three of its tributaries, with the third tributary had a nearly V-shaped incision more than 50 m deep (Grishin et al., 2015). The 2023 deposits overlapped the deposits of the previous eruption (October 2010), which in the thickest strata were hot until the 2023 eruption, judging from snow thawing over an area of ~2 km^2.

Below Zone II, the pyroclastic flows descended along riverbeds and valleys, resulting in five flow arms clearly distinguished, which formed Zone III (Fig. *2b*). The eastern arm traveled 4.5 km along the Kabeku River valley, descending to 220 m asl. The width of its band of high-temperature deposits reached 1 km. The central branch, the largest in area, descended along an old forested channel to 145 m asl, covering about 6 km. In its final part, the plume spread out in a large fan through the forest (mainly larch), covering an area about 3 km wide, and only 400–500 m short of the regional highway (Figs. *2b*; *4b*). The total area of deposits of all pyroclastic flow arms was ~12.5 km^2.

SEDIMENT TEMPERATURE AND THICKNESS

The temperature of pyroclastic flows material during their deposition exceeds 500 °C. In thick (tens of meters) strata, the temperature can remain very high for several years and even decades, while at the surface it rapidly decreases, especially during the cold season. Field measurements in August 2023 in Zones II and III showed that the temperature of deposits at a depth of 50 cm reached 50–65 °C. Soaring fumaroles with vapor temperatures of 200–300 °C at the outlet were found in many places where thick deposit strata were formed due to the relief conditions. It was revealed that series and chains of fumaroles were confined to buried riverbeds.

In Zone I, by the spring of 2024, the snow covering most of the deposits had stopped melting. This meant that the sediments had cooled down and, consequently, their relatively small thickness. Only a small part of the deposits, expressed by a chain of islands

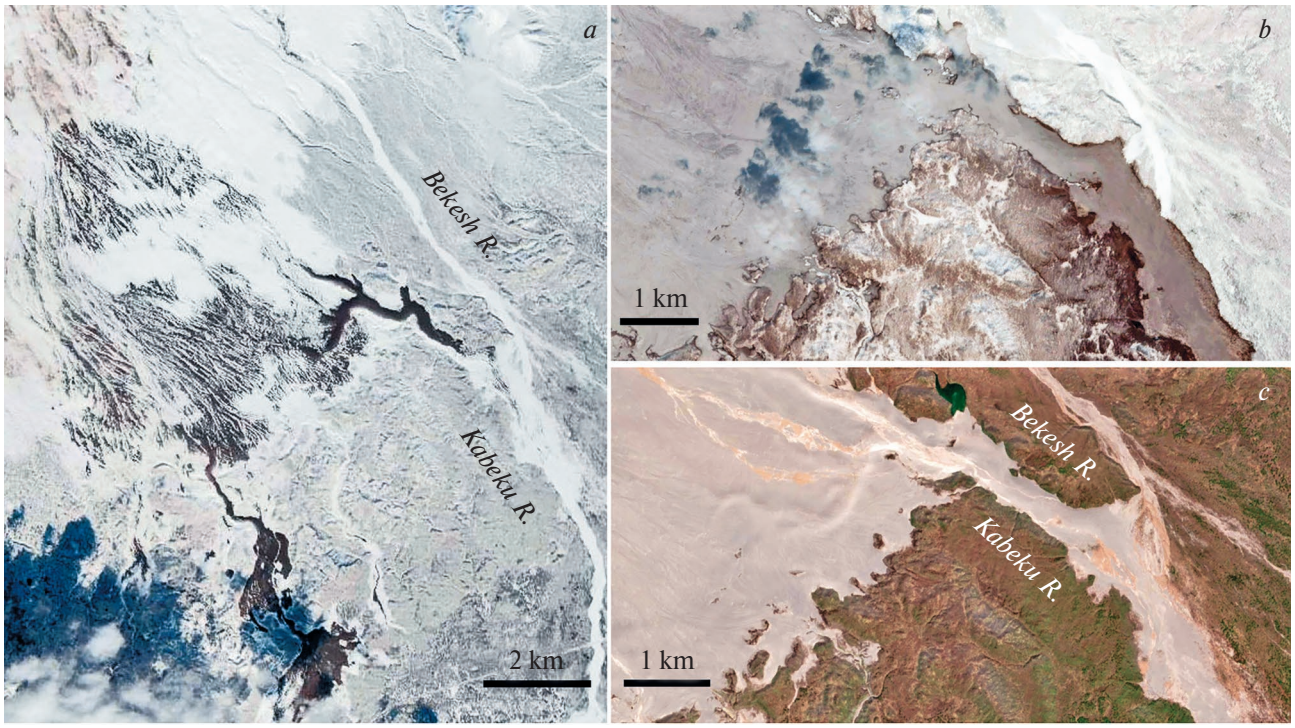

Fig. 3. Transformation of pyroclastic deposits surface: *a* — thawing of snow cover on hot pyroclastic deposits of the eruption of 2023. Sentinel-2 image from March 24, 2024; *b* — southeastern part of zone II, the valleys of the Kabeku River and its tributaries are buried. Sentinel-2 image from April 29, 2023; *c* — the same area 13 months later: deposits in the buried tributary valleys have subsided; fresh sediments have marked new channels; a dammed lake has been formed (above, in the middle). Sentinel-2 satellite image from June 5, 2024.

in the axial part of the zone, remained snow-free, i.e. hot.

In most of Zones II and III, deposits remained hot during the first year after the eruption, as judged by snow melt in the spring of 2024. Severe frosts in the winter of 2023/2024 caused much of the surface to cool; under these conditions, snow thawed only in deep incision areas in V-shaped valleys, where deposits were up to 50 m thick (Fig. *3a*). When frosts weakened by spring 2024, snow thawing resumed in most of Zone II (Fig. *3a*). Thus, the multi-meter thick deposit strata that overlapped the gentle slopes in Zone II did not cool during the long frosty (in mountain conditions) winter either. However, due to the different thickness of deposits there was a differentiation of thawing intensity. Large areas covered with non-stagnant snow show the presence of low thickness deposits inside the contour of zone II. Their total area is about 8–12 km^2, and the thickness of deposits is presumably 1–5 m. The satellite images of March 2024 show that the main part of the area of zone II remains heated. The structure of the passage and deposition of material is noticeable: one can see that there are many streams; subparallel strips of deposits alternate with narrow areas of low thickness deposits (unmelted snow).

In Zone III, snow first thawed on the surface of deposits of most of the largest flows ("central" and in the Kabeku River valley). Thawing on the remaining pyroclastic flows was absent or represented by fragments, i.e., their deposits turned out to be thin.

Thus, the thawing of the snow cover can be used to judge the temperature and, accordingly, the thickness of deposits, as well as to conditionally distinguish zones of different thicknesses: presumably 30–50 m, 10–25 m and up to 5 m. As a result, we can tentatively estimate the total volume of pyroclastic deposits in zones I–III to be 0.4–0.5 km^3.

The change in the relief caused localized backwatering of one of the watercourses, which was blocked by pyroclastic deposits. As a result, a lake was formed, which by the early summer of 2024 reached 700 m across and an area of about 0.08 km^2 (Fig. *3c*).

BURIAL OF FOREST AND SHRUB VEGETATION

The erupted pyroclastic deposits pushed down the boundary between volcanic desert and forest (Fig. 2). The displacement of this boundary was ~1–2.2 km, decreasing vertically from an elevation of 490–540 m to 400–500 m asl. The new boundary

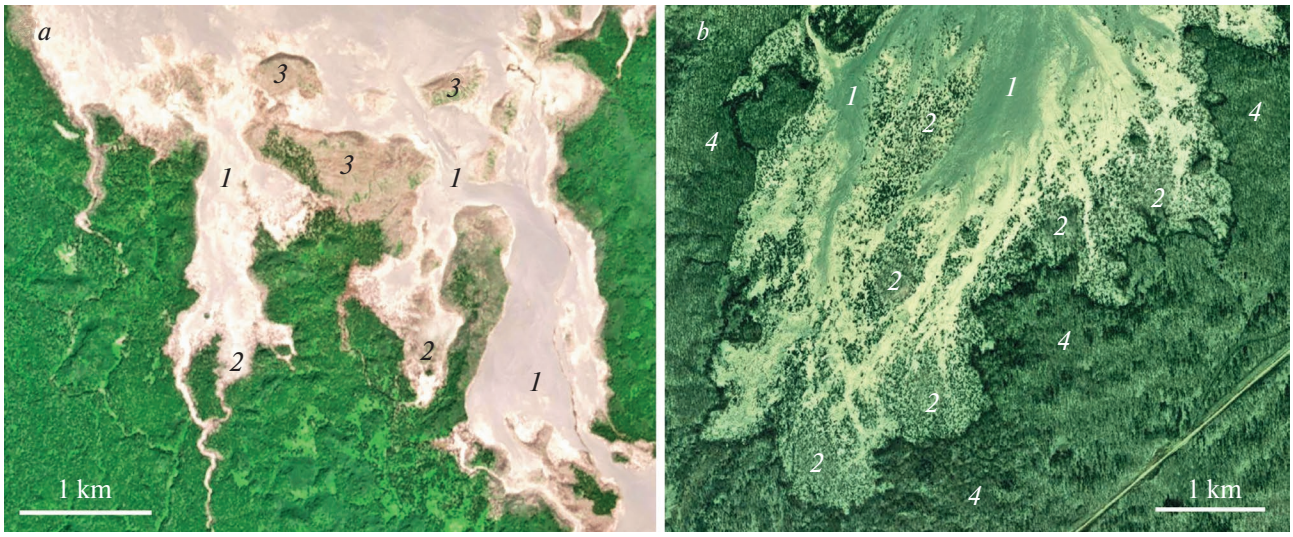

Fig. 4. Death and burial of forest stands: *a* — image from the Sentinel-2 satellite from July 1, 2023; *b* — image from the GeoEye-1 satellite from April 29, 2023. *1* — zones of powerful deposits of pyroclastic flows, which completely buried forests; *2* — areas of destroyed and half-buried forests; *3* — areas of forest death under the influence of pyroclastic surges; *4* — forest before the beginning of vegetation, with snow cover under the stand canopy.

between volcanic desert and lower slopes with surviving forest was sharp; above the boundary and close to it there are more than a dozen islands of forest, ~50–500 m across (Figs. *2b*; *4a*). They are the upper parts of the hills, the bases of which were buried by deposits of moving pyroclastic deposits streams. Between the former and new boundaries, a contour was formed with length of ~7 km along the front and a total area of ~11 km^2, where forest, meadow, and shrub vegetation was completely buried. In addition to the closed vegetation of the forest belt, the pyroclastic deposits of 2023 buried extremely sparse vegetation cover on the 1964 deposits (to the west of Zone II) and meadow and shrub vegetation (to the east of Zone II).

Below Zone II, forest vegetation was buried by deposits of five pyroclastic flow tongues. The thickness of deposits was up to several tens of meters in deeply incised channels of the largest tongues (at an altitude of 390–450 m). Forests of stone birch and larch, as well as thickets of shrubs, mainly alder. As a rule, along the buried channels, along the axial part of the tongues, continuous deposits were observed, without dead trees or broken trunks. These bands of deposits have thick pyroclastics that remained hot even a year after the eruption. In the lower half of the tongues, thick sediment strata are surrounded by a edging of half-buried forest (Fig. *4b*). The thickness of sediments in this fringe is apparently up to a dozen meters; as one moves away from the thick strata to the living forest, it gradually, over 200–400 m, becomes wedged out. The stand is sparse, the undergrowth is buried, tree trunks are partly buried, and most of them are broken or burned out at the tree butt buried in hot deposits and lying on the surface. The deposits in these peripheral zones 4 months after the eruption were hot and half-buried wood smoldered in some places. Standing dead trees were also encountered locally; due to moderate dynamic impact on the base of the trunks, they survived. The total area of half-buried and dead stands is ~2.5 km^2.

AFFECTING FOREST VEGETATION

In the final parts (plumes) of pyroclastic flows, which spread wide fans through the forest, the thickness of deposits decreases to 1 meter and less; therefore, they quickly cooled down. The trees were not blown down and buried, but remained standing. The deposits burned the bases of the trunks at the contact points and also thermally affected the crowns (up to scorching; individual trees burned). As a result, most trees died; strips and patches of dead stands were formed.

In addition, the pyroclastic surges that accompanied the pyroclastic flows left their trace in the form of bands of dead trees along the valley sides in the mountain topography. High-temperature gas-sand eddies scorched and partially destroyed the stand of trees, leading to its death in strips up to ~50–100 m wide adjacent to the flow deposition zones (just as it happened in 2005 in the Baidarnoi River valley and in the Kabeku River valley in 2010 (Grishin, 2009; Grishin et al., 2015)).

The areas of stands killed by pyroclastic surges and low-power pyroclastic flow plumes are located mainly above 200 m a.s.l.; they consist predominantly

of stone birch. At the same time, larch forests located below 200–220 m were destroyed (trees broken, burned and felled) or perished (without significant external damage) under the impact of partial burial by more powerful deposits of pyroclastic flows.

The beginning of vegetation (image from June 26, 2023) showed the extent of stand death from the passage of low-power plumes of pyroclastic flows and pyroclastic surges — about 3.5 km^2. The largest area of the dead stands with the area ~0.8 km^2 is located in the western part of the contact zone II deposits and forest (Fig. *2b*; *4a*). Mountain forests of stone birch there have died in an area up to 1500 m wide and 700 m deep. In the forest islands located near the lower boundary of Zone II, trees and shrubs were also mostly killed. A number of islets show that in their northern (upper) half the woody vegetation completely perished from the impact of pyroclastic waves, while in the southern half it partially survived, protected by the relief.

Overall, forest and shrub vegetation, including coniferous forests, was buried and killed over an area of about 24 km^2. According to preliminary estimates, the forests destroyed consisted of ~50% stone birch, 25% larch (including spruce in places), about 15% mixed and deciduous forests, and about 10% alder shrub thickets.

ASH FALL

The ash fall covered a wide sector of the southwestern foot of the volcano, as well as areas located from the volcano to the west (to the Sredinniy Ridge; distance of about 90–100 km), southwest (Kamchatka River valley, about 130 km), and south/southwest (northern half of the Kliuchevskoi group of volcanoes). Examination of satellite images showed that after the start of the 2023 growing season, light-colored dried ash was visible only in areas of bare ground. In total, it was possible to identify more than 10 types of natural and anthropogenic landscapes where the presence of ash accumulations was recorded on satellite images. According to these marks, it was possible to delineate the territory of distribution of ash fall deposits, having a thickness of more than 1 cm, with an area of about 10000 km^2 (Grishin et al., 2024). Assuming, in accordance with the results of our field measurements, an average thickness of 2.5 cm, we obtain an ash volume in this area of about 0.25 km^3. This is a large value even without taking into account the distant tephra (which was deposited in a layer less than 1 cm thick). The April 11, 2023 ash fall was the largest volcanic ash fall in almost 60 years and the largest in Russia in the last 40 years in terms of the volume of spewed products. The negative impact of the moderate ash fall on the vegetation of the forest belt (fresh sediment thickness of 6–10 cm) was minimized due to a number of circumstances (thin ash, lack of foliage, snow cover on which the ash layer rested).

POST-ERUPTIVE EVENTS

During the snow-free period of 2023, fresh volcanic deposits began to erode and be transported by watercourses. The beginning of this process is recorded on the image from the WorldView-3 satellite image from May 20, 2023: the flow of the Bekesh River, which flows into the Kabeku River, erodes the deposits of the pyroclastic flow. Following it began the erosion of sediments in the upper reaches of the Kabeku River and its tributaries, the valleys of which were buried by sediments of 2023. New channels began to form on the surface of fresh and hot sediments; the image from the Sentinel-2 satellite image from 05.06.2024 shows 6 channels crossing Zone II from top to bottom and going down into Zone III (some of them can be seen in Fig. *3c*). Pyroclastic sediments transported along these channels are re-deposited downstream in forest areas, which leads to desiccation and death of tree stands. Thus, a large area of forest desiccation along the left bank of the Kabeku River began to form; by June 17, 2024, its area amounted to about 2 km^2 Fig. *5a*, *b*).

In the vast open areas above the new forest boundary, freshly deposited loose materials will be subjected to erosion and their surface will be dusty in windy weather. This process was active during the snow-free period of 2023, especially when winds became strong (more than 20 m/s, according to the meteorological station in Klyuchi settlement). As a result, thousands of tons of dust raised into the air were transported not only in the volcanic desert, but also carried tens of kilometers away from the volcano, reaching the Pacific Ocean (Fig. *5c*). These processes were exacerbated by the significant volume of tephra deposited during the large-scale ash fall on April 11, 2023, and may continue for many years.

DISCUSSION

The 2023 eruption largely repeated the eruptive event of October 2010, when, as a result of the dome collapse, hot masses were deposited on the southeastern slope; pyroclastic flows descended below the extensive accumulation zone; and ash fall occurred in the southern sectors of the volcano and in the remote vicinity (tens of kilometers from the eruption center). However, the scale of the 2023 eruption is noticeably larger, and the area of hot deposits is significantly larger. At the same time, the high-temperature deposits of 2023 overlapped the deposits of 2010, which had not yet cooled down and were hot in thick strata.

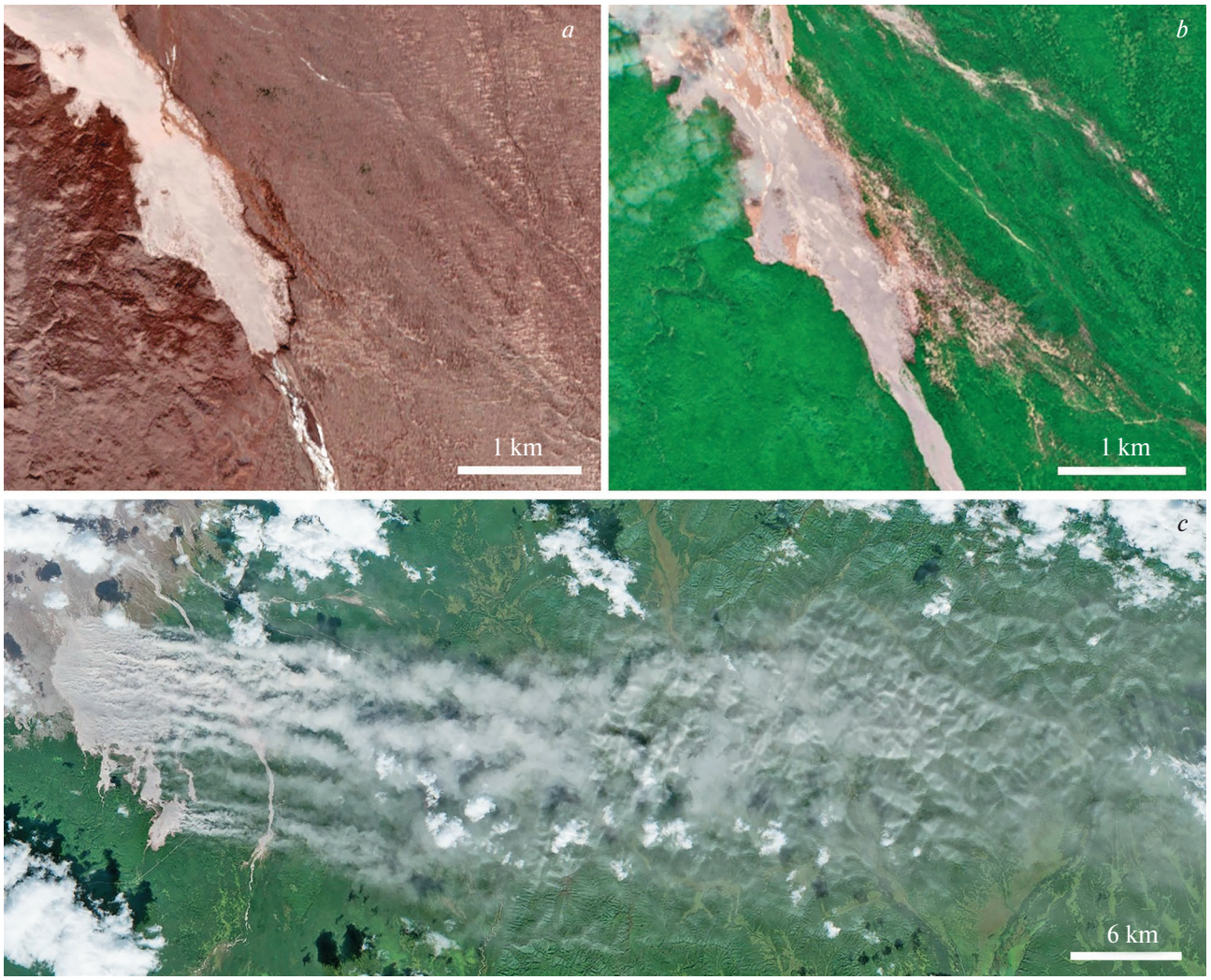

Fig. 5. Post-eruptive phenomena: *a* – tongue of the pyroclastic flow in the valley of the Kabeku River before the beginning of its erosion. Image from the Sentinel-2 satellite from May 17, 2023; *b* — erosion of the territory along the left bank of the Kabeku River by redeposited pyroclastic deposits. Image from the Sentinel-2 satellite from June 17, 2024; *c* — transport of ash and thin pyroclastic deposits by strong wind from the surface of the eruption deposit field of 2023 (left part). Image from the Sentinel-2 satellite from September 4, 2023.

The pyroclastic flows of 2023 traveled much farther and lower — up to 22 km from the volcano dome (up to 18 km in 2010); this is the maximum distance for modern eruptions in Kamchatka and the Kurils. It is significant that no lahars (volcanogenic mudflows) were formed, despite the fact that the eruption occurred during the period of maximum snow accumulation. This can be explained by the special thickness and temperature of pyroclastic deposits, the flows of which, moving rapidly, overlapped the snow cover and instantly vaporized it in its many meters of heated thickness.

The area of forest and shrub vegetation buried as a result of the 2023 eruption significantly (by an order of magnitude, according to our data) exceeded the area of forests buried during the 2010 eruption. Initially (in April-June 2023), the extent of forest damage by low-power plumes of pyroclastic flows and pyroclastic surges that traveled through the forest and scorched trees, causing them to die, was unclear. With the beginning of the growing season of 2023, it was possible to identify the affected zones and estimate their area (about 3.5 km^2) from the strips of dead stands.

In general, the 2023 eruption significantly increased the area of a huge (more than 150 km^2) volcanogenic badland located on the southern, southwestern and southeastern slopes of Shiveluch volcano. The negative impact of the huge volume of deposits on the nature of adjacent areas will continue for a number of subsequent years and decades.

CONCLUSION

As a result of the strong eruption, a radical change of the natural environment with large-scale burial and destruction of ecosystems occurred in the impact area. High-temperature sediments from the April 2023 eruption covered the slopes of the volcano with a multimeter-long cover of ~60 km^2, noticeably reducing the upper boundary of the forest in its southeastern sector. Pyroclastic flows traveled a record distance for modern eruptions in Kamchatka — up to 22 km from the eruptive center. The impact on the ecosystems of the southeastern sector of the volcano is a local ecological disaster. Forest and shrub vegetation, including coniferous forests, was buried and killed over an area of about 24 km^2.

ACKNOWLEDGEMENTS

I thank volcanologists M.G. Belousova and A.B. Belousov (IV&S FEB RAS) who reviewed the paper and made constructive comments.

REFERENCES

1. *Belousov A.B., Belousova M.G.* Izverzhenie vulkana Shiveluch v 1964 g. (Kamchatka) — plinianskoe izverzhenie, predvaryavsheesya krupnomasshtabnym obrusheniem postroyki [The 1964 eruption of Shiveluch (Kamchatka) — a plinian eruption preceded by a voluminous slide of the cone top] // Volcanology and Seismology. 1996. Vol. 17. Pp. 497–508. (In Russian).

2. *Girina O.A., Lupyan E.A., Horvat A., Mel'nikov D.V., Manevich A.G., Nuzhdaev A.A., Bril' A.A., Ozerov A.Yu., Kramareva L.S., Sorokin A.A.* Analiz razvitiya paroksizmal'nogo izverzheniya vulkana Shiveluch 10–13 aprelya 2023 goda na osnove dannyh razlichnyh sputnikovyh sistem [Analysis of the development of the paroxysmal eruption of Sheveluch volcano on April 10–13, 2023, based on data from various satellite systems] // Sovremennye problemy distancionnogo zondirovaniya Zemli iz kosmosa. 2023. No. 2. Pp. 283–291. (In Russian).

3. *Gorshkov G.S., Dubik Yu.M.* Napravlennyj vzryv na vulkane Shiveluch [Direct explosion on the Shiveluch volcano] / Vulkany i izverzheniya. Moscow: Nauka, 1969. Pp. 3–37. (In Russian).

4. *Grishin S.Yu.* Forest die-off under the impact of burning pyroclastic surge (Shiveluch volcano, Kamchatka, 2010) // Russian Journal of Ecology. 2009. No. 2. Pp. 146–148.

5. *Grishin S.Yu., Belousov A.B., Belousova M.G., Perepelkina P.A.* Vozdeystvie peplopada izverzheniya vulkana Shiveluch (Kamchatka, 11 aprelya 2023 g.) na lesnuyu rastitel'nost' [Impact of ash fallout of the 2023 eruption of Shiveluch volcano (Kamchatka) on the forest vegetation] // Biota i sreda prirodnyh territoriy. 2024. No. 1. Pp. 39–55. (In Russian).

6. *Grishin S.Yu., Burdukovskij M.L., Lazarev A.G., Komachkova I.V., Perepelkina P.A., Yakovleva A.N.* Gibel' rastitel'nosti v rezul'tate prohozhdeniya piroklasticheskoj volny (vulkan Shiveluch, Kamchatka, 2010 g.) [Devastation of vegetation as a result of an impact of pyroclastic surge (Shiveluch volcano, Kamchatka, 2010)] // Vestnik DVO RAN. 2015. No. 2. Pp. 101–108. (In Russian).

7. *Grishin S.Yu., Krestov P.V., Verholat V.P., Yakubov V.V.* Vosstanovlenie rastitel'nosti na vulkane Shiveluch posle katastrofy 1964 g. [Restoration of vegetation on the Shiveluch volcano after the 1964 disaster] // Komarovskie chteniya. Vladivostok: Dal'nauka, 2000. No. 46. Pp. 73–104. (In Russian).

8. *Zharinov N.A., Demyanchuk Yu.V.* Large explosive eruptions of Shiveluch volcano (Kamchatka) with partial destruction of the extrusive dome (February 28, 2005 and October 27, 2010) // Journal of Volcanology and Seismology. 2013. Vol. 7. No. 2. Pp. 131–144.

9. *Melekescev I.V., Volynec O.N., Ermakov V.A., Kirsanova T.P., Masurenkov Yu.P.* Vulkan Shiveluch [Shiveluch volcano] // Deystvuyushchie vulkany Kamchatki. 1991. Vol. 1. Pp. 84–103. (In Russian).

10. *Ponomareva V., Portnyagin M., Pevzner M., Blaauw M., Kyle Ph., Derkachev A.* Tephra from andesitic Shiveluch volcano, Kamchatka, NW Pacific: chronology of explosive eruptions and geochemical fingerprinting of volcanic glass // International Journal of Earth Sciences. **2015**. Vol. 104. Pp. 1459–1482.

EARTH RESEARCH FROM SPACE, 2025, No. 1, pp. 23–34

USING SATELLITE INFORMATION ABOUT THE EARTH

STUDY OF DYNAMICS REGULARITIES FOR MORPHOLOGICAL PATTERN OF ABRASION SHORES OF CRYOLITHOZONE BASED ON COMPLEXING MATHEMATICAL MODELING AND SPACE IMAGERY

© 2025 A. S. Victorov*

Federal State Budgetary Institution of Science Sergeev Institute of Environmental Geoscience of Russian Academy of Science (IEG RAS) Moscow, Russia

**e-mail: vic_as@mail.ru*

Received May 23, 2024

Abstract. The article is devoted to the study of dynamics regularities of abrasion shores of the cryolithozone based on complex mathematical modeling and space imagery including their significance for obtaining information on dynamic parameters of ongoing processes based on remote sensing data. The studied landscape of abrasion shores is a combination of thermal cirques of different ages and preservation, it develops under the action of processes of both the appearance of new thermal cirques and partial or complete erasure of existing ones due to the formation of new ones. The characteristic feature of thermal cirques is a clear arc-shaped boundary with the adjacent watershed surface, which is well detected on remote sensing data. The technique includes creating and analyzing a mathematical model of the morphological pattern changes of abrasion shores within the cryolithozone. The model uses the approach of the random process theory and empirical measurement of thermal cirques in different physiographic conditions on space imagery. The combination of mathematical modeling with space imagery interpretation allowed us to show that in different physiographic and geocryological conditions, a stable stationary distribution of thermal cirque sizes of abrasion shores of the Arctic cryolithozone is formed with a significant development time in homogeneous areas. The physiographic and geocryological variety of different sites does not prevent the existence of the limiting stationary distribution. Thus, the morphological pattern of the abrasion shore, being in constant change, nevertheless has a stationary distribution of thermal cirque sizes, their average size, and average location density, i.e., it is in a state of dynamic balance. The research gave a mathematical dependence between the limiting thermal cirque size distribution for abrasion shores and the size distribution for forming young thermal cirques. The sites' physical-geographical, geological-geomorphological, and geocryological conditions influence the character of the stationary limit distribution through the size distribution of forming young thermal cirques. The results obtained allow us to predict quantitative characteristics of the thermal cirques (and consequently landslides) formation process, namely, the size distribution of emerging new thermal cirques and landslides, based on measurements of the observed thermal cirque sizes using high-resolution single-shot remote sensing data. This is essential in predicting the development, in particular, of shore retreat.

Keywords: *mathematical morphology of landscapes, abrasion shores, cryolithozone, mathematical models of landscape morphological patterns, remote sensing data, mathematical modeling*

DOI: 10.31857/S02059614250103e1

INTRODUCTION

Many studies are devoted to morphological peculiarities of abrasion banks of cryolithozone. An extensive group of works is devoted to the study of ongoing processes in connection with bank retreat (Belova et al., 2001; Novikova, 2002; Pizhankova, Dobrynina, 2010; Aleksyutina et al., 2018; Belova et al., 2020), landscape factors influencing the development of processes (Sovershaev, 1998; Khomutov, Leibman, 2008; Kizyakov, 2005; Vasiliev et al. 2001), their connection with climatic characteristics (Leibman et al., 2021). However, most researchers study the processes of development of abrasion banks of cryolithozone in connection with retreat, and, accordingly, the extent of morphological elements (thermal cirques) and its changes in the direction perpendicular to the shoreline are analyzed. At the same time, little attention has been paid to the study of the extent of thermal cirques along the coastal slope and its quantitative parameters.

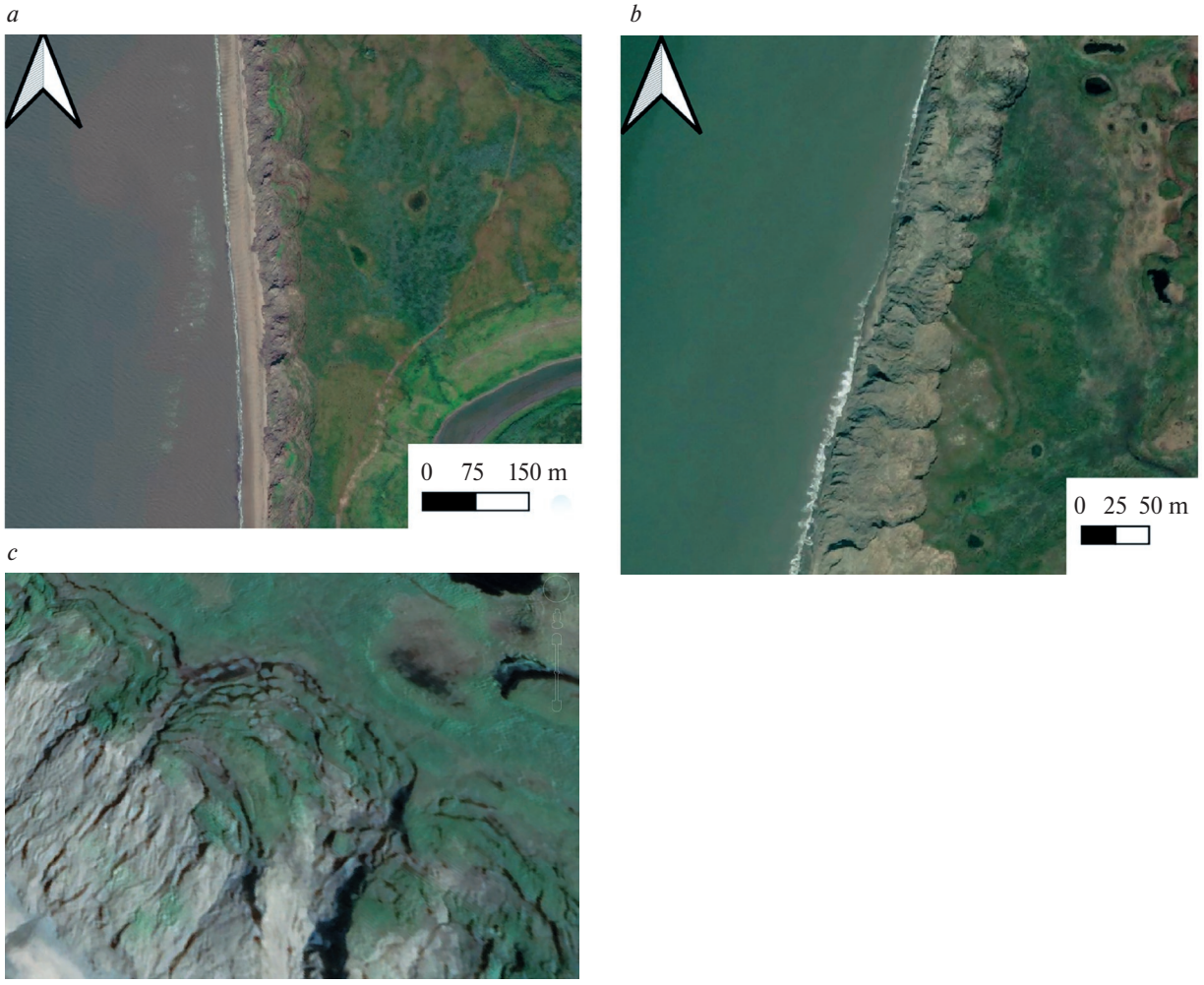

Fig. 1. Typical image of abrasion banks with the development of thermal cirques in the cryolithozone on the materials of high-resolution visible space imagery: *a, b* — general view (Victorov et al., 2023), *c* — example of a thermal cirque.

The aim of the research was to study the regularities of dynamics of abrasion banks of cryolithozone based on the complex of mathematical modeling and space imagery and their significance for obtaining information on ongoing processes, including their quantitative parameters, using remote sensing data.

The landscape of abrasion banks with the development of thermal cirques is a combination of thermal cirques, including landslide bodies of different ages, surfaces with the development of intensive thermo-abrasion, erosion, rockfall and thermodenudation processes. A characteristic feature of thermal cirques is a clear arc-shaped boundary with the adjacent watershed surface, well interpreted on the materials of space surveys, the appearance of such a boundary is associated with the fact that the formation of a thermal cirque begins, as a rule, with the development of landslide process. It is not uncommon to also observe arc-shaped residual areas of the watershed surface on the slope, corresponding to different stages of landsliding. A typical view of the bank is presented in Fig. 1.

The study is oriented to investigate the change in the size of thermal cirques along the shoreline; the length of the chord closing the arc-shaped boundary of the thermal cirque with the adjacent watershed surface was taken as the size of the thermal cirque.

The development of shores occurs under the action of a complex of processes involved in the formation of values of the thermal cirque size, including an increase in the number of thermal cirques due to the formation of a new thermal cirque inside the boundaries of an existing thermal cirque with the older thermal cirque splitting into two parts, a decrease in the number of thermal cirques due to the complete erasure of thermal cirques (and, accordingly, their chords) when overlapping younger ones, partial erasure of already existing thermal cirques with preservation of their number due to the overlapping of younger ones ("lateral erasure"), the appearance

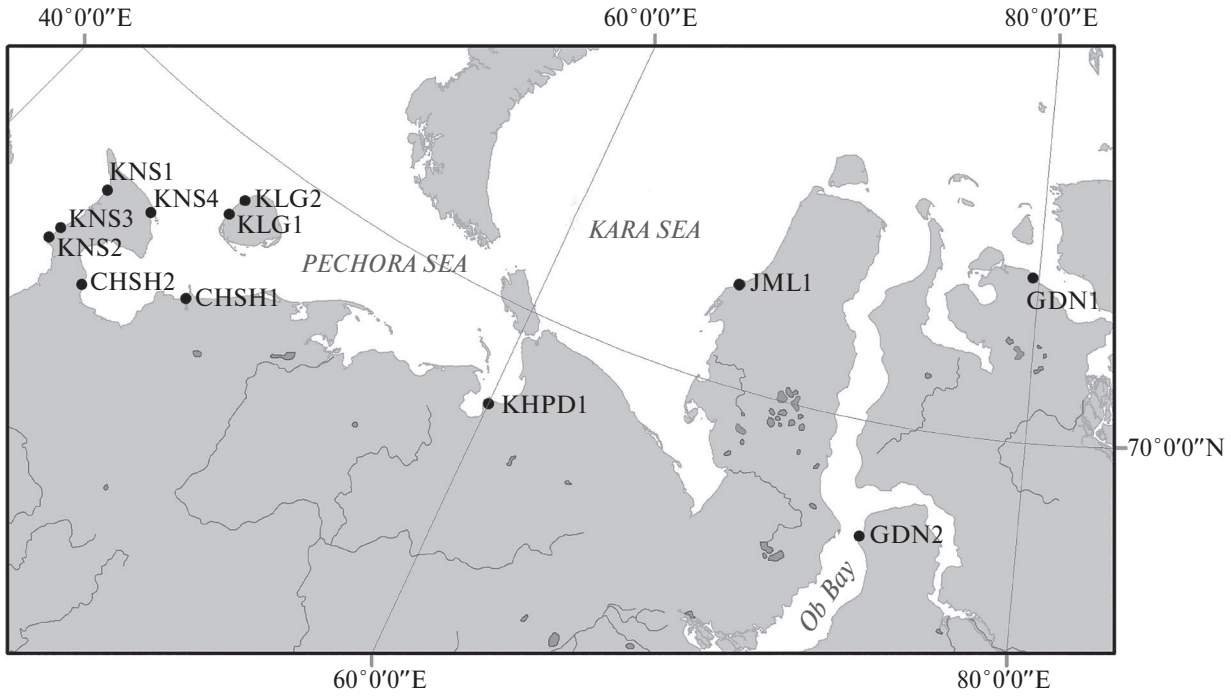

Fig. 2. Schematic of key site locations.

of a new thermal cirque on one or another thermal cirque ("lateral erasure"), and the appearance of a new thermal cirque on one or another thermal cirque.

In this case, the boundary of the coastal slope and the adjacent watershed surface is a system of arcs of thermal cirques, some of which are new, unaffected by subsequent erasures, and the other part is residual, preserved after one-, two-, three-, etc. multiple partial erasures of existing thermal cirques by new ones. Thus, in general, on the image the researcher observes at a random moment of time (survey) a system of different-aged formations in constant change. In this situation the problem arises — how to correlate quantitative characteristics of the image observed on the space image with quantitative dynamic parameters of the ongoing process of thermal cirques formation, and accordingly what information about the process the image allows to extract.

METHODOLOGY

The methodology included the following steps:

• creation and analysis of a mathematical model of changes in the morphological pattern of abrasion banks in the cryolithozone,

• study of thermal cirque sizes in different physiographic conditions using satellite data.

The mathematical model of changes in the morphological pattern of abrasion banks in the cryolithozone was based on the consideration of ongoing changes as a random process

• study of thermocircuit sizes in different physiographic settings using satellite data included:

• selection of key sites,

• measurement of thermal cirque sizes using space imagery materials,

• statistical processing of the obtained characteristics of the morphological pattern of the coastal slope and analysis of the obtained results.

The key sites were selected based on the requirements of relative morphological homogeneity of the area and homogeneity of physiographic, primarily geological-geomorphological and geocryological conditions. As a result, 12 sites with a length of 2.5–10.1 km were selected, which generally have a rectilinear strike (Fig. 2) and are located within the coastline of the Kanin Nose, Gydansky, Tazovsky and Yamal peninsulas, Kolguyev Island, and Khaipudyrskaya Bay.

High resolution satellite images from WorldView 3 (0.3 m/pix resolution), GeoEye 1 (0.5 m/pix resolution), WorldView 2 (0.5 m/pix resolution) and several other satellites were used to analyze morphological features.

RESULTS

The first part of the solution to the problem at hand is to determine the change in the probability distribution of thermal cirque sizes over time to assess its behavior with significant time of abrasion bank development.

For this purpose, the model proposed earlier (Victorov, 2022) for the formation of the morphological pattern of a rectilinear long abrasion bank (L) with homogeneous physiographic and geocryological conditions was used; relative constancy in time of climatic conditions is also assumed. The model is based on the following assumptions:

— the probability of appearance of new thermal cirques (in the number k = 1,2...) for the time Δu on the coastline segment[1] Δl is determined only by the values of the time interval and the segment[2]

$$p_1(\Delta\ell, \Delta u) = \lambda\Delta\ell\Delta u + o(\Delta\ell\Delta u),$$
$$p_k(\Delta\ell, \Delta u) = o(\Delta\ell\Delta u),\ k > 1,$$

where λ is the parameter corresponding to the average number of thermal cirques formed per unit time on the unit length of the coastline;

— sizes (arc chord length) of emerging thermal cirques do not depend on the place of their appearance on the site and have a constant probability distribution $F_0(x)$ independent of time[3].

The analysis allowed us to show (Victorov, 2022) that in this case the appearance of new thermal cirques corresponds to a Poisson random process, i.e., the probability of appearance of k thermal cirques at length l for time u is given by the expression

$$P_\mu(k) = \frac{(\lambda u l)^k}{k!} e^{-\lambda u l} \quad (1)$$

Hence, if the coastal segment of interest has the size Δv the probability of a single hit of the right border of the forming thermal cirque inside this segment during the time interval Δu based on the model assumptions and the Poisson character of the process of appearance of new thermal cirques (1), is as follows

$$q = \lambda\Delta v\Delta u + o(\Delta u) \quad (2)$$

and the probability of the right border of the forming thermal cirque not falling inside this segment is equal to

$$p_0^1 = e^{-\lambda\Delta v u} \quad (3)$$

In addition, it is shown that the probability that the considered thermal cirque will be neither hit nor erased during the time u by a forming thermal cirque with an initial point outside the considered thermal cirque is given by the expression

$$p_0^2 = e^{-\lambda a u} \quad (4)$$

where a is the mathematical expectation (average size) of forming (young) thermal cirques.

In the first step, we obtain an equation for the variation of the probability distribution of the thermal cirque size (chord length of the thermal cirque arc) in time. Let the thermal cirque dimensions at time u have a probability distribution $F(x,u)$[4]. Consider the behavior of thermal cirque for the time interval $(u, u + \Delta u)$ the following cases are possible (Fig. 2):

a) the thermocircus remains unchanged,

b) splitting an older thermal cirque into two elements with erasure of some part by forming a new thermal cirque inside the boundaries of the existing one ("internal erasure"), thus increasing the total number of thermal cirques,

c) erasure of part of the thermal cirque (and consequently part of the chord) due to the superposition of younger ones ("lateral erasure"),

d) complete erasure of the thermal cirque (and consequently of the chordae) at the superposition of the formed younger one.

The last three cases are accompanied by the appearance of a newly formed thermal cirque (e) at one or another site.

Let the total number of thermal cirques at time u be n_0 and the number of thermal cirques with chord less than x is respectively

$$n_1(x,u) = n_0 F(x,u)$$

Consider an existing thermal cirque with dimension y (chord length), introduce a coordinate system with zero at the right end of the chord and directed to the left. Determine the mathematical expectation of the number of thermal cirques with chord less than x at the moment $u + \Delta u$.

In case (a), the fact that the thermal cirque of size y will be neither erased nor damaged during the time interval Δu corresponds to the fulfillment of the condition that the initial point of the forming thermal cirque is outside the existing thermal cirque, but the thermal cirque is not damaged (Fig. 3a). Taking into account the Poisson character of the process, formulas (3) and (4), as well as the independence of the events under consideration, the required probability is given by the expression

$$p_0 = e^{-\lambda(a+y)\Delta u} = 1 - \lambda(a + y)\Delta u + o(\Delta u).$$

[1] The position of the thermal cirque is conditionally accepted as the position of the point at the right boundary of its chord (starting point).

[2] $o(\Delta x)$ here and below in accordance with the usual notations — an infinitely small quantity of a higher order than Δx.

[3] It is assumed that the distribution $F_0(x)$ and other distributions in the work have finite mean and variance.

[4] It is assumed that the distribution has a finite mathematical expectation and variance, as well as partial derivatives and continuous mixed derivatives.

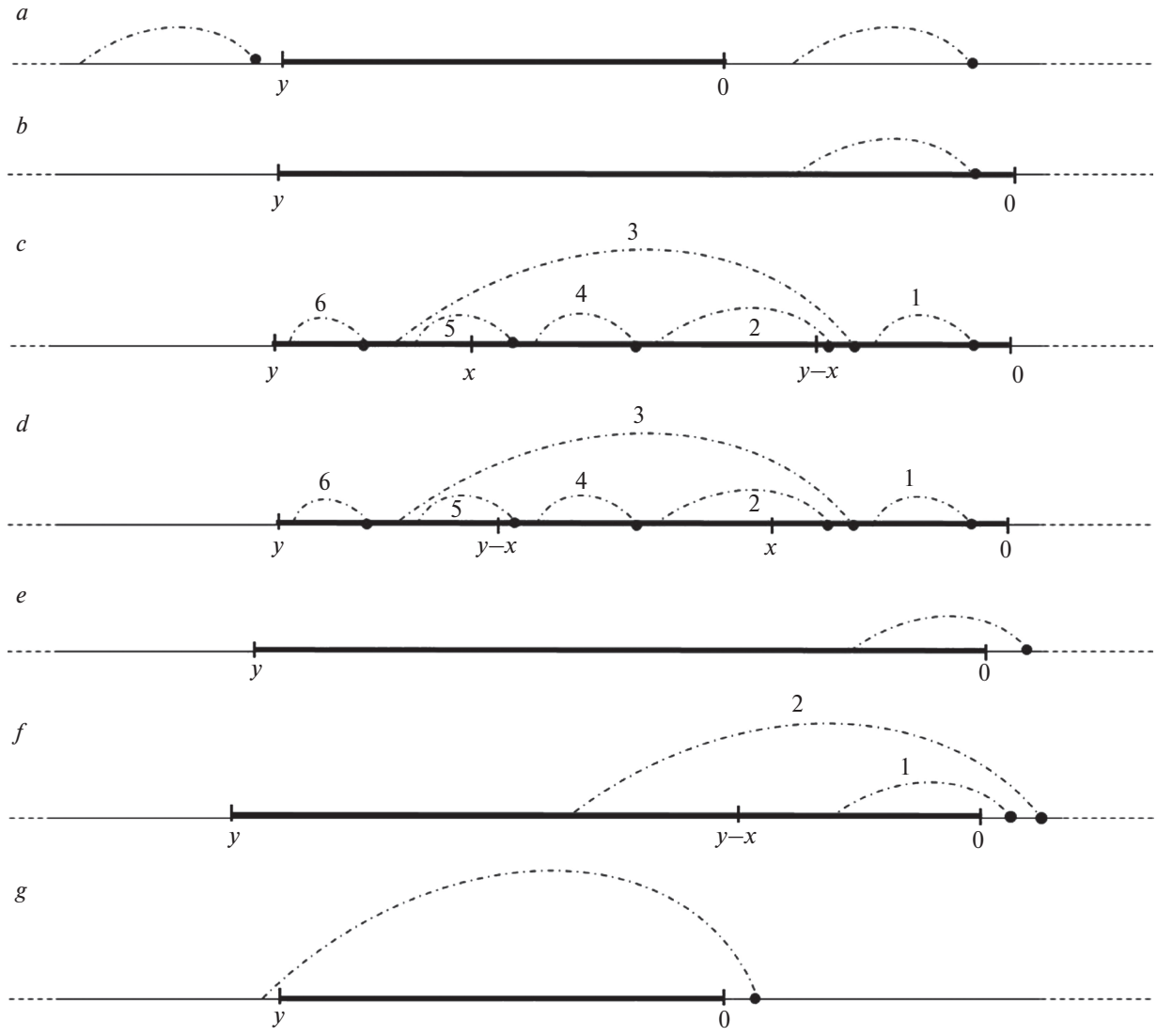

Fig. 3. Different types of interaction between the existing thermal cirque and the new thermal cirque being formed (explanations in the text); cases of interaction: *a* — no erasure, *b, c, d* — internal erasure, *e, f* — lateral erasure, *g* — complete erasure. Symbols: thin line — shoreline, thick line — chord of the existing thermal cirque under consideration, black point — initial point of the arc of the forming thermal cirque, dashed arc — arc of the forming thermal cirque, numbers — different variants of the mutual arrangement of thermal cirques.

Accordingly, the mathematical expectation of the number of thermal cirques with chord less than x at time $u + \Delta u$ given the number of thermal cirques n_0 at time u in case (a) can be obtained by integrating the probability obtained above to take into account all possible sizes of thermal cirques and then multiplying by the number of thermal cirques n_0 at the moment u,

$$N_0(x, u + \Delta u | n_0) =$$

$$= n_0 \int_0^x f(y,u)\left[1 - \lambda(a + y)\Delta u\right]dy + o(\Delta u),$$

where $f(y, u)$ is the density distribution of the thermal cirque size at time u.

The internal obliteration probability ((b) see above) of a thermal cirque of size y is determined by the fact that both first and second boundary points of the new thermal cirque are inside the existing thermal cirque, with three possibilities b1–b3:

(b1) $0 < y < x$ (Fig. 3b), in any case splitting into two residual thermal cirques with chord less than x, and taking into account the equal probability of location of the initial point on any segment Δv of the chord (assumption 1) with the probability given in expression (2), and taking into account the condition that the

chord of the new thermal cirque does not overlap the end point of the existing one (so that there is no lateral erasure), by integration we obtain the probability of internal erasure for the time interval Δu

$$p_1 = \lambda\Delta u\int_o^y F_0(y-v)dv = \lambda\Delta u\int_0^y F_0(v)dv;$$

respectively, the mathematical expectation of the number of thermal cirques given the number of thermal cirques n_0 at the moment u can be obtained by integrating the probability obtained above to take into account all possible sizes of the existing thermal cirque (y) and taking into account the formation of two new thermal cirques and then multiplying by the number of thermal cirques n_0 at the moment u,

$$N_1^1(x,u+\Delta u|n_0) = 2n_0\lambda\Delta u\int_0^x f(y,u)\int_0^y F_0(v)dvdy$$

(b2) $x < y < 2x$ (with $y - x < x$ (Fig. 3c), in this case, if the start and end points[5] of the forming thermal cirque are on the segment $[0, y-x]$ (Fig. 3c arcs 1 and 6), or the start and end points are on the segment $[x, y]$ only one residual thermal cirque with chord less than x is formed; if the initial point is on the segment $[0, x]$ and the end point is on the segment $[y-x, y]$ (Fig. 3c arcs 2–5), two thermal cirques with chord less than x are formed. Accordingly, determining the above probabilities by integration, further the mathematical expectation of the number of thermal cirques with chord less than x at time $u + \Delta u$ given the number of thermal cirques n_0 at time u can be obtained by integrating the obtained probabilities to take into account all possible sizes of the thermal cirque existing at moment u and then multiplying by the number of thermal cirques n_0 at moment u,

$$N_1^2(x,u+\Delta u|n_0) = n_0\lambda\Delta u\int_x^{2x} f(y,u)\left\{1\cdot\int_0^{y-x} F_0(y-x-v)dv + 2\int_0^{y-x}[F_0(y-v)-F_0(y-x-v)]dv\right\}dy +$$
$$+n_0\lambda\Delta u\int_x^{2x} f(y,u)\left\{2\int_{y-x}^{x} F_0(y-v)dv + 1\int_x^y F_0(y-v)dv\right\}dy + o(\Delta u)$$

Transforming and simplifying, we obtain

$$N_1^2(x,u+\Delta u|n_0) = n_0\lambda\Delta u\int_x^{2x} f(y,u)\left[2\int_{y-x}^{y} F_0(v)dv\right]dy + o(\Delta u)$$

(b3) $2x < y$ (with $x < y - x$ (Fig. 3g), in this case, if the starting point of the forming thermal cirque is on the segment $[0,x]$ and the end point is on the segment $[0, y-x]$ (Fig. 3d arcs 1 and 2), or the start point is on the segment $[x, y]$ and the end point is on the segment $[y-x, y]$ (Fig. 3d arcs 5 and 6), then only one residual thermal cirque with chord less than x is formed; in the case if the initial point of the forming thermal cirque is on the segment $[0, x]$ and the end point is on the segment $[y-x, y]$ (Fig. 3d arc 5 and 6), then only one residual thermal cirque with chord less than x is formed (Fig. 3d arc 3), then two residual thermal cirques with chord less than x will be formed; finally, if the initial and the end points of the forming thermal cirque are on the segment $[x, y-x]$ (Fig. 3d arc 4), then no residual thermal cirques with chord less than x will be formed. Accordingly, determining the above probabilities by integration, further the mathematical expectation of the number of thermal cirques with chord less than x at time $u + \Delta u$ given the number of thermal cirques n_0 at time u can be obtained by integrating the obtained probabilities to take into account all possible sizes of the thermal cirque existing at moment u and then multiplying by the number of thermal cirques n_0 at moment u,

$$N_1^3(x,u+\Delta u|n_0) = Nn_0\lambda\Delta u\int_{2x}^{+\infty} f(y,u)\left\{1\cdot\int_0^x F_0(y-x-v)dv + 2\cdot\int_0^x[F_0(y-v)-F_0(y-x-v)]dv\right\}dy +$$
$$+n_0\lambda\Delta u\int_{2x}^{+\infty} f(y,u)\left\{1\cdot\int_x^{y-x}\left[F_0(y-v)-F_0(y-x-v)\right]dv + 1\cdot\int_{y-x}^{y} F_0(y-v)dv\right\}dy + o(\Delta u)$$

Transforming and simplifying, we obtain

$$N_1^3(x,u+\Delta u|n_0) = n_0\lambda\Delta u\int_{2x}^{+\infty} f(y,u)\left[2\int_{y-x}^{y} F_0(v)dv\right]dy + o(\Delta u)$$

Summing up the mathematical expectation of the number of thermal cirques with chord less than x given the number of thermal cirques n_0 at time u for all three variants and simplifying, we obtain for internal erasure

[5] Let us recall that, in accordance with the above assumption, the endpoint of the chord is always located to the left of the starting point.

the value of the mathematical expectation of the number of thermal cirques with chord less than x

$$N_1(x,u+\Delta u|n_0) = n_0 2\lambda\Delta u\int_0^x f(y,u)\int_0^y F_0(v)dvdy +$$

$$+ n_0 2\lambda\Delta u\int_x^{+\infty} f(y,u)\int_{y-x}^{y} F_0(v)dvdy + o(\Delta u)$$

The lateral erasure probability ((c) see above) of a thermal cirque of size y is determined by having one endpoint of the newly forming thermal cirque outside the existing thermal cirque and the other endpoint inside the existing thermal cirque, with the following possibilities (c1–c2):

(c1) $0 < y < x$ (Fig. 3d), where, if the starting point is to the right of the existing thermal cirque, the probability of lateral erasure is determined by the condition that the size of the forming thermal cirque must be sufficient to encroach on the existing thermal cirque, but at the same time not overlap its end point, so that there is no complete erasure. Given the Poisson nature of the process of emergence of new thermal cirques and the long length of the bank, the equal probability of lateral erasure on both the right and left sides, simplifying, then multiplying by the number of thermal cirques n_0 at moment u, we obtain the mathematical expectation of the number of thermal cirques with chord less than x given the number of thermal cirques n_0 at moment u

$$N_2^1(x,u+\Delta u|n_0) = 2n_0\lambda\Delta u\int_0^x f(y,u)\int_0^{+\infty}\left[F_0(y+v) -\right.$$

$$\left. - F_0(v)\right]dvdy = 2n_0\lambda\Delta u\int_0^x f(y,u)\int_0^y\left[1 - F_0(v)\right]dvdy + o(\Delta u)$$

(c2) $x < y$

(Fig. 3e), in this variant, if the named conditions are fulfilled, if the end point is on the segment $[y-x, y]$ then only one thermal cirque with chord less than x is formed, in otherwise no residual thermal cirque with chord less than x is formed. Similarly to the previous one, we obtain the mathematical expectation of the number of thermal cirques with chord less than x under the condition of the number of thermal cirques n_0 at the moment u

$$N_2^2(x,u+\Delta u|n_0) = 2n_0\lambda\Delta u\int_x^{+\infty} f(y,u)\int_0^{+\infty}\left[F_0(y+v) -\right.$$

$$\left. - F_0(y-x+v)\right]dvdy =$$

$$= 2n_0\lambda\Delta u\int_x^{+\infty} f(y,u)\int_{y-x}^{y}\left[1 - F_0(v)\right]dvdy + o(\Delta u)$$

Summing up, we obtain for lateral erasure the mathematical expectation of the number of thermal cirques with chord less than x given the number of thermal cirques n_0 at time u expression

$$N_2(x,u+\Delta u|n_0) = 2n_0\lambda\Delta u\int_0^x f(y,u)\int_0^y\left[1 - F_0(v)\right]dvdy +$$

$$+2n_0\lambda\Delta u\int_x^{+\infty} f(y,u)\int_{y-x}^{y}\left[1 - F_0(v)\right]dvdy + o(\Delta u)$$

In case (d) (Fig. *3j*) of complete erasure, the mathematical expectation of the number of thermal cirques is zero.

In case (e) of appearance of new thermal cirques, the mathematical expectation of the number of thermal cirques with chord less than x, given the number of thermal cirques n_0 at the moment u appearing during the considered time interval on the whole length of the coast L, in accordance with the Poisson character of the process is equal to

$$N_4(x,u+\Delta u|n_0) = \lambda L\Delta u F_0(x)$$

Summing over all cases, and over all values of $|n_0$ taking into account their probabilities and simplifying, we obtain the mathematical expectation of the number of thermal cirques with chord less than x at time $u + \Delta u$

$$N(x,u+\Delta u) = N(u)\left[F(x,u) - \lambda a F(x,u)\Delta u +\right.$$

$$\left. + \lambda\Delta u\int_0^x yf(y,u)dy + 2\lambda\Delta u x[1 - F(x,u)]\right] +$$

$$+ \lambda L\Delta u F_0(x) + o(\Delta u)$$

where $N(u)$ is the mathematical expectation of the total number of thermal cirques at time u

Going to the limit at $x \to +\infty$ given the equality for the average size of the thermal cirque

$$h(u) = \frac{L}{N(u)} = \int_0^{+\infty} yf(y,u)dy = \frac{1}{\gamma(u)} \qquad (5)$$

where $\gamma(u)$ is the average linear density of thermal cirque locations along the shoreline, as well as the following equality from the finiteness of the second order moment of the thermal cirque size distribution function

$$\lim_{x\to+\infty}\left[x\left[1 - F(x,u)\right]\right] = 0$$

we obtain the mathematical expectation of the total number of thermal cirques at time $u + \Delta u$

$$N(u+\Delta u) = N(u) - N(u)\lambda a\Delta u + \\ + 2N(u)\lambda\Delta u\int_0^{+\infty} yf(y,u)dy + o(\Delta u).$$

Hence, dividing by L and Δu and going to the limit at $\Delta u \to 0$ it is not difficult to obtain, considering (5), the differential equation for the variation of the average linear density of the circus arrangement

$$\frac{d\gamma(u)}{du} = 2\lambda - \lambda a\gamma(u).$$

After its solution by standard methods for the initial condition $\gamma(0) = \frac{1}{a}$ (since at the initial moment there is no superposition and erasure of thermal cirques, and the average size is equal to the average size of forming thermal cirques) the change of mathematical expectation of the thermocircle size with time is given by the following expression

$$h(u) = \frac{a}{2 - e^{-\lambda a u}}. \qquad (6)$$

Let's take as probability of thermocircle of size not more than x at moment $u + \Delta u$ at large number of thermocircles the ratio of mathematical expectation of number of thermal cirque with size less than x to mathematical expectation of total number of thermal cirques at the moment $u + \Delta u$

$$F(x,u+\Delta u) = N(u)\Bigg[F(x,u) - \lambda a F(x,u)\Delta u + \\ + \lambda\Delta u\int_0^x yf(y,u)dy + 2\lambda\Delta u x[1 - F(x,u)]\Bigg] + \\ + \lambda L\Delta u F_0(x) + o(\Delta u)\Big/N(u) - N(u)\lambda a\Delta u + \\ + 2N(u)\lambda\Delta u\int_0^{+\infty} yf(y,u)dy + o(\Delta u).$$

Subtracting the probability value $F(x,u)$ at time u simplifying, dividing by Δu $N(u)$ and going to the limit at $\Delta u \to 0$ we obtain the equation for the thermal cirque size distribution

$$\frac{1}{\lambda}\frac{\partial F(x,u)}{\partial u} = \int_0^x yf(y,u)dy + 2x\big[1 - F(x,u)\big] + \\ + F_0(x)h(u) - 2F(x,u)h(u)]$$

with the conditions at the initial moment $F(x,0) = F_0(x)$ and $F(0,u) = 0$ arising from the fact that the size cannot be negative, the thermal cirques do not overlap at the initial moment, and at that moment the distribution corresponds to the size distribution of the new thermal cirques forming.

The next step is to solve the obtained equation. Passing to a new unknown function $\phi(x,u)$

$$\phi(x,u) = \int_0^x F(v,u)dv \qquad (7)$$

changing the order of differentiation in the resulting mixed derivatives[6] and integrating *over x,* we reduce the equation to the following one

$$\frac{1}{\lambda}\frac{\partial\phi(x,u)}{\partial u} + [x + 2h(u)]\phi(x,u) = x^2 + h(u)I(x) + C(u),$$

where

$$I(x) = \int_0^x F_0(v)dv$$

$C(u)$ is some function depending only on u. This equation can be regarded as a linear inhomogeneous differential equation on u, and when solved in standard way, taking into account the initial moment conditions, we finally obtain

$$\phi(x,u) = \exp(-\lambda xu - 2\lambda\int_0^u h(v)dv)\Bigg[\lambda\int_0^u [x^2 + \\ + h(s)I(s)]\exp(\lambda xu + 2\lambda\int_0^u h(v)dv)ds + \int_0^x F_0(v)dv\Bigg].$$

The desired probability distribution of thermal cirque sizes can be formed according to (7) by differentiation of the obtained solution

$$F(x,u) = \varepsilon(x,u)\Bigg[-\lambda^2 u\int_0^u \frac{x^2 + h(s)I(x)}{\varepsilon(x,s)}ds + \\ + \lambda\int_0^u \frac{2x + h(s)F_0(x) + \lambda sx^2 + \lambda sh(s)I(x)}{\varepsilon(x,s)}ds\Bigg] + \\ + \varepsilon(x,u)\Bigg[-\lambda u\int_0^x F_0(v)dv + F_0(x)\Bigg] \qquad (8)$$

where

$$\varepsilon(x,u) = \exp[-\lambda xu - 2\lambda\int_0^u h(v)dv].$$

Finally, the last step, in accordance with the task at hand, is to evaluate the behavior of the obtained distribution at large development time. Passing to the limit at $u \to +\infty$ in expression (8), twice using the Lopital rule (the conditions, as it is easy to see, are satisfied (Fichtenholtz, vol. 1, 1970. p. 151)) and the variation of

[6] The necessary conditions (Fichtenholtz, vol. 1, 1970, para. 190) are satisfied (see footnote 3).

Table 1. Results of evaluation of compliance of samples of thermal cirque sizes at key sites with different types of theoretical distributions

Plot	Sample size	Normal distribution			Lognormal distribution			Gamma distribution		
		average м	standard м	*p*	logarithmic mean	logarithm standard	*p*	λ	α	*p*
KNS1	183	50	43	0.000	3.675	0.666	0.288	22.66	2.22	0.015
KNS2	181	60	43	0.000	3.881	0.639	0.241	23.18	2.57	0.010
KNS3	181	23	15	0.000	2.951	0.586	0.782	7.63	2.99	0.131
KNS4	159	46	27	0.000	3.678	0.529	0.339	12.40	3.68	0.153
JML1	108	18	11	0.000	2.751	0.504	0.574	4.71	3.81	0.314
KLG1	113	24	89	0.057	3.108	0.156	0.254	3.51	6.87	0.331
KLG2	108	25	105	0.020	3.16	0.151	0.923	3.74	6.80	0.640
KPD1	111	31	118	0.309	3.36	0.14	0.694	3.93	7.82	0.842
CSH1	290	22	115	0.000	3.004	0.235	0.015	4.91	4.60	0.037
CSH2	278	15	100	0.000	2.532	0.312	0.545	4.622	3.21	0.113
GDN1	190	14	40	0.000	2.564	0.195	0.658	2.637	5.42	0.305
GDN2	319	22	344	0.000	2.832	0.449	0.235	9.56	2.25	0.006

Note. λ — scale parameter, α — shape parameter, *p* — parameter of agreement of distributions (the difference between empirical and theoretical distributions is statistically significant at the level of 0.99 in the case of $p < 0.01$).

the average thermal cirque size with time (6), we finally obtain that there is a limit to the probability distribution of thermal cirque sizes, and it is equal to

$$\lim_{u\to+\infty} F(x,u) = F(x) = 1 - \frac{a}{2}\frac{\left[1 - F_0(x)\right]}{\left[x + a\right]} - \frac{a}{2}\frac{a - \int_0^x \left[1 - F_0(v)\right] dv}{\left[x + a\right]^2} \quad (9)$$

where $a, F_0(x)$ are, respectively, the mathematical expectation (mean size) and size distribution of young thermal cirques forming.

The second part of the task was to carry out studies of thermocircle sizes (chord lengths) at specific sites, including obtaining samples of chord lengths for thermal cirque of each site and comparing them with theoretical distributions to identify characteristic features of the distributions[7]. As mentioned above, the key sites were selected based on the requirements of relative morphological homogeneity of the site and homogeneity of physiographic, primarily geological and geomorphologic, conditions; thus, there are no significant physiographic differences within each site.

The slope edges were delineated on the images and the arc-shaped boundaries of thermal cirques with the adjacent watershed surface were delineated, and the chords of the arcs were drawn. The chords were measured using ArcGIS. The obtained samples were compared with theoretical distributions of various types; the comparison was performed using the chi-square test (Pearson's criterion) in the Statistica program in compliance with the standard requirements of the methodology in terms of the sample volume and the size of partition intervals.

The sites vary considerably in terms of conditions. For example, according to the state geologic maps at a scale of 1:200 000 are composed of marine, glacial, lacustrine-glacial, alluvial-marine and lacustrine-alluvial sediments from the surface; the sediments are represented by both sands and siltstones, gravel-pebble sediments, sandy loams and loams with boulders and pebbles, as well as silty-fine sandy sediments; permafrost rocks have both discontinuous and massive-island and continuous distribution. In climatic terms, the areas belong to either the Arctic or Subarctic belts.

The results of statistical processing for all sites are summarized in Table 1.

The analysis of the similarity of empirical distributions of chord lengths with different types of theoretical distributions (normal, lognormal, and gamma distribution) gives interesting results. All twelve plots show agreement with the same type of distribution, the lognormal distribution, at a significance level of 0.99. This is fulfilled when there is a significant difference in the values of the distribution parameters at different sites. The gamma distribution also agrees with the empirical data, but slightly worse; this can be explained by the general similarity of the lognormal distribution and the gamma distribution. The normal distribution does not agree with the empirical data at any site.

[7] Performed jointly with M.V. Arkhipova, V.V. Bondar, T.V. Gonikov (Victorov et al., 2023).

Figure 4 shows examples of the correspondence between empirical distributions and theoretical lognormal distributions for different sites.

OBSERVATION

Thus, mathematical modeling of the process of change in the morphological pattern of abrasion banks of the cryolithozone has shown that in different physical-geographical and geocryological conditions, a stable stationary distribution of the sizes of thermal cirques is formed under significant development time. This distribution is formed in the conditions of constant appearance of new thermal cirques, as well as complete or partial (internal and lateral) erasure of existing ones; therefore, the distribution of thermal cirque sizes observed at each moment, first of all, on the materials of space imagery, coincides with the distribution of sizes of new thermal cirques being formed. Thus, the obtained result allows us to conclude that the morphological pattern of the abrasion coast, being in constant change, nevertheless, with a significant development time, has a stationary distribution of the sizes of thermal cirques, their constant average size and average density, i.e., it is in a state of dynamic equilibrium. Interestingly, the analysis shows that the limiting distribution does not depend on the distribution of thermal cirque sizes at the initial moment $F(x,0)$.

The physical-geographical, geological-geomorphological, and geocryological conditions do not affect the existence of the limiting distribution, but affect the character of this distribution through the size distribution of young thermal cirques formed; the relationship is described by expression (9). At the same time, the density of thermal cirque generation (λ) does not influence the limiting size distribution, apparently affecting only the rate of convergence to the limiting distribution.

It should be emphasized that we have previously proposed a variant of the model for the development of morphological pattern of abrasion banks (Victorov, 2022), but it used a significant simplification — it neglected internal erosion, which greatly facilitated the analysis, but made it less accurate. Thus, the present model is a new and much better one.

Comparison of empirical distributions of observed thermal cirque sizes with the results of mathematical modeling allows us to conclude that the same type of size distributions of forming young thermal cirques is characteristic of different physiographic, in particular geological-geomorphological and geocryological conditions. This follows from the uniformity of the observed distributions of thermal cirque sizes (lognormal distributions) and the established dependence between distribution of the sizes of forming young thermal cirques and the observed distributions of thermal cirque sizes described by expression (9). The same expression allows us to predict, in a more detailed analysis, the quantitative characteristics of the thermal cirque formation process (and, accordingly, of the landslides that start the formation of thermal cirque), namely, the size distribution of emerging new thermal cirques and landslides, by measurements of the observed sizes from the materials of a single high-resolution space imagery and, accordingly, by the probability distribution of these sizes.

The results obtained are also significant in practical terms for predicting the development, in particular, the retreat, of coasts, due to the previously established correlations between the sizes of thermal cirques and the arrows of the arcs bounding them (Victorov et al., 2023), which are closely related to the rate of retreat.

CONCLUSIONS

Abrasion shores of the cryolithozone develop under the action of a complex of processes including both increase and decrease in the number of thermal cirques due to the formation of new thermal cirques and, to a greater or lesser extent, erasure of existing ones; therefore, the distribution of thermal cirque sizes observed at each moment, first of all on the materials of space imagery, generally does not coincide with the distribution of sizes of new thermal cirques being formed.

The complex of mathematical modeling and space methods allowed us to show that in different physiographic and geocryological conditions, a stable stationary distribution of the sizes of thermal cirques of abrasion shores of the Arctic cryolithozone is formed in different physiographic and geocryological conditions with a significant development time at homogeneous sites. Differences in the conditions of different sites do not affect the fact of existence of the limiting stationary distribution. Thus, the morphological pattern of the abrasion shore, being in constant change, nevertheless has a stationary distribution of the sizes of thermal cirques, their constant average size and average density, i.e. it is in a state of dynamic equilibrium.

The dependence of stable stationary distribution of abrasion bank thermal cirque sizes on the size distribution of forming young thermal cirques is obtained. Physical-geographical, geological-geomorphological and geocryological conditions of the sites influence the character of the stationary limiting distribution through the size distribution of young thermal cirques forming.

Comparison of empirical distributions of thermal cirque sizes observed from space imagery with the results of mathematical modeling allows us to conclude that different physiographic, in particular, geological-geomorphological and geocryological conditions are characterized by the same type of size distribution of forming young thermal cirques; the conditions affect only the values of distribution parameters.

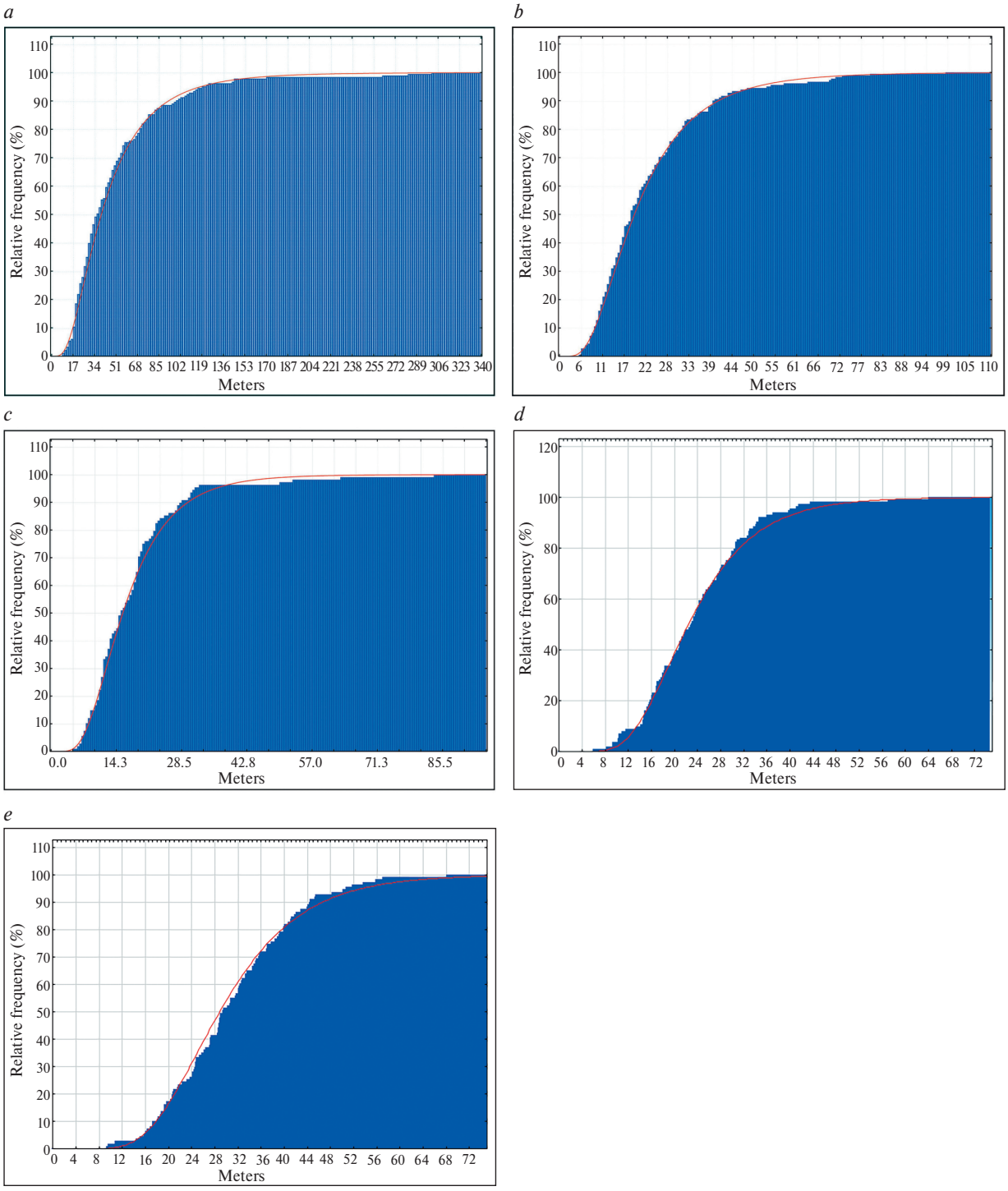

Fig. 4. Examples of correspondence between empirical distributions (blue contour) and theoretical lognormal distributions (red line) for key sites (*a* — KNS1, *b* — KNS3, *c* — JML1, *d* — KLG1, *e* — KHPD1)

The obtained results make it possible to predict the quantitative characteristics of the thermal cirque formation process, namely, the size distribution of emerging new thermal cirques, based on measurements of the observed thermal cirque sizes using the materials of a single high-resolution space imagery; this is essential in forecasting the development, in particular, the coastal retreat due to the existing correlation between the thermal cirque sizes and the arrows of the arcs bounding them.

FUNDING

The research was carried out within the framework of the state order topic No. FMWM-2022-0010.

REFERENCES

1. *Aleksyutina D.M., Shabanova N.N., Kokin O.V., Vergun A.P. et al.* Monitoring and modelling issues of the thermoabrasive coastal dynamics // In IOP Conf. Series: Earth and Environmental Science, 2018. No. 193. No. 012003.

2. *Belova N.G., Novikova A.V., Günther F., Shabanova N.N.* Spatiotemporal variability of coastal retreat rates at Western Yamal Peninsula, Russia, based on remotely sensed data // J. of Coastal Research. 2020. No. 95. Pp. 367–371.

3. *Belova N.G., Shabanova N.N., Ogorodov S.A., Kamalov A.M., Kuznetsov D.E., Baranskaya A.V., Novikova A.V.* Dynamics of thermal abrasion coasts of the Kara Sea in the area of Cape Kharasavey (Western Yamal) // Kriosfera Zemli. 2017. Vol. 21. No. 6. Pp. 85–96. https: //doi.org/10.21782/KZ1560-7496-2017-6(85-96). (In Russian).

4. *Fikhtengolts G.M.* Kurs differentsial'nogo i integral'nogo ischisleniya (Course of differential and integral calculus) Vol. 1. Moscow, Nauka, 1970. P. 608 (In Russian).

5. *Khomutov A.V., Leibman M.O.* Landscape controls of thermodenudation rate change on Yugorsky peninsula coast // Kriosfera Zemli. 2008. Vol. XII. No. 4. Pp. 24–35. (In Russian).

6. *Kizyakov A.I.* The dynamics of thermodenudation processes at the yugorsky peninsula coast // Kriosfera Zemli. 2005. Vol. IX. No. 1. Pp. 63–67. (In Russian).

7. *Leibman M., Kizyakov A., Zhdanova Y, Sonyushkin A., Zimin M.* Coastal Retreat Due to Thermodenudation on the Yugorsky Peninsula, Russia during the Last Decade, Update since 2001–2010. // Remote Sensing. 2021. 13. 4042. P. 21. https://doi.org/10.3390/rs13204042.

8. *Novikova A.V.* Morphology and dynamics of thermal abrasion coasts of the Kara Sea: PhD thesis. — Moscow.: 2022. P. 26 (In Russian).

9. *Pizhankova E.I., Dobrynina M.S.* Dynamics of the coast of the Lyakhovsky Islands (results of interpretation of aerospace images). // Kriosfera Zemli. 2010. Vol. XIV. 4. Pp. 66–79. (In Russian).

10. *Sovershayev V.A.* Cryogenic processes and phenomena on the coast and shelf of the Arctic seas // Dinamika arkticheskikh poberezhiy Rossii (Dynamics of the Arctic coasts of Russia.) Moscow, Izd-vo MGU, 1998. Pp. 12–18. (In Russian).

11. *Vasiliev A.A., Pokrovsky S.I., Shur Yu.L.* Dynamics of thermal abrasion shores of the western Yamal // Kriosfera Zemli, 2001. Pp. 44–52. (In Russian).

12. *Victorov A.S.* Modeling Morphological Features of Abrasion Landslide Coasts in Cryolithozone // Geoekologiya. Inzhenernaya geologiya. Gidrogeologiya. Geokriologiya. 2022. No. 6. Pp. 28–36.

13. *Victorov A.S., Orlov T.V., Arkhipova M.V., Kapralova V.N., Bondar V.V.* Quantitative lows of a morphological pattern for abrasion slopes with a landslide process within the cryolithozone (the coasts of the Kanin and Yamal peninsulas as examples) // Geomorfologiya i paleogeografiya. 2023. Vol. 54. No. 3. Pp. 124–137. https://doi.org/10.31857/S294917892303012X; https://elibrary.ru/WETHFU

EARTH RESEARCH FROM SPACE, 2025, No. 1, pp. 35–46

USING SATELLITE INFORMATION ABOUT THE EARTH

MAPPING OF HYDROTHERMAL-METASOMATIC ALTERATION FOR PREDICTION GOLD MINERALIZATION BASED ON PROCESSING A DATASET OF THE LANDSAT 8 REMOTE SENSING SPACECRAFT FOR THE TERRITORY OF THE EASTERN SLOPE OF THE POLAR URALS

© 2025 Yu. N. Ivanova[a, b, *]

[a] *Institute of Geology of Ore Deposits, Petrography, Mineralogy and Geochemistry of the Russian Academy of Sciences, Moscow, Russia*

[b] *RUDN University, Moscow, Russia*

**e-mail: jnivanova@yandex.ru*

Received June 24, 2024

Abstract. Based on satellite imagery from Landsat 8, an analysis was made of the territories of the eastern slope of the Polar Urals that are promising for identifying gold mineralization (from north to south): Shchuchinskaya zone (Yunyaginskoye deposit), Toupugol-Khanmeishorsky ore district (Novogodnee-Monto and Petropavlovskoye deposits) and the central part of the Malouralskaya zone (Manyukuyu-Vorchatinsky ore cluster). The study was carried out with the aim of identifying similar features in the distribution of metasomatic changes in order to develop a prediction criterion (material) for the gold ore type of mineralization. It was found that in areas promising for Au mineralization on the eastern slope of the Polar Urals, intrusions of basic composition should be localized, with which gold mineralization is genetically associated and metasomatic halos of a significant area (more than 30 km^2) with increased values of iron (III) oxide indices should be localized. And iron (II) oxide, and to a lesser extent — iron oxides and hydroxides (limonite), as well as hydroxyl-(Al-OH, Mg-OH) and carbonate-containing minerals.

Keywords: *gold mineralization, lineaments, morphostructures, hydrothermal-metasomatic alteration, the Polar Urals, Landsat 8*

DOI: 10.31857/S020596142501046e6

INTRODUCTION

Spectral methods of Earth remote sensing (ERS) in the practice of geological exploration began to be used in the 1970s due to the introduction of multispectral photographs of the Earth's surface. Today such methods are widely used along with traditional methods (geological, geophysical, geochemical, etc.) to predict various types of ore mineralization (di Tommaso, Rubinstein 2007; Zhang et al. 2007; Pour, Hashim, 2011; Amer et al., 2012).

The Arctic has recently attracted a lot of attention from scientific communities around the world, and more and more scientific missions are targeting the region because of the vast and diverse mineral resources (MRs) that are still poorly explored.

Many specific challenges in the Arctic, including the prediction of ore deposits, can also be addressed by space-based technologies, which provide many advantages for research and development projects in the area, enabling large-scale and relatively cost-effective observations and data collection in a region with limited ground-based infrastructure (Bohlmanna and Koller, 2020).

Currently, there are very few papers in specialized journals and books devoted to remote sensing on the topic of predicting ore mineralization and mapping metasomatic changes in the Arctic territory (e.g., Pour and Hashim, 2012; Graham et al., 2017; Ivanova et al., 2022, 2023, etc.).

This paper presents the results of mapping of metasomatic change using multispectral satellite images from the Landsat 8 remote sensing spacecraft (RS) for areas of the eastern Polar Urals, part of the Russian Arctic. This study will help to identify a material prediction criterion for gold mineralization, which can be used as an auxiliary tool for MRs exploration in other areas of the Polar Urals and northern latitudes.

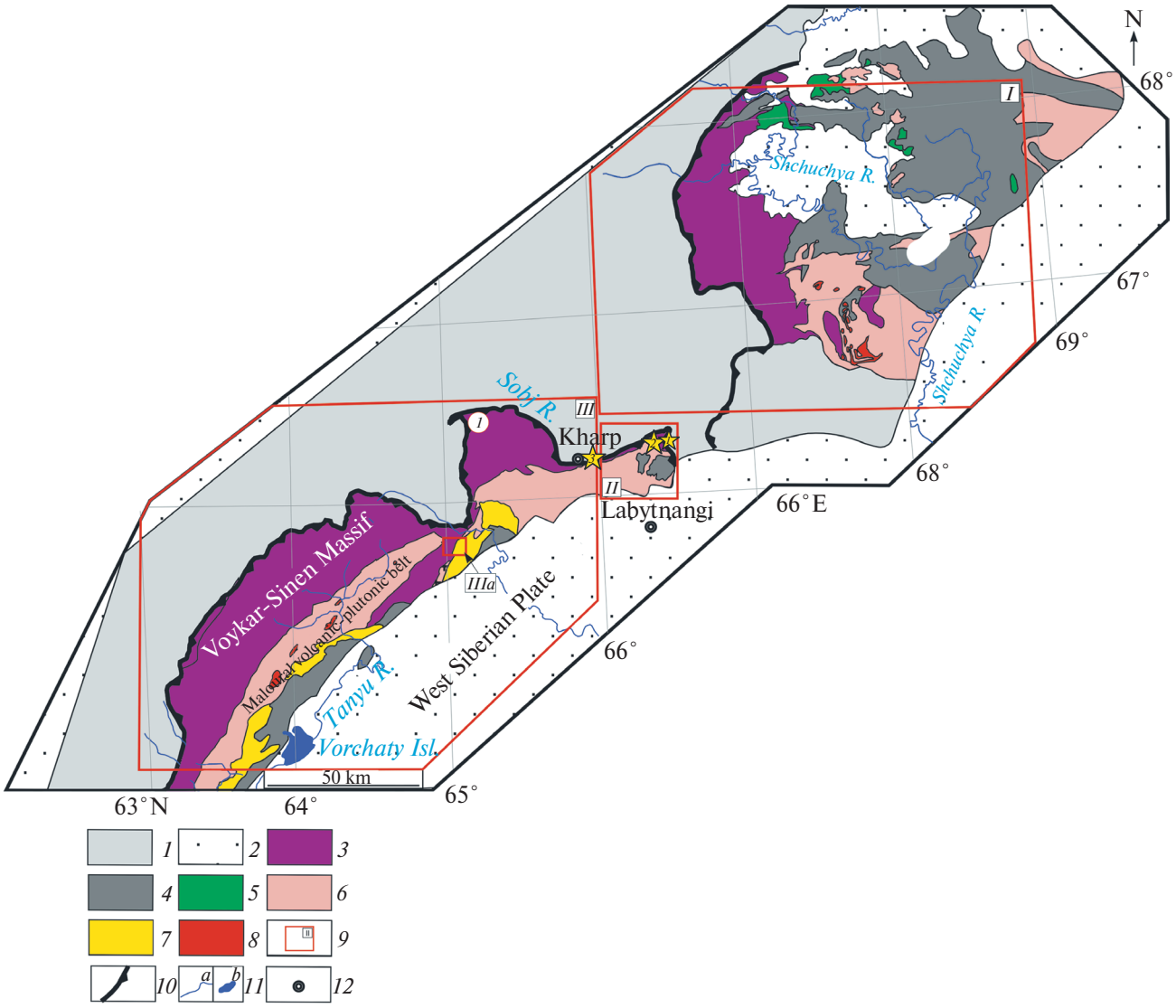

Fig. 1. Tectonic scheme of the Ural fold belt (from State..., 2007): *1* — Late Cambrian and Paleozoic formations of the West Ural structural megazone; *2* — Mesozoic-Cenozoic cover of the West Siberian plate; *3–9* — East Ural megazone (the Shchuchya zone is localized above 66°30'E, the Voykarskaya zone — below 66°30' E): *3* — Ordovician metamorphosed hyperbasites and gabbroids; *4* — Ordovician-Devonian volcanic and volcanogenic-sedimentary formations; *5* — Middle-Late Ordovician gabbroids and plagiogranitoids of the Khoipei complex; *6* — Early-Middle Devonian diorites and granitoids of the Yunyaginsky and Sobsky complexes; *7* — Early-Middle Devonian gabbroids, diorites and monzonitoids of the Kongor complex; *8* — Middle-Late Devonian granitoids of the Yurmenek and Janoslorsk complexes; *9* — boundaries of the studied areas: Shchuchinskaya zone (*I*), Toupugol-Khanmeyshorsky ore district (*II*), central part of Malouralskaya zone (*III*), Manyukuyu-Vorchatinsky ore junction (*IIIa*); *10* — MUF; *11* — main rivers and lake; *12* — towns. Yellow asterisks show: deposits Novogodneye-Monto (1), Petropavlovskoye (2) and ore occurrence Amphibolitovoye (3), number one shows the Rai-Iz massif.

The following areas (from north to south) were selected: Shchuchinskaya zone (Yunyaginskoye deposit), Toupugol-Khanmeyshorsky ore district (Novogodneye-Monto and Petropavlovskoye deposits) and the central part of Malouralskaya zone (Manyukuyu-Vorchatinskoye ore cluster), which are the most promising for identification of gold mineralization.

GEOLOGICAL STRUCTURE OF THE STUDY AREAS

The Polar-Ural segment of the East Ural megazone divided into the Shchuchinskaya and Voykarskaya zones (Fig. 1).

These zones are characterized by sedimentary-volcanogenic deposits with widely manifested

plutonic and hypabyssal magmatism, relatively weak dynamothermal and intense dislocation metamorphism. The formations correspond to the settings of oceanic rifting of island-arc systems and active continental margin (Puchkov and Ivanov, 2020).

The Shchuchinskaya zone is the northernmost part of the Paleozoic island-arc system of the Urals. In the west, it is bounded by a regional fault that is part of the Main Ural Fault (MUF) system. It is a large thrust fault overlain by Mesozoic sediments to the east. Its fragment frames the Shchuchinsky synclinorium in the form of arc-shaped faults that merge into a single semicircular structure.

In the structure of the Shchuchinskaya zone there are several segments, within which the following are established: Paleozoic cover-fold structures represented by rocks of Ordovician, Silurian, Devonian, Carboniferous, overlain by platform Mesozoic sediments of Jurassic and Triassic. The most widespread development among the plutonic formations is represented by gabbroids, granitoids are much less widespread and are localized in the form of small shtokoshaped massifs up to 10–16 km^2 (Dushin, 2020).

For example, manifestations and deposits of V±Ti-Fe-ore and Cu-Fe-scarne formations are associated with magmatic and volcanogenic-sedimentary rocks of the basic composition of the Vaskieu and Harampei-Maslov complexes, as well as the Yanganapei Formation. Sedimentary rocks of Malapaipudynskaya and Khantey formations host occurrences of Pb-Zn mineralization. The magmatic rocks of the main composition of the second phase of the Harbey-Sob complex are associated with manifestations of Mo, Pb-Zn, Cu-quartz and skarn-magnetite mineralization. The magmatic rocks of acidic composition of the Syadatayakhinskiy and Evyuganskiy complexes include deposits and occurrences of As, Au, Mo and Cu mineralization. Cu and Au mineralization is localized in sedimentary rocks of the Khoidyshorsk and Usinskaya Formations, and polymetallic mineralization is localized in metamorphic and sedimentary rocks of the Orang Formation. Cr occurrences are spatially and genetically associated with magmatic rocks of ultrabasic composition of the Syum-Keu complex and dikes of serpentinites of the Hartmannushor complex. Eclogite-like rocks of the Slyudyanogorsk complex contain occurrences of metamorphogenic Ti (Zyleva et al., 2014).

The second phase of the gabbro-granodiorite-granite Yunyaginsky complex can be separately identified for this zone, which is genetically associated with gold-bearing skarn-magnetite deposits and ore occurrences localized in the ore cluster of the same name. The Yunyaginskoye deposit is currently of industrial interest. In addition to this object, the ore cluster hosts a number of ore occurrences and mineralization points of Cu-Fe-ore skarn with Au, Ti-Fe-ore mafic (Volkovsky type), Ti-Fe-ore ultramafic-mafic (Kachkanar type) and Ti-Fe-ore metamorphogenic formations (Zyleva et al., 2014; Andreichev et al., 2017).

The Yunyaginskoye deposit is located 10 km east of the Obskaya-Bovanenkovo railway line. Other known promising ore occurrences and mineralization points are much less well studied.

A more detailed geological description of the Shchuchinskaya zone can be found in articles and published reports (Zyleva et al., 2014; Remizov et al., 2014; Andreichev et al., 2017; Sobolev et al., 2018; Dushin, 2020; Puchkov and Ivanov, 2020, etc.).

The Voykarskaya zone has a submeridional SSW direction and is a series of allochthons dipping gently to the SE. The zone is significantly tectonized and is broken by thrusts into separate plates. The allochthons consist of volcanogenic and terrigenous-volcanogenic rocks of Paleozoic age of oceanic and supra-subduction origin. The footwall of the allochthons (in the western part of the Voykarskaya zone) is bounded by the MUF. The eastern part of the zone is composed of Early-Middle Paleozoic and Late Precambrian blocks of variously metamorphosed ultramafic and basic rocks of ophiolite association. These blocks compose the Rai-Iz and Voykar-Syninsky mountain massifs in the axial part of the Ural Ridge (see Fig. 1). East of the MUF are the Devonian supra-subduction plutonic, hypabyssal, and associated predominantly volcanic and volcanogenic-sedimentary formations (Upper Devonian – Upper Silurian) of the Eastern Subzone (Malouralskaya zone) (Remizov et al., 2014).

In the Middle Paleozoic (Upper Ordovician – Lower Carboniferous), the Malouralskaya zone was either an island arc (Upper Ordovician – Lower Devonian), which was replaced in the Early Devonian by a marginal continental volcanic-plutonic belt (Yazeva and Bochkarev, 1984), or an island arc formed on a heterogeneous basement (Kuznetsov et al., 2000). In the north and west of the Voykara subzone, the Voykar-Syninsky and Rai-Iz massifs are framed from the south and east by a band of gabbro-amphibolites. In the east there are Ordovician-Devonian island-arc plutonic and sedimentary-volcanic complexes, united into the Malouralskaya subzone. In the east of the Malouralskaya subzone, volcanic strata (Upper Ordovician – Middle Devonian) with thin interbeds of sedimentary rocks broken through by intrusions of different compositions (from gabbro to granitoids) come to the surface (State..., 2007). These volcanic strata are part of the Paleozoic island-arc system of the Polar Urals, which developed most likely as a mature island arc in the Eifelian and up to the Permian collision with the East European continent (Estrada et al., 2012; Vikentyev et al., 2017).

The Toupugol-Khanmeyshorsky ore district is localized at the NE end of the Malouralsky volcanic-plutonic belt and represents a local volcanic-tectonic uplift complicating the volcanic-tectonic depression, and is confined to the intersection of submeridional, NE and NW direction fault zones, which limit it and

control the position of gold deposits and occurrences. The NE-direction faults determine the block structure of the ore district and determine the position of intrusive bodies, dikes and apophyses of the Sobsky pluton. All the formations of the district are broken by dikes and sills of gabbro-dolerites and lamprophyres of the Malokhanmei complex (Lower Carboniferous). Two deposits are localized here: Petropavlovskoye (Au-porphyry) and Novogodneye-Monto (Au-Fe-scarn) (see Fig. 1), as well as a number of ore occurrences — Zapadnoye, Karachentseva, Karyernoye, etc. (Fig. 3). (Fig. 3) — of Fe-Au-skarn, gold-quartz and gold-porphyry types (Vikentyev et al., 2017).

The Manukuyu-Vorchatinsky ore cluster consists of volcanogenic and volcanogenic-sedimentary rocks of the Malouralsky Formation (Upper Silurian-Upper Devonian (second phase of the Kongor complex)) interrupted by intrusive formations of the Sobsky and Kongorsky complexes. The suite is characterized by facies uncontainment and is composed of clastic tuffs and tuffites of pyroxene-plagioclase andesibasalts with flows of basalts and andesibasalts, interlayers of tuffites and tuff sandstones. Bioherms composed of reefogenic limestones are occasionally encountered (Shishkin et al., 2009; Kremenetsky et al., 2012). In general, the petrogeochemical composition and petrographic features of volcanic and tuffogenic rocks of the formation indicate that they occurred as a result of explosive activity of central-type volcanoes in a paleogeodynamic setting of subduction stage (Shishkin et al., 2009). The alternation of volcanogenic and sedimentary rock packs in the section indicates periodic activation of volcanic activity during the accumulation of the formation rocks.

Intrusive complexes include formations of the Sobsky (Lower-Middle Devonian) and Kongor (Upper Devonian – Lower Carboniferous) complexes. The Sobsky complex consists of large intrusions of gabbro, diorite, and tonalite that flank a band of volcanics to the west. Small intrusions and dyke formations occurring among the volcanic fields: gabbro, gabbro-diorites, diorites, and montsodiorites are referred to the Kongor complex (Shishkin et al., 2009).

Various objects with iron ore mineralization have been identified here. The most promising are contact-metasomatic (skarn), hydrothermal-sedimentary, magmatic, Ti-magnetite types (First and Third Ore Hills). There are also few manifestations of Ti and Mo mineralization. In addition, Cu mineralization is widely manifested, which is represented both by copper ore and complex objects where Cu is associated with Pb and Zn, Ag, Au, Mo and other metals (manifestations of Yanaslorskoye, Elkoshorskoye, Mokry Log, Osenneye, etc.)

More detailed geological structure of the central part of the Malouralskaya zone and the Toupugol-Khanmeyshorsky ore district can be found in published reports (Galliulin et al, 2005; Perminov et al., 2009, etc.; Butakov et al., 2012; Kremenetsky, 2012; Zyleva et al., 2014; Remizov et al., 2014, etc.) and papers (Chernyaev et al., 2005; Koenig, Butakov, 2013; Vikentyev et al., 2017).

INITIAL DATA

Cloudless daytime scenes of Landsat-8 satellite were obtained:

Shchuchya zone: LC08_L1TP_165012_20161001_20170320_01_T1 (01.10.2016) and LC08_L1TP_165013_20161001_20170320_01_T1 (01.10.2016.); Toupugol-Khanmeyshorsky ore district: LC08_L1TP_165013_20161001_20170320_01_T1 (01.10.2016); central part of Malouralskaya zone: LC08_L1TP_166013_20160821_20170322_01_T1 (21.08.2016).

The images were obtained from the Earth Observation Satellite Data Acquisition and Delivery Information System (EOSDIS) (https://search.earthdata.nasa.gov).

Geological information for the study areas is presented in the form of geologic maps of preQuaternary formations and MRs maps (map scale 1:1000000, sheets Q-41 and Q-42), which were compiled as part of the state assignment of the Karpinsky Institute in 2007 and 2014 (Shishkin et al., 2007; Zyleva et al., 2014).

RESEARCH METHODS

Lineament analysis. Lineaments are straight or approximately linear landforms that are widespread on the Earth's surface and are closely related to the underground hidden and surface structural elements of the discontinuity framework. The orientation and number of lineaments reflect the fracture patterns of rock masses and can carry valuable information about geologic structures, tectonics, and PI localization (e.g., Ekneligoda and Henkel, 2010; Masoud and Koike, 2011).

Lineament analysis is widely used for structural studies (Thannoun, 2013; Milovsky et al., 2021; Ivanchenko et al., 2022), caldera delineation (Ananyev, 2017; Verdiansyah, 2019), assessment of mineralization prospects (Lesniak et al., 2022; Korotkov, 2023), etc.

The methodology for manual lineament extraction based on space images (SI) is given in (Ivanova et al., 2020).

The results of lineament and morphostructural analysis for the study areas can be found in (Vikentiev et al., 2021; Ivanova and Nafigin, 2023; Ivanova, 2024).

Minerals cannot be identified directly by SI, but fields of metasomatic change rocks with pronounced spectral characteristics of absorption and reflection, which are fixed in the range of the remote sensing

satellite sensor, can be identified. Therefore, the band ratio method (band ratios) is widely used to map metasomatic change minerals and lithologic units (Maurer, 2013; Korotkov, 2023). This method enhances the spectral features of image pixels based on the calculation of the ratio of spectral reflectance of one channel to another (Mather, 1999). Such channels are selected based on the reflectance of the mineral being searched for. In this case, the channel characterizing the highest reflecting or emitting ability of mineral should be located in the numerator, and the lowest one in the denominator. As a result, the sought mineral (or their group) will be expressed by bright pixels in the obtained image.

Several mineralogical indices have been developed to map the development fields of metasomotic change minerals using spectral channels of Landsat-8 satellite (Pour et al., 2018): 4/2 — iron oxide and hydroxide group minerals (hematite, magnetite, goethite, ilmenite), as well as jarosite and their mixture — limonite; 6/4 — mineral associations dominated by iron (II) oxide (magnetite); 6/5 — mineral associations with predominance of iron (III) oxide (hematite); 6/7 — hydroxyl-bearing (Al-OH and Fe,Mg-OH), carbonate (calcite and dolomite) and sulfate (gypsum) minerals. These indices are considered as weight indicators (indicators) of Fe^{3+}, Fe^{2+}, Al/Fe-OH, Mg-Fe-OH and Si-OH groups of minerals of hydrothermal nature and products of their hypergenesis.

The principal component analysis (PCA) is a multivariate statistical method that selects uncorrelated linear combinations (eigenvector loadings) of variables such that each extracted component has the smallest variance. More details of the method can be found in (Jolliffe, 2002; Jensen, 2005; Cheng et al., 2006; Gupta, 2017). The first principal component (PC1) is used to extract structural information from the image as it is characterized by the largest variance in the space of all features (Jolliffe, 2002).

PCA converts a correlated data set into uncorrelated linear data. PCA is widely used for mapping metasomatic change minerals and lithologic units based on remote sensing satellite spectral channel-sensors (Loughlin, 1991). This method is applied to the analysis of previously derived mineralogical indices using a covariance matrix. Such an approach allows us to statistically assess the reliability of the spatial distribution of relevant secondary minerals in the study area.

As input data for PCA traditionally act spectral channels of SI, but for the most effective statistical assessment of the reliability of the spatial distribution of relevant hydrothermal minerals in the study area the results of mineralogical indices estimation with the use of covariance matrix were used.

Systematization and generalization of data was performed in QGIS software environment. All available data were collected and visualized in a single GIS project.

RESULTS

For each area, four types of metasomatic change were identified in the SI analysis, represented predominantly by different mineral groups and separately shown in Figs. 2, 3, 5.

For the territory of the Shchuchya zone, the distributions of iron (II) oxide and iron (III) oxide, especially with high content, generally coincide. At that, the greatest accumulation of medium and high concentrations is localized in the north, west and south of the territory. To a lesser extent, the location of elevated values of hydroxyl-(Al-OH, Mg-OH) and carbonate-bearing minerals, and iron oxides and hydroxides (limonite) coincides (see Fig. 2).

This can be explained by the presence of overlying strata in the form of later sedimentary complexes (e.g., the Yany-Manyinsky, Tolya, Teuntoysha and Laborov Formations), which are represented by a variety of sedimentary rocks (sands, gravels, pebbles, conglomerates, lignite beds, siltstones, sandstones, coal clays, clays) up to 450 m thick.

In addition, iron (II) oxide and iron (III) oxide minerals in the ores of the Yunyaginskoye deposit form complex assemblages (poikilitic, myrmekite-like) with both ore (including hematite and pyrite) and nonore minerals (Zyleva et al., 2014).

Researchers of the Karpinsky Institute (Zyleva et al., 2014) have identified beresitization zone in this area, to which objects of Mo, Au, Au-Fe and Pb-Zn mineralization belong (see Fig. 2).

These zones are poorly reflected in the obtained remote sensing results, which is also due to the large thickness of Quaternary sediments. In places where sediments are reduced in thickness, their coincidence is observed (mountainous areas).

The main factors controlling the location of Mo mineralization on the territory of the Shchuchinskaya zone are magmatic (ore-generating acidic intrusions of pre-Ordovician complexes) and hydrothermal-metasomatic (ore-bearing and ore-bearing greisen, vein stockworks).

Most iron ore objects (Cu-Fe-ore skarn (Au-bearing) formation) belong to two genetic types: magmatic and contact-metasomatic. For both, the main ore-controlling factor is also magmatic. The main intrusives are both ore-generating and ore-bearing. Acidic plutonites (Lower-Middle Devonian) provide skarn formation localized exclusively in sedimentary-volcanogenic Silurian strata, which are intruded by granitoids of the Sobsky and Yunyaginsky complexes.

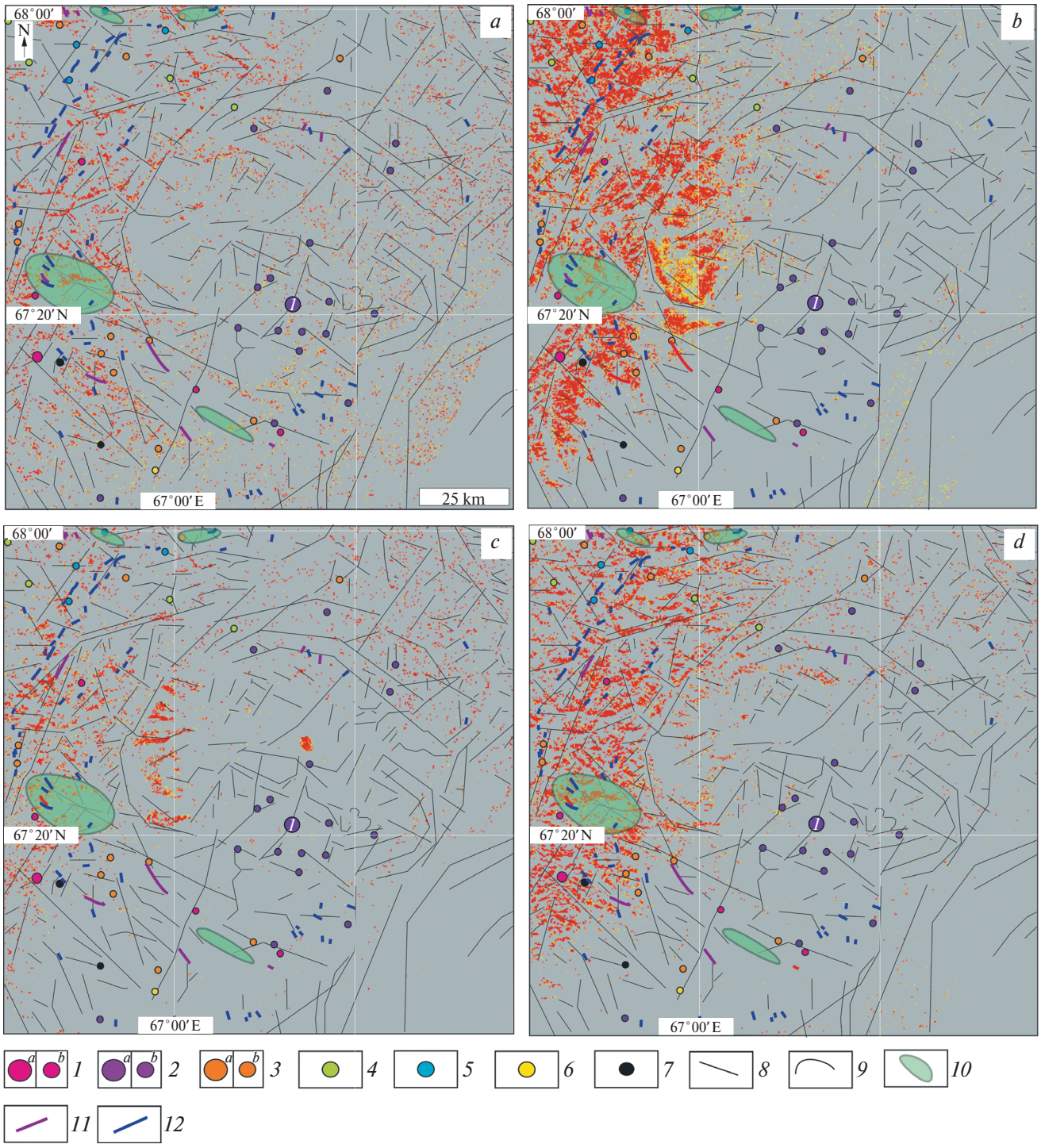

Fig. 2. Schemes of development of metasomatic change mineral associations for the Shchuchinskaya zone, obtained as a result of Landsat 8 satellite SI processing, with lineaments delineated manually, according to Landsat 8 satellite SI: *a* – hydroxyl- (Al-OH, Mg-OH) and carbonate-bearing, *b* — iron (III) oxides (hematite), *c* — iron oxides and hydroxides (limonite), *d* — iron (II) oxides (magnetite). Concentrations of indicator groups of metasomatic changes are shown by colored dots: minimum — yellow, average — orange and maximum — red. *1–7*: deposits (*a*), ore occurrences (*b*): *1* — Mo, *2* — Fe, *3* — Au, Au-Fe, *4* — Cu, *5* — Pb-Zn, *6* — As-Mo-Au, *7* — Ti; *8–9* — radial (*8*) and arc (*9*) lineaments, *10* — beresitization zone, *11–12* — dikes of basic (*11*) and acidic (*12*) composition taken from the geological map (Zyleva et al., 2014). Numder one shows the Yunyaginskoye deposit.

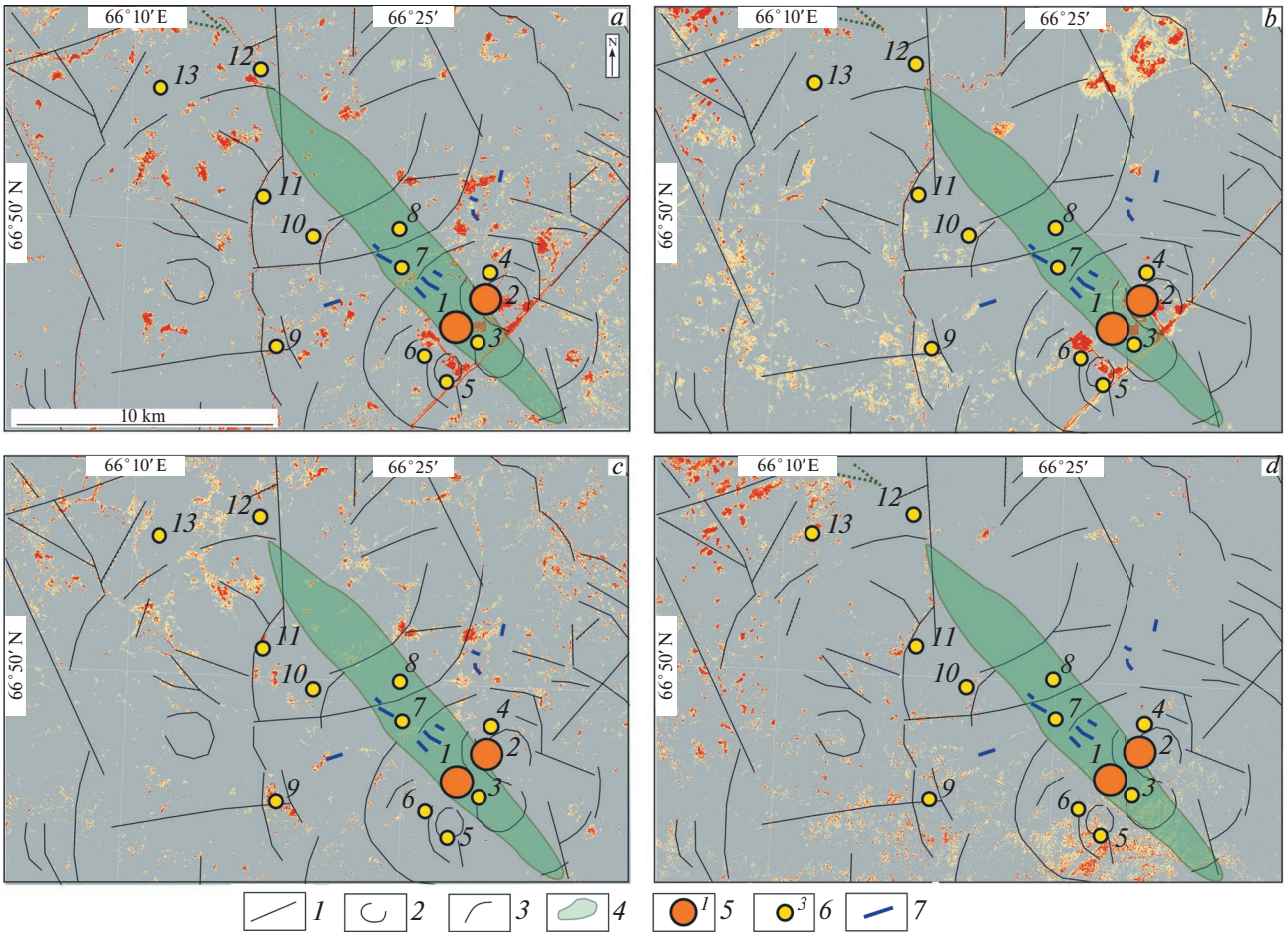

Fig. 3. Map of metasomatic changes of the Toupugol-Khanmeyshorsky ore district and adjacent territory: *a–d* — schemes of development of metasomatic change mineral associations correspond to Fig. 2; *1–3* — lineaments: *1* — radial; *2* — circular; *3* — arc; *4* — beresitization zone taken from the geological map (Zyleva et al, 2014), *5–6* — deposits and ore occurrences: Petropavlovskoye (*1*), Novogodneye-Monto (*2*), Karachentseva (*3*), Toupugol (*4*), Karyernoye (*5*), Taunugolskoye (*6*), Anomalnoye (*7*), Khanmeishorskoye (*8*), Nevidimka (*9*), Obskoye (*10*), Malokhanmeyskoye (*11*), Evyuganskoye (*12*), Evyugan (*13*), *7* — main composition dikes taken from the geological map (Zyleva et al., 2014). Concentrations of indicator groups of metasomatic changes are shown by colored dots: minimum — yellow, average — orange and maximum — red.

In addition, gold mineralization contained in skarn-magnetite deposits and ore occurrences is genetically related to gabbro and diorites.

Pb-Zn mineralization is localized at the contact of gneissed hornblende diorites and apovulcanogenic schists. A "marble-leptite horizon" with a mineral paragenesis close to skarns is distinguished; later beresites develop along the latter (Zyleva et al., 2014).

In the Toupugol-Khanmeyshorsky ore district, the area with the known gold deposits Petropavlovskoye and Novogodneye-Monto is distinguished by the highest concentrations of iron (III) oxide index (see Fig. 3)

The volcanic rocks of medium and basic composition (basalts, andesibasalts, andesites, and less frequently andesites) of the Toupugol Formation are overlain by products of often spatially combined different-age processes of skarnation, beresitization, and silicification. These metasomatic manifestations are associated with dikes of quartz montsodiorite-porphyrites and quartz gabbro of the Congorsk complex of the first and second phases of intrusion (Middle Devonian), as well as propylitization, to which plagiogranites and other granitoids of the late phase of the Sobsky complex were subjected (Middle Devonian). The development of small phenocrysts of Cu and Fe sulfides is associated with propylitization zones, along which sulfide oxidation products develop in the hypergenesis zone (Vikentyev et al., 2021).

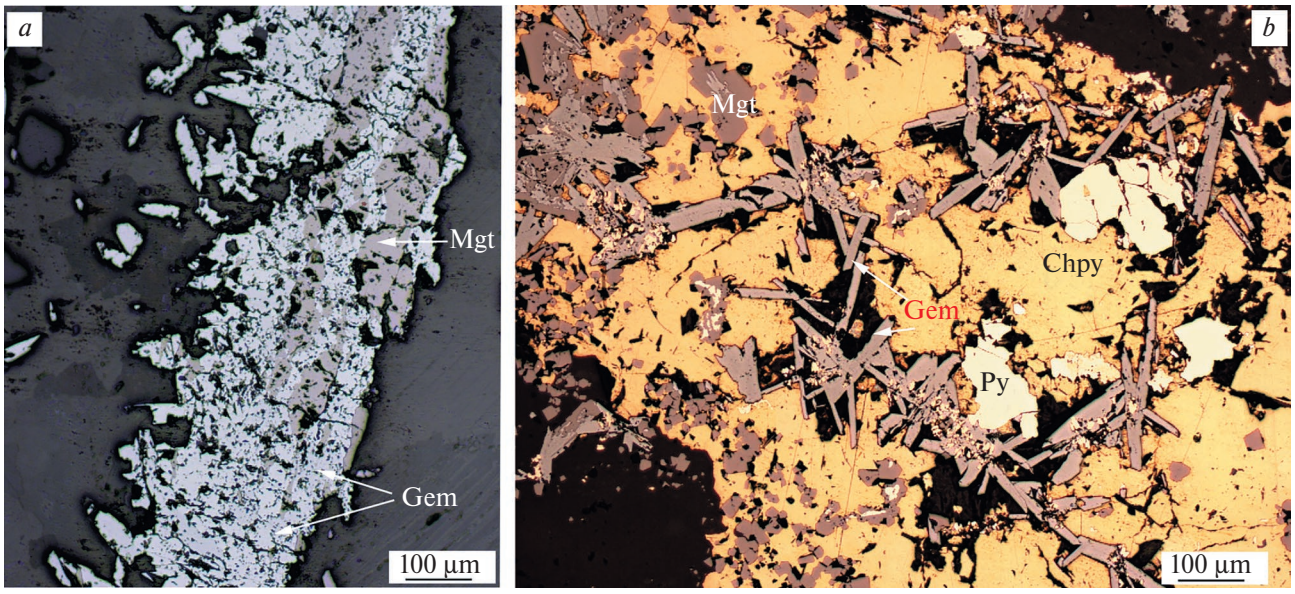

Fig. 4. Decay structures of the Novogodneye-Monto deposit (samples NM-4 and NM-27): allotriomorphic aggregates of hematite replace xenomorphic grains of magnetite in the oxidized skarn (*a*), irregular accumulations of chalcopyrite replace differently oriented needle crystals of hematite and xenomorphic grains of magnetite and pyrite localized in epidote-granate-pyroxene skarn (*b*). Notation: Mgt — magnetite, Py — pyrite, Gem — hematite, Chpy — chalcopyrite.

In addition, iron (II) oxide and iron (III) oxide in the form of concretions and various decay structures can also be found in the Novogodneye-Monto and Petropavlovskoe deposits (Fig. 4).

Researchers of the Karpinsky Institute (Zyleva et al., 2014) identified a beresitization zone with NE-dip in this area, which extends in the NW direction and was traced by boreholes in the Novogodnenskoye ore field to depths of 150–250 m with a gold content of more than 1 ppm. This zone is poorly reflected in the obtained remote sensing results due to the large thickness of Quaternary sediments, which reaches 93 m here (Zyleva et al., 2014). In the SE part of the zone, where the loose sediments, although present, are reduced in thickness to 3–6 m, coincidence is observed. Thus, we can conclude that the halos of near-ore alteration buried for more than 6 m are not reflected on the SI of the day surface.

Deposits and ore occurrences in the central part of the Malouralskaya zone are represented by the following mineralization: Cu-Zn-Mo, Mo-Cu, Fe-Ti-V-Cu and Au.

The most promising objects with iron ore mineralization in this area include contact-metasomatic (skarn), hydrothermal-sedimentary, magmatic, Ti-magnetite types. For example, skarn type occurrences of the First and Third Ore Hills are associated with contact transformation processes.

Manifestations of Ti mineralization are genetically divided into magmatic and sedimentary types. In the former, Ti is associated with iron and is part of titanomagnetite or forms an independent mineral phase — ilmenite. As a rule, rocks of the gabbro family are the most enriched with titanium, where titanium minerals sometimes form scattered phenocrysts and schlierock-like clusters (Sobsky gabbro-diorite-tonalite complex). In addition, the titanomagnetite occurrences have elevated V contents.

Mo mineralization is associated with granitoids and probably belong to the same (stockwork Cu-Mo- or V-Mo-porphyry) geological and industrial type.

Cu mineralization on the area is very widely manifested and is represented both by copper-ore and complex objects, in which Cu is associated with Pb and Zn, Ag, Au, Mo and other metals. For example, mineralization of the Mo-Cu porphyry formation is developed within the Malouralsky volcanic-plutonic belt and is represented by the Yanaslorskoye, Elkoshorskoye, Mokry Log, etc. occurrences. The first of them is localized in granitoids and has predominantly Cu-Mo specialization. The Mokry Log and Osennoe ore occurrences are associated with intrusions of quartz montsodiorites of the Kongorsky complex, which break through volcanogenic-sedimentary rocks of the Malouralskaya Formation. The exocontacts of the intrusions show epidotization, oxidization, and skarnization. The development of quartz-sericite

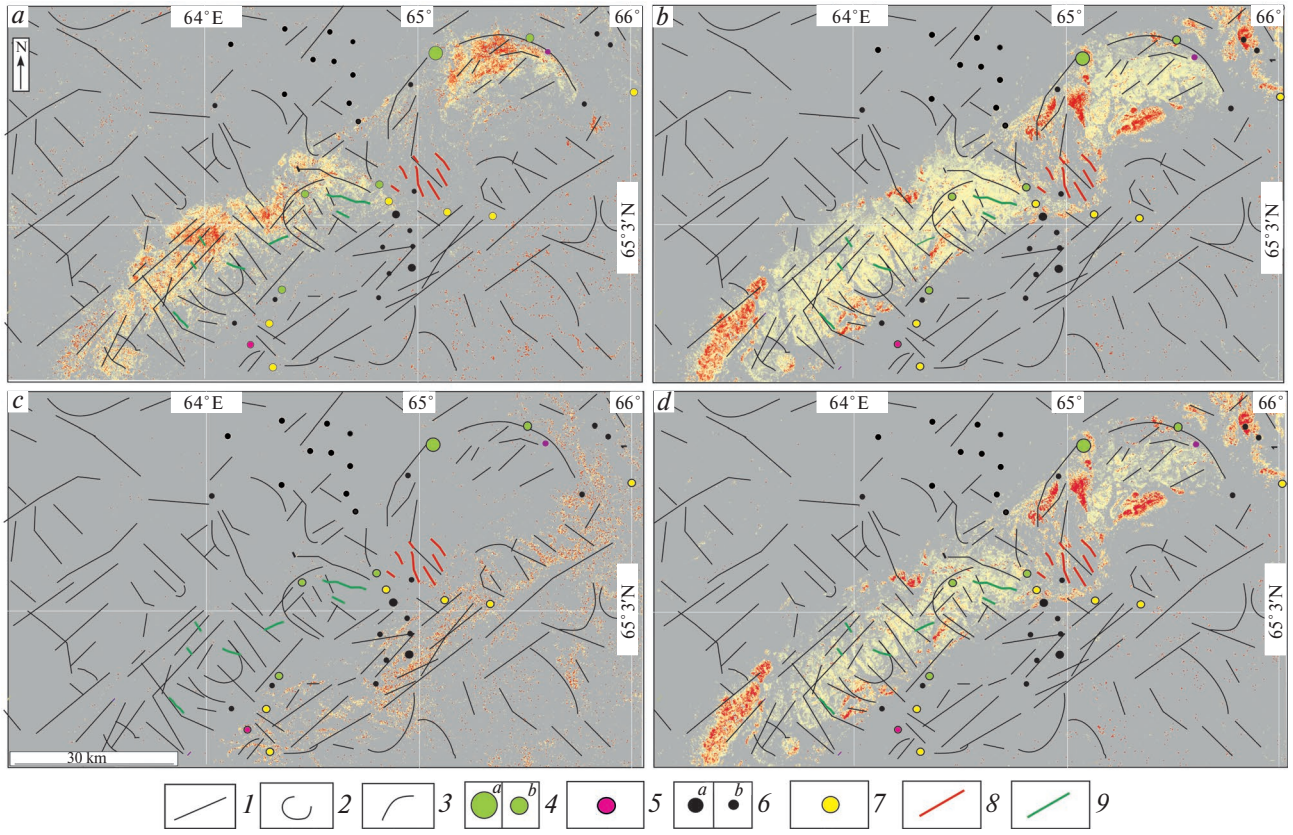

Fig. 5. Map of metasomatic changes of the central part of the Malouralskaya zone and the adjacent territory, obtained with the use of the Landsat 8 remote sensing satellite: *a–d* — correspond to fig. 2: *1–3* — correspond to fig. 3; *4–7* — deposits (*a*) and ore occurrences (*b*): *4* — Cu-Zn-Mo, *5* — Mo-Cu, *6* — Fe-Ti-V-Cu, *7* — Au, *8–9* — dikes of acidic (*8*) and main (*9*) composition taken from the geological map (Shishkin et al., 2009). Concentrations of indicator groups of metasomatic changes are shown by colored dots: minimum — yellow color, average — orange and maximum — red.

metasomatites-phyllisites (berezites) is observed in some areas of the Mokry Log ore occurrence. These formations are accompanied by intense chalcopyrite mineralization (Cu content up to 0.7%).

In addition, the Malouralskaya Formation, consisting of volcanogenic-sedimentary and sedimentary rocks, is a favorable environment for localization of skarn-magnetite and copper porphyry mineralization.

Gold ore objects are paragenetically associated with intrusions and halos of metasomatic change rocks in fault zones (Shishkin et al., 2009).

According to Landsat 8 satellite SI data, the distribution of iron (II) oxide and iron (III) oxide especially with high content, also coincides for the central part of the Malouralskaya zone, but the average concentrations of iron (III) oxide are slightly higher and distributed more evenly over the entire study area than iron (II) oxide (Fig. *5b*, *d*). The distribution of hydroxyl-(Al-OH, Mg-OH) and carbonate-bearing minerals and iron oxides and hydroxides (limonite) are different. The latter are distributed (high and medium concentrations) mainly in the part of the area (see Fig. 5).

The samples of the Amphibolitovoye ore occurrence (central part of the Malouralskaya zone) (see Fig. 1) also contain iron (II) oxide and iron (III) oxide together in the form of various decay structures (Fig. 6) (Ivanova and Tyukova, 2022).

Thus, as a result of the analysis and comparison of areas, the patterns of gold mineralization type for the eastern slope of the Polar Urals have been revealed:

— the studied areas have various ore specialization, including gold ore specialization (Au-sulphide-Fe-skarny), where Au is either the only useful component or one of the main valuable elements (Au containing ore formations: Cu-Fe-skarny, V-Fe-Cu, Cu-Mo-porphyry, etc.). At the same time, gold mineralization has a wide range of formation types: Au-sulfide-quartz veins and vein zones, quartz-Au-sulfide veins, (Cu)-Fe-ore with gold skarn, Cu-porphyry with Au, etc.;

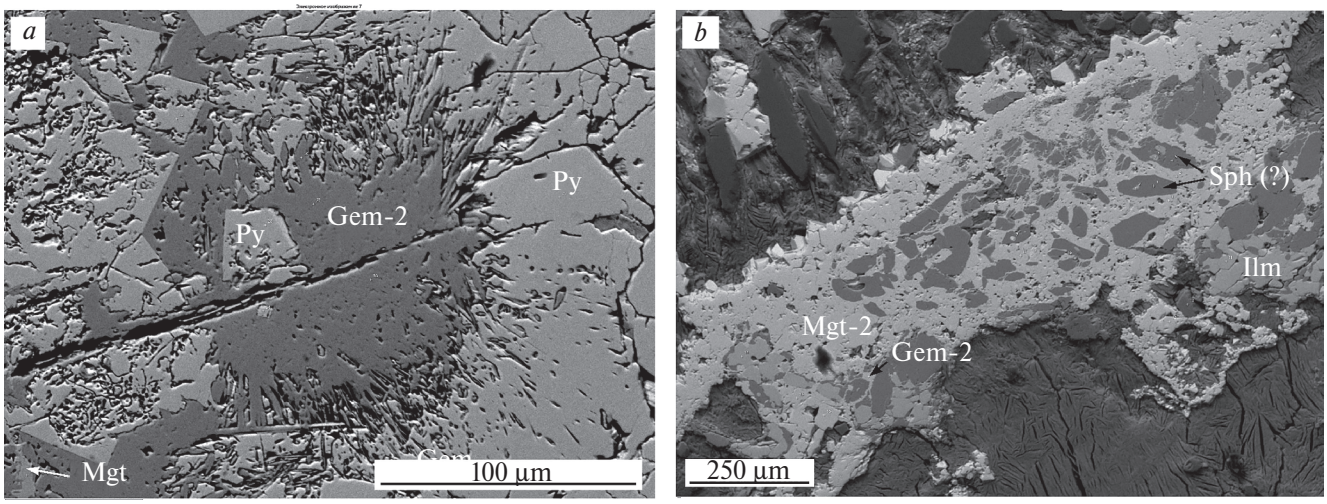

Fig. 6. Decay structures of the Amphibolitovoye ore occurrence (sample A-973): radial aggregate (fibrous structure) of hematite-2, concentrated in cataclastic pyrite localized in pyroxenite (?) (*a*), a loop structure represented by xenomorphic magnetite capturing oval inclusions of sphene (?), xenomorphic inclusions of hematite and ilmenite up to 200 μm are also localized in magnetite, but at the edges of the structure (*b*). Notation: Mgt — magnetite, Py — pyrite, Gem — hematite, Sph — sphene, Ilm — ilmenite.

— According to the conditions of formation, gold mineralization is divided into: (1) magmatic-hydrothermal type — genetically associated with intrusions, which, as a rule, were formed in the epoch close to the formation of the intrusions themselves. (2) Hydrothermal-metamorphogenic type, related to fault zones and confined to halos of metasomatites;

— iron-ore mineralization belongs (Cu-Fe-ore skarn (gold-bearing) formation) mainly to magmatic and contact-metasomatic genetic types (Shchuchinskaya zone and central part of Malouralskaya zone);

— probably, the formation of gold and complex deposits occurred as a result of the development of intracrustal metasomatic systems concentrating ore mineralization. As a result, the decay of such systems in the upper layers of the Earth's crust resulted in the formation of predominantly unextended vertically (not more than 2 km) and small in volume discontinuous columns of ore bodies (Ananyev, 2017);

— the metasomatic halo is manifested over a large area (more than 30 km^2). In areas where, due to the presence of overlying strata, either later sedimentary complexes or a shielding layer of less permeable volcanic rocks, the metasomatic halo is also manifested over a smaller area (up to 10 km^2) (Levochskaya et al., 2021; Gray and Coolbaugh, 1994);

— at microscopic study of ores of samples from deposits and ore occurrences of the studied territories iron (II) oxide and iron (III) oxide are present in the form of various accretions and decay structures.

CONCLUSION

As a result of Landsat 8 remote sensing data processing, maps of metasomatic change distribution were constructed for the territory of the Shchuchinskaya zone, the Toupugol-Khanmeyshorsky ore district and the central part of the Malouralskaya zone: hydroxyl-(Al-OH, Mg-OH) and carbonate-bearing rocks, iron (II) oxide (magnetite) and iron (III) oxide (hematite), iron oxides and hydroxides (limonite), — using spectral channels of Landsat 8 remote sensing satellite (mineralogical indices) and PCA.

Based on the results obtained in the course of the study, it can be concluded that the areas prospective for gold mineralization for the eastern slope of the Polar Urals should be localized intrusions of main composition, with which gold mineralization is genetically related, and metasomatic halos of considerable area (more than 30 km^2) with increased values of iron (III) oxide and iron (II) oxide indices, and to a lesser extent — iron oxides and hydroxides (limonite), as well as hydroxyl-(Al-OH, Mg-OH) and carbonate-bearing minerals.

FUNDING

The work was supported by the youth laboratory of IGEM RAS "Laboratory of prognostic-metallogenic studies" within the framework of the theme of the state assignment "Application of modern methods of assessment, search and forecasting of solid mineral deposits, including

strategic ones, in the Arctic zone of the Russian Federation in order to expand the mineral resource base and plan the development of transportation and communication networks".

REFERENCES

1. *Ananiev Yu.S.* Gold-concentrating systems of the Southern folded framing of the West Siberian plate (on the example of the Western Kalba). Dis. ... dok.geol.-miner. Sciences. Tomsk, 2017, p. 509 (In Russian).

2. *Andreichev V.L., Kulikova K.V., Larionov A.N., Sergeev S.A.* Age of island-arc granites in the Shchuchinskaya zone, Polar Urals: first U–Pb (SIMS) results // Doklady Earth Sciences. 2017. Vol. 477. No. 1. Pp. 1260–1264.

3. *Bohlmanna U.M., Koller V.F.* ESA and the Arctic — The European Space Agency's contributions to a sustainable Arctic // Acta Astronautica. 2020. Vol. 176. Pp. 33–39.

4. *Cheng Q., Jing, L., Panahi A.* Principal component analysis with optimum order sample correlation coefficient for image enhancement // Intern. Jour.of Rem. Sen. 2006. Vol. 27(16). Pp. 3387–3401.

5. *Chernyaev E.V., Chernyaeva E.I., Sedelnikova A.Yu.* Geology of the gold-skarn deposit Novogodnee-Monto (Polar Urals) // Skarns, their genesis and ore content (Fe, Cu, Au, W, Sn, ...). Mat. conf. XI Readings A.N. Zavaritsky. Yekaterinburg: IGiG UrO RAN, 2005. Pp. 131–137.

6. *Di Tommaso I., Rubinstein N.* Hydrothermal alteration mapping using ASTER data in the Infiernillo porphyry deposit, Argentina // Ore Geol. Rev. 2007. Vol. 32. Pp. 275–290.

7. *Dushin V.A.* Geological structure and magmatism of the Shchuchinsky megablock (Polar Urals) // News of the USGU. 2020. Issue. 4(60). Pp. 35–56. (In Russian).

8. *Ekneligoda T.C., Henkel H.* Interactive spatial analysis of lineaments // Jour. of Comp. and Geos. 2010. Vol. 36. No. 8. Pp. 1081–1090.

9. *Estrada S., Henjes-Kunst F., Burgath K.P., Roland N.W., Schäfer F., Khain E.V., Remizov D.N.* Insights into the magmatic and geotectonic history of the Voikar massif, Polar Urals // Zeitschrift der Deutschen Geologischen. Gesellschaft. 2012. Vol. 163. No. 1. Pp. 9–42.

10. *Galiullin I.Z., Perminov I.G., Konovalov Yu.I. et al.* Report on the results of works on completion of the object: "Specialized geochemical prospecting for noble and rare metals in within the West Harbeyskaya area Labytnangi", 2005.

11. *Graham G.E., Kokaly R.F., Kelley K.D. et al.* Application of imaging spectroscopy for mineral exploration in Alaska: a study over porphyry Cu deposits in the Eastern Alaska Range // Econ. Geol. 2018. Vol. 113 (2). Pp. 489–510. DOI: 10.5382/econgeo.2018.4559.

12. *Gray J.E., Coolbaugh M.F.* Geology and geochemistry of Summitville, Colorado: An Epitermal Acid Sulfate Deposit in a Volcanic Dome // Economic Geology. 1994. Vol. 89. Pp. 1906–1923.

13. *Gupta R.P.* Remote Sensing Geology, 3rd edn. Springer, Berlin, Germany, 2017. Pp. 180–190, 235–240, and 332–336.

14. *Ivanchenko G.N., Gorbunova E.M., Cheremnykh A.V.* Some possibilities of lineament analysis when mapping faults of different ranks (using the example of the Baikal region) // Earth Research from Space. 2022. No. 3. Pp. 66–83. (In Russian).

15. *Ivanova J.N., Nafigin I.O.* Application of the Landsat-8 data set and the SRTM digital elevation model to predict gold-base metal mineralization in the central part of the Little Ural zone, Polar Urals // Earth Research from Space. 2023. No. 6. Pp. 20–34. (In Russian).

16. *Ivanova J.N., Tyukova E.E.* Decay structures in the ores of the Amphibolite occurrence (the Polar Urals) // II scientific. conf. "Geology at the Continental Margin". 2022. Pp. 143–145. (In Russian).

17. *Ivanova J.N.* Prediction promising areas for gold ore mineralization based on the integration of geological, geophysical information and processing of the data set of the Earth remote sensing spacecraft Harmonized Landsat Sentinel-2 for the territory of the northern end of the eastern slope of the Polar Urals // Earth Research from Space. 2024 (in press) (In Russian).

18. *Jensen J.R.* Introductory Digital Image Processing: A remote sensing perspective // Pearson Prentice Hall, Upper Saddle River NJ 07458, 3–rd ed., 2005. Pp. 276–287 and 296–301.

19. *Jolliffe I.T.* Principal component analysis. Department of Mathematical Sciences King's College University of Aberdeen, Uk, 2–d edition., 2002. P. 487.

20. *Kenig V.V., Butakov K.V.* Ore gold deposits the Novogodnee-Monto and the Petropavlovskoye are a new gold ore region in the Polar Urals // Razvedka i okhrana nedr. 2013. No. 11. Pp. 22–24. (In Russian).

21. *Korotkov V.V.* Geochemical and other technologies, methods and techniques for forecasting and searching for deposits (mainly "hidden" type) // Federal State Budgetary Institution "VIMS", 2023. P. 166 (In Russian).

22. *Kremenetsky A.A.* Justification of search and prediction and audit works on gold within the Manukuyu-Varchatinsky ore cluster (the Polyarnaya Nadezhda, the Geokhimicheskoe, and the Blagodatnoye ore occurrence). Scale 1: 10,000. Moscow: FSUC IMGRE. 2012. P. 45 (In Russian).

23. *Kuznetsov N.B., Udoratina O.V., Andreichev V.L.* Paleozoic isotope rejuvenation of the pre-Uralide complexes and the problem of the Paleozoic evolution of the eastern margin of the East European continent, Vestn. Voronezh. Gos. Univ., Ser. Geol. 2000. No. 3(9). Pp. 15–19. (In Russian).

24. *Lesnyak D.V., Ananiev Yu.S., Gavrilov R.Yu.* Structural, geophysical and geochemical criteria for epithermal acid-sulfate gold mineralization on the example of the Svetloe ore field (Khabarovsk Territory) // Bulletin of the Tomsk Polytechnic University. Engineering of georesources. 2022. Vol. 333. No. 8. Pp. 60–72. (In Russian).

25. *Levochskaya D.V., Yakich T.Yu., Lesnyak D.V., Ananiev Yu.S.* Hydrothermal-metasomatic zoning, fluid regime and types of gold mineralization in the Emi and Elena sites of the Svetloe epithermal ore field (Khabarovsk Territory) // Proceedings of the Tomsk Polytechnic University. Engineering of georesources. 2021. Vol. 333. No. 10. Pp. 17–34. (In Russian).

26. *Loughlin W.P.* Principal Component Analysis for Alteration Mapping // Photogramm. Eng. Remote Sens. 1991. Vol. 57. Pp. 1163–1169.

27. *Masek J.G., Claverie J., Ju. M. et al.* Harmonized Landsat Sentinel-2 (HLS) Product User Guide. Product Version 2.0. 2018.

28. *Masoud A.A., Koike K.* Morphotectonics inferred from the analysis of topographic lineaments auto-detected from DEMs: application and validation for the Sinai Peninsula, Egypt // Tectonophysics. 2011. 510(3). Pp. 291–308.

29. *Mather P.M.* Computer Processing of Remotely Sensed Images: An Introduction. Chichester, UK: John Wiley and Sons. 1999. P 460.

30. *Maurer T.* How to pan-sharpen images using the gram-Schmidt pan-sharpen method—a recipe. In: International archives of the photogrammetry, remote sensing and spatial information sciences, volume XL-1/W1. ISPRS Hannover workshop, Hannover, pp. 21–2. Environmental Earth Sciences. 2013. 79:101.

31. *Milovsky G.A., Denisova E.A., Yezhov A.A., Kalenkovich N.S.* Asting mineralization in the Sob'-Kharbey area (the Polar Urals) from Geospatial data // The study of the Earth from space. 2007. No. 6. Pp. 29–36. (In Russian).

32. *Perminov I.G., Grigoriev V.V., Kozlitin V.I. al.* Prospecting and prospecting works for ore gold within the Sob-Kharbeyskaya area (YaNAO). Report on works 2006–2009 according to the State Contract No. 111–143 // Labytnangi, the Polar-Ural State Geological Enterprise, 2009. (In Russian).

33. *Pour B.A., Hashim M.* The application of ASTER remote sensing data to porphyry copper and epithermal gold deposits // Ore Geology Review. 2012. Vol. 44. Pp. 1–9. DOI: 10.1016/j.oregeorev.2011.09.009.

34. *Pour A.B., Park Y., Park T.S. et al.* Regional geology mapping using satellite-based remote sensing approach in Northern Victoria Land, Antarctica // Polar Sci. 2018. No. 16. Pp. 23–46.

35. *Pryamonosov A.P., Stepanov A.E., and et al.* State geological map of the Russian Federation. Scale 1:200,000 (second edition). The Polar Ural series. Q-41–XII Sheet. Explanatory note. Salekhard: natural resources committee for the Yamalo-Nenets autonomous district. 2001. P. 231 (In Russian).

36. *Puchkov V.N., Ivanov K.S.* Tectonics of the northern Urals and Western Siberia: general history of development // Geotecto. 2020. No. 1. Pp. 41–61. (In Russian).

37. *Remizov D.N., Shishkin M.A., Grigoriev S.I. et al.* State geological map of the Russian Federation. Scale 1:200,000 (2nd edition, digital). The Polar-Ural series. Sheet Q-41-XVI (Khordyus). Explanatory letter. Saint Petersburg: Cartographic factory VSEGEI. 2014, p. 256 (In Russian).

38. *Shishkin M.A., Astapov A.P., Kabatov N.V. et al.* State geological map of the Russian Federation. Scale 1: 1000000 (3rd gen.). The Ural series. Q41 — Vorkuta sheet: Explanatory note. St. Petersburg: VSEGEI. 2007. P. 541 (In Russian).

39. *Sobolev I.D., Soboleva A.A., Udoratina O.V. et al.* Devonian island-arc magmatism of the Voikar zone in the Polar Urals // Geotectonics. 2018. Vol. 52. No. 5. Pp. 531–563.

40. *Thannoun R.G.* Automatic Extraction and Geospatial Analysis of Lineaments and their Tectonic Significance in some areas of Northern Iraq using Remote Sensing Techniques and GIS // Intern. Jour. of enhanced Res. in Scien. Techn. & Engin. 2013. 2, 2. ISSN NO: 2319–7463.

41. *Verdiansyah O.* A Desktop Study to Determine Mineralization Using Lineament Density Analysis at Kulon Progo Mountains, Yogyakarta and Central Java Province. Indonesia // Indonesian Journ. of Geography. 2019. 51, 1. Pp. 31–41.

42. *Vermote E., Justice C., Claverie M., Franch B.* Preliminary analysis of the performance of the Landsat 8/OLI land surface reflectance product // Remote Sensing of Environment. 2016. Vol. 185. Pp. 46–56.

43. *Vermote E.F., Kotchenova S.* Atmospheric correction for the monitoring of land surfaces // Journal of Geophysical Research: Atmospheres. 2008. Vol. 113(D23).

44. *Vikentiev I.V., Mansurov R.Kh., Ivanova Yu.N. and others.* Gold-porphyry Petropavlovskoe deposit (Polar Urals): geological position, mineralogy and conditions of formation Geology of ores. deposits // Geology of ore deposits. 2017. Vol. 59. No. 6. Pp. 501–541.

45. *Vikentyev I.V., Ivanova Y.N., Tyukova E.E. et al.* Porphyry-style Petropavlovskoe gold deposit, the Polar Urals: geological position, mineralogy, and formation conditions // Geology of Ore Deposits. 2017. Vol. 59. No. 6. Pp. 482–520.

46. *Yazeva R.G., Bochkarev V.V.* Voikar volcano-plutonic belt (Polar Urals). Sverdlovsk: UC AN SSSR, 1984. P. 156 (In Russian).

47. *Zhang X., Panzer M., Duke N.* Lithologic and mineral information extraction for gold exploration using ASTER data in the south Chocolate Mountains (California) // J. Photogram. and Rem. Sens. 2007. Vol. 62. Pp. 271–282.

48. *Zylova L.I., Kazak A.P. et al.* State geological map of the Russian Federation. Scale 1:1000000 (third generation). Series West Siberian. Sheet Q-42 — Salekhard: Explanatory note. Saint Petersburg: VSEGEI, 2014. P. 396 (In Russian).

EARTH RESEARCH FROM SPACE, 2025, No. 1, pp. 47–61

USING SATELLITE INFORMATION ABOUT THE EARTH

THE USE OF SPACE SURVEY MATERIALS RESURS-P, CANOPUS-PSS, ASTER AND LANDSAT FOR FORECASTING URANIUM-MOLYBDENUM AND CHROMITE-PLATINUM MINERALIZATION IN THE POLAR URALS

© 2025 G. A. Milovsky[a], *, A. D. Aparin[a], A. R. Ibragimov[a], A. A. Kirsanov[b], and K. L. Lipiyainen[b]

[a] *Scientific Geoinformation Center of the Russian Academy of Sciences, Moscow, Russia*

[b] *All-Russian Scientific Research Geological Institute named after A.P. Karpinsky, St. Petersburg, Russia*

**e-mail: oregas@mail.ru*

Received March 05, 2024

Abstract. Methods of complex analysis of the results of space, gravimetric and magnetometric surveys for localization of ore-promising sites in the Polar Urals within the nomenclature sheets R-42, Q-42 have been developed. When decoding the materials of multi-zone satellite imagery of medium (ASTER, Landsat) and high (Canopus-PSS, Resurs-P) resolution, linear, arc and ring structural elements controlling the localization of uranium-molybdenum and chromite-platinum mineralization of the Polar Urals were revealed. The decoding of zones of metasomatically altered rocks in various spectral IR channels made it possible to localize areas for detailed work. Based on high-resolution satellite imagery, large-scale structural and tectonic schemes have been prepared and areas of detail for ground-based verification work have been outlined.

Keywords: *multi-zone satellite imagery, search signs, deposits, chromium, platinum, uranium, molybdenum, Polar Ural*

DOI: 10.31857/S02059614250105e6

INTRODUCTION

Landsat-7 (USA) and ASTER (Japan) multispectral space imagery materials were used for medium-scale interpretation. On their basis, zones of near-ore-altered rocks (berezites, secondary quartzites, sericite-hydrosludic-quartz metasomatites) were identified. The remote sensing bases of prospecting areas were prepared on the basis of multizonal space survey Resurs-P (channels 10, 21–23, 33) and panchromatic imagery Canopus-PSS with 1–3 m ground resolution.

Based on these materials, space surveying and lineament analysis of geological structures were performed. Interpretation of local volcanogenic structures, metasomatic rocks and subvolcanic formations made it possible to outline the areas recommended for ground completion on the basis of space imagery data.

Methodological techniques for predicting mineralization based on remote sensing methods include the use of space data for interpretation of structural elements (lineaments) controlling the spatial location of deposits and ore occurrences, as well as for localization of areas of hydrothermal-metasomatic rocks. Application of GIS-technologies in studying the spatial distribution of ore objects of different levels makes it possible to select new criteria for predicting mineralization. Large arrays of raw data obtained from high- and medium resolution space imagery and geological and geophysical data were processed using ArcGIS, ENVI, Adobe Photoshop software.

GEOLOGICAL STRUCTURE AND RESULTS OF SPACE SURVEY OF THE HAHAREMPE AREA (URANIUM-MOLYBDENUM MINERALIZATION)

The Hakharempe area is located in the western part of the R-42-XXXI sheet. The structure of the R-42-XXXI sheet includes structural-material complexes of 3 structural stages: Riphean-Early Cambrian, Cambrian-Upper Paleozoic and Mesozoic-Cenozoic,

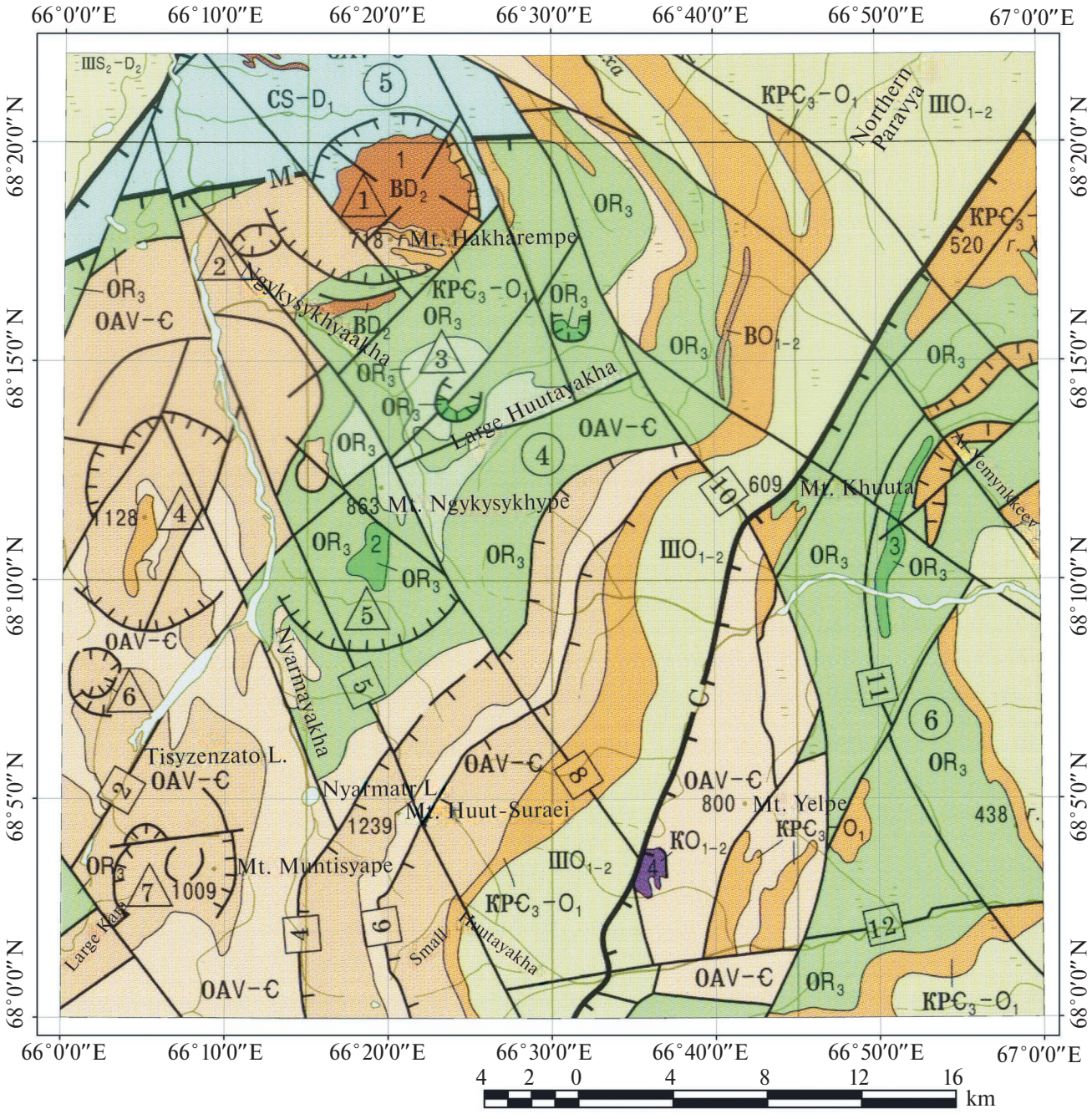

Fig. 1. Tectonic scheme at a scale of 1:500000. R-42-XXXI. The notation in Figure 1a.

corresponding respectively to the Baikal (Kadoma), Caledonian-Varissian and Alpine folding epochs (State..., 2003). They are characterized by different structural plan, separated by angular and azimuthal unconformities, often with major interruptions in sedimentation. The lower structural floor ($R–Є_1$) is composed of metamorphosed rocks of the Ochetyvis, Lyadgean, Syadatinsk, Arkanyr Formation, and is characterized by a complex combination of paleovolcanic and dispersed structural elements. The middle structural floor ($Є_3–P_1$) is composed of metamorphosed (greenshale-greenstone facies) sedimentary, volcanogenic-sedimentary riftogenic, shelf and slope complexes of the Paleozoic in combination with disjunctive and dysplicate structures. The upper structural floor (Mz–Kz) is represented by weakly lithified and friable sedimentary formations of marine and continental types complicated by intraplate

GEODYNAMIC COMPLEXES AND THEIR FORMATIONS

Geodynamic complexes / Structural levels	Intraplate			Continental margin		Subduction		Collisional
	Plate cover	Hot spots	Continental (margin-continental) rift	Shelf	Continental slope	Ophiolites	Active margin of Andean type	
	B		CR	Sh	S	O	MA	C
Paleozoic (C_3–P)		BO_{1-2} Trachireolitic BD_2 Basalt-rhyolite-andesite (volcanomictic)	KPC_3-O_1 KPC_3-O_1 Sandstone and gravel	$ШS_2$-D_2 Limestone-dolomitic $ШO_{1-2}$ Siltstone-sandstone	CS-D_1 Limestone-clayey siliceous (carbon-containing)			KO_{1-2} Ultramafic
Riphean–Early Cambrian (R_3–C_3)					Limestone-sandstone-clay (carbon-containing)	OR_3 OR_3 Basalt-andesite-dacitic	OAV-C Rhyolite-basaltoid OAV-C Siltstone-sandstone OR_3 Gabbro-diorite-granodiorite	

NOTATION

(5) Main structures and their numbers

Anticlinoria

Malokarsky

Blocks: Ochenyrdsky — 4, Lekyntalbeysky — 6

Parautochthons

Karsko-Nyarminsky — 5

(1) Paleovolcanic structures and their numbers:

1 — Khakharemskaya
2 — Malaya Caldera-Pe
3 — Vostochnokyzygeiskaya
4 — Lyadgeyskaya
5 — Kyzygeiskaya
6 — Muntysyapeyskaya
7 — Tiznezashorskaya

Disjunctive Faults

Main Structural Faults

Overlaps

Geological boundaries

Others (a – confirmed, b – suspected)

a, b Overlaps

a, b Of Uncertain Kinematics

Faults – constraints of volcano-tectonic structures

Disjunctive Faults

Main (structural faults)

M — Malotalbeysky, S — Saurieyakhinsky

[1] Secondary

2 — Tiznezatinsky
4 — Verkhnenyarminsky
5 — Nyarminsky
6 — Sangaryakhinsky
8 — Kyzygeisky
10 — Ozyorny
11 — Bedashorsky
12 — Malokhutinsky

Intrusive massifs and their numbers:

1 — Khakharemsky, 2 — Kyzygeisky,
3 — Bedashorsky, 4 — Komsomolsky

Fig. 1a. The notation.

activation processes. The main basement structures are the Ochenirdsky and Lekyntalbeysky blocks (Fig. 1). The internal structure of the Ochenyrdsky block is defined by a system of paleovolcanic structures of central and linear types (Lyadgeysky, Muntysyapeysky, Kyzygeysky, Khakharemsky paleovolcanoes) complicated by a series of paleocraters (Tiznezashorsky, Malaya Caldera-Pe, Vostochnykzygeysky, etc.) in combination with shelf-molassoid sediments of the Ochetyvisky, Lyadgeysky, and Arkanyrsky formations. The latter are often crushed into isoclinal westward-tilted folds with steep (60–70°)

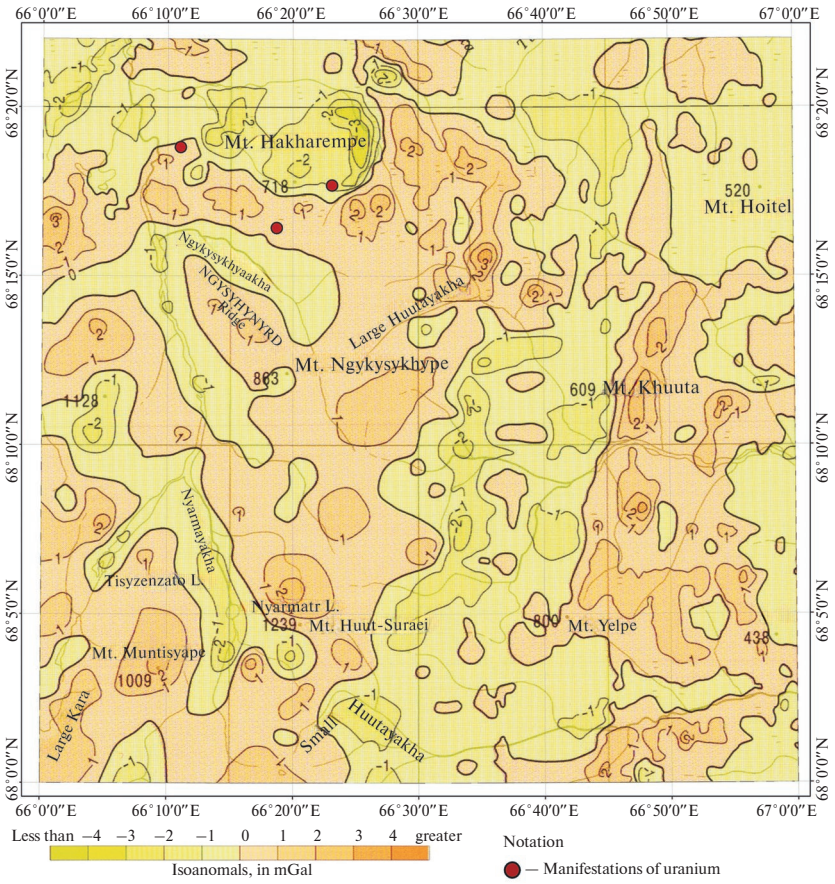
66°0′0″E
66°10′0″E
66°20′0″E
66°30′0″E
66°40′0″E
66°50′0″E
67°0′0″E
68°20′0″N
68°15′0″N
68°10′0″N
68°5′0″N
68°0′0″N
Mt. Hakharempe
718
520
Mt. Hoitel
Ngykysykhyaakha
NGYSYHYNYRD Ridge
Large Huutayakha
Mt. Ngykysykhype
863
1128
609 Mt. Khuuta
Nyarmayakha
Tisyzenzato L.
Nyarmatr L.
1239 Mt. Huut-Suraci
800 Mt. Yelpe
438
Mt. Muntisyape
1009
Large Kara
Small
Huutayakha
Less than −4 −3 −2 −1 0 1 2 3 4 greater
Isoanomals, in mGal
Notation
— Manifestations of uranium

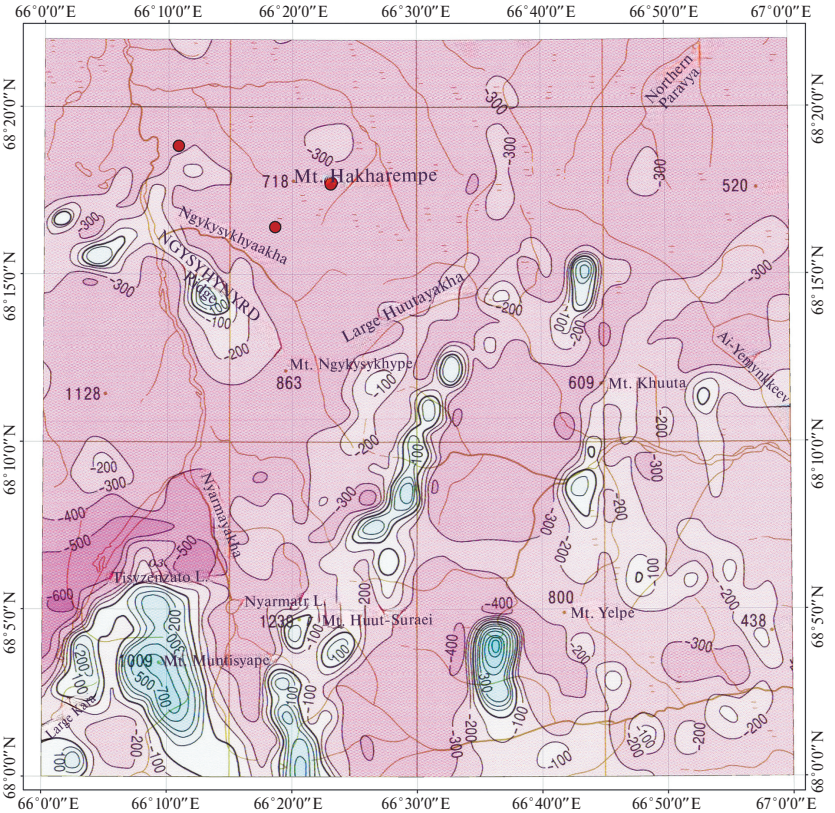
66°0′0″E
66°10′0″E
66°20′0″E
66°30′0″E
66°40′0″E
66°50′0″E
67°0′0″E
68°20′0″N
68°15′0″N
68°10′0″N
68°5′0″N
68°0′0″N
Northern Paravya
718 Mt. Hakharempe
520
Ngykysykhyaakha
NGYSYHYNYRD Ridge
Large Huutayakha
Mt. Ngykysykhype
863
1128
609 Mt. Khuuta
Ai-Yemynlkeev
Nyarmayakha
Tisyzenzato L.
Nyarmatr L.
1238 Mt. Huut-Suraci
800 Mt. Yelpe
438
1009 Mt. Muntisyape
Large Kara
Less than −600 −500 −400 −300 −200 −100 0 100 200 300 500 700 1000 1200 greater
4 2 0 4 8 12 16 km

← **Fig. 2.** Gravity and magnetic field maps at a scale of 1:500000. R-42-XXXI.

dip of the wings. Paleovolcanic structures are usually broken by a series of circular and radial disjunctives and a system of younger discordant northwestern and submeridional (Nyarminskiy and Kyzygeiskiy faults) structures. The eastern wing of the Ochenyrdsky block is complicated by a system of subparallel thrusts (Verkhnenyarminsky, Sangaryakhinsky), which are characterized by rather steep dip angles of displacements. In the east, the Ochenyrdsky block dips under the Paleozoic littoral-shelf complexes composing the Saurey syncline, complicated by the Saureyakhinskaya collision zone from the east.

The structural feature of the area is a wide development of cover-overthrust dislocations disturbed by a system of subvertical activation structures of dumping-extension type. The Kara-Nyarma paravtochthon, located to the north of the Ochenyrdsky block, is known in the literature as the "Nyarma triangle". It is composed of intensely dislocated carbonate-carbonate-carbonaceous sediments of the Kharot Formation ($S-D_1$) and is bounded on all sides by tectonic faults of the thrust-overthrust type, dipping at angles of 70–80°. The Kara–Nyarma structure and the Ochenyrdsky block are delimited by the Malotalbey structural suture. The internal structure of the suture zone is very complex: it is tectonites, blastomylonites with horizons of pseudoconglomerates. The latter are boudinage structures with mylonitization and disintegration of the strongest rocks.

The Saureyakhinsky structural suture bounds the pre-Paleozoic Lekyntalbey block from the west. Its distinctive feature is saturation of magmatites: serpentinized ultrabasites, gabbroids and dolerites. The length of the Saureyakhin suture is about 50 km. The general strike is northeastern 25–30°. The main seams of the western limitation of the Saureyakhin structure have an eastern dip (dip azimuth 110–120°) at angles of 55–60°.

Structural seams (first-order faults) are fixed in the gravimetric field by lowering Δg values (Fig. 2). The interpretation of potential fields (gravity and magnetic) and their transformations with the use of seismic survey data (GSZ) established the connection between the structure of the gravity field and, especially, its local components and the uplift of the pre-Riphean crystalline basement of the platform (State..., 2003). Positive magnetic field anomalies fix the system of the Verkhnenyarminsk and Sangaryakhinsk faults, the Tiznezashorsk paleovolcanic structure, and the Komsomolsk hyperbasite massif. Among the second-order faults, several groups can be distinguished, differing in direction and shape in plan, time of emplacement and morphology. In terms of direction, they are distinguished as: northwest, submeridional, northeast and sublatitudinal. Faults of north-western and north-eastern directions were laid down in the pre-Paleozoic time. Their distinctive feature is their length and straightness in plan, secant character in relation to the boundaries of structural-formational zones and subzones. As a rule, they are several tens of meters wide zones with complex internal structure and morphology. Sublatitudinal faults are probably also of ancient origin. The modern tectonic structure of the Polar Urals was determined by the development of Mesozoic block tectonics superimposed on Paleozoic and older geological structures.

In the Polar Urals, uranium deposits are known in the western part of the northern periclinal closure of the Lyapinsky anticlinorium and are spatially associated with the Riphean-Cambrian acidic volcanics (Mashkovtsev et al., 2010). Deposits of the molybdenum-uranium formation are characterized by spatial and paragenetic connection with complexes of late-orogenic volcanism, stockwork structure of ore bodies and genetic connection of mineralization with different facies of the metasomatic berezite formation (Boitsov et al., 2008).

The distribution of metasomatic rocks in the study area is subordinate to linear discontinuous structures of northeastern strike (Fig. 3). Metasomatic changes are most clearly manifested in the zone of the Saureyakhinsky structural suture and the Sangaryakhinsky thrust. All the studied types of metasomatites (berezites, propylites, secondary quartzites, sericite-hydrosludic-quartz metasomatites) were determined by cosmodetic survey data in the area of Lyadgeyskaya and Muntysyapeyskaya paleovolcanic structures. The halo of berezites and sericite-hydrosludic-quartz metasomatites was also noted on the southern periphery of the Khakharemskaya paleovolcanic structure. Methodological approaches for the use of ASTER multispectral space imagery to obtain information on different types of metasomatic rocks are outlined in our publications (Milovsky et al., 2023). We used measured and library spectra of reference minerals from free-access sources from NASA et al. (JPL, USGS).

The high-resolution Resurs-P space imagery was used to study the geological structures of the Khakharempe area, within which molybdenite-nasturanium mineralization was previously established. Three uranium occurrences (Valerievskoe III-1-3, Valentinovskoe III-2-1, Andriano-Pavlovskoe III-2-3) are located in the exocontact of the Hakharempe trachyryolite massif and belong to the molybdenite-nasturanic ore formation (Fig. 4). The Andriano-Pavlovskoye uranium occurrence (III-2-3) is the most studied one; it lies in the thickness of volcanogenic-sedimentary rocks of the middle composition of

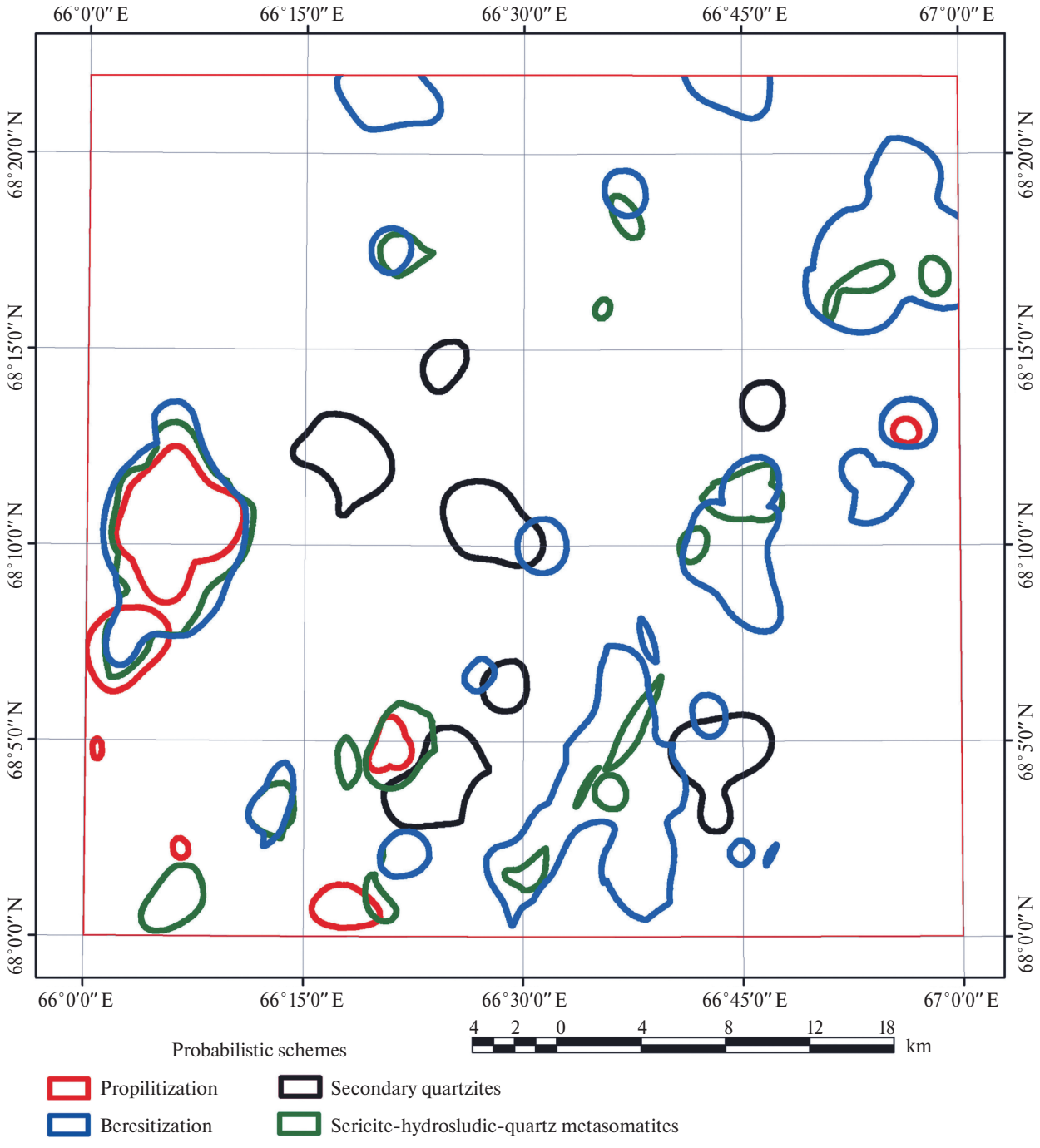

Fig. 3. Map of metasomatic rocks based on ASTER space imagery. R-42-XXXI.

the Ochetyvis Formation (R_3 оč). It is confined to the sublatitudinal body of hydrothermally altered trachyryolites of the Khakharem complex ($\tau\lambda D_3$ hh). There are six ore-bearing zones in the body of trachyryolites, controlled by tectonic disturbances of northwestern strike. The ore-bearing zones show vein-embedded ore mineralization of nasturan, pyrite, galena, sphalerite, arsenopyrite. Uranium mineralization is superimposed on polymetallic mineralization.

As a result of processing of space imagery materials (Fig. 5) of the Haharempe area, lineaments of northwestern, northeastern and sublatitudinal direction were identified; local ring structures were identified; the boundaries of lava-pyroclastic and subvolcanic formations were delineated by phototone. Northwest strike-slip faults — Nyarminskiy, Kyzygeiskiy, etc. — are predominantly developed. These faults are complicated by small

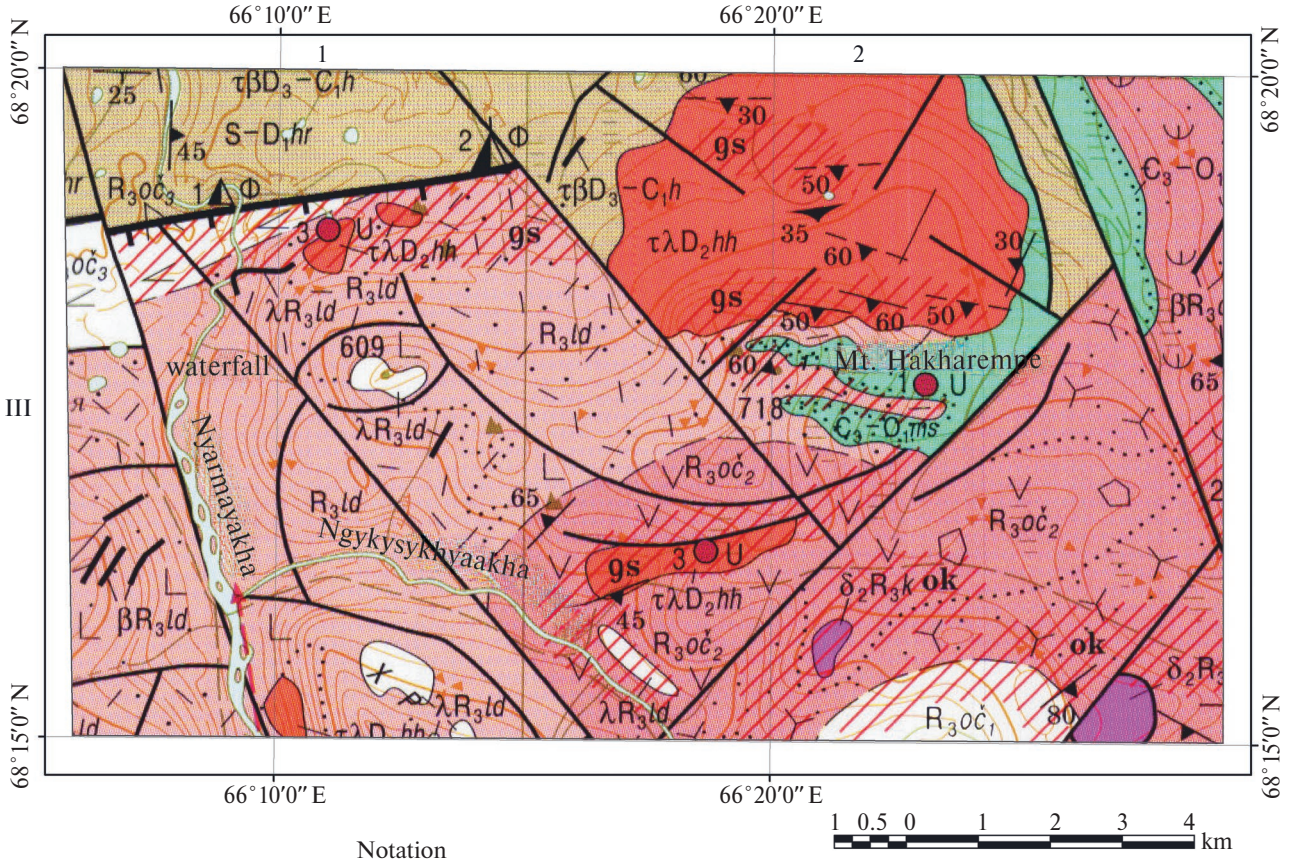

Notation

Type	Manifestations	Genetic group of deposits	Ore formations
Uranium	●U	Hydrothermal Plutogenic	Molibdenite-nasturanovaya (rare-metal uranium-molybdenum)

Uranium manifestations:
III-1-3 — Valeryevskoye
III-2-1 — Valentinovskoy
III-2-3 — Andriano-Pavlovskoe

Fig. 4. Haharempe detail area. Mineral map at a scale of 1:200000. R-42-XXXI. See Fig. 4a for notation. 4a.

shear deformations of predominantly northeastern strike. The Malotalbeyskaya suture zone is represented by several subparallel disjunctivities complicated by northwest-trending faults. The structure of the Khakharemskaya ring structure reveals arc and linear discontinuities reflecting the peculiarities of the structure of both the trachyryolite massif and the host rocks. Along the south-southeastern margin of the Hakharemskaya ring structure, the boundary between rhyolitic tuffs of the Lyadgeya Formation (R_3ld) and siltstones of the Miniseya Formation ($Є_3$–O_1ms) was delineated (by phototone). In the southern part of the detailed area, the contours of the intrusive body of diorites of the Kyzygey complex (δ_2R_3k), localized in the field of development of effusive formations (andesites) of the Ochetyviska Formation (R_3 oč$_2$), are delineated by phototone

A more detailed examination of the Khakharempe area on a scale of 1:20000 revealed additional structural elements represented by sublatitudinal and northwestern trending lineaments and arc structures. Local ring structures in the Khakharempe area are established in the field of volcanics of the Ochetyvis and Lyadgean formations. They are complicated by discontinuities and gravitate to large linear disjunctives of northeastern and northwestern strike.

The Valeryevskoye ore deposit (III-1-3) is confined to a trachyriolite stockwork of the Khakharemsky complex in the arc of intersection of northeastern and northwestern strike-slip faults. The Valentinovskoye

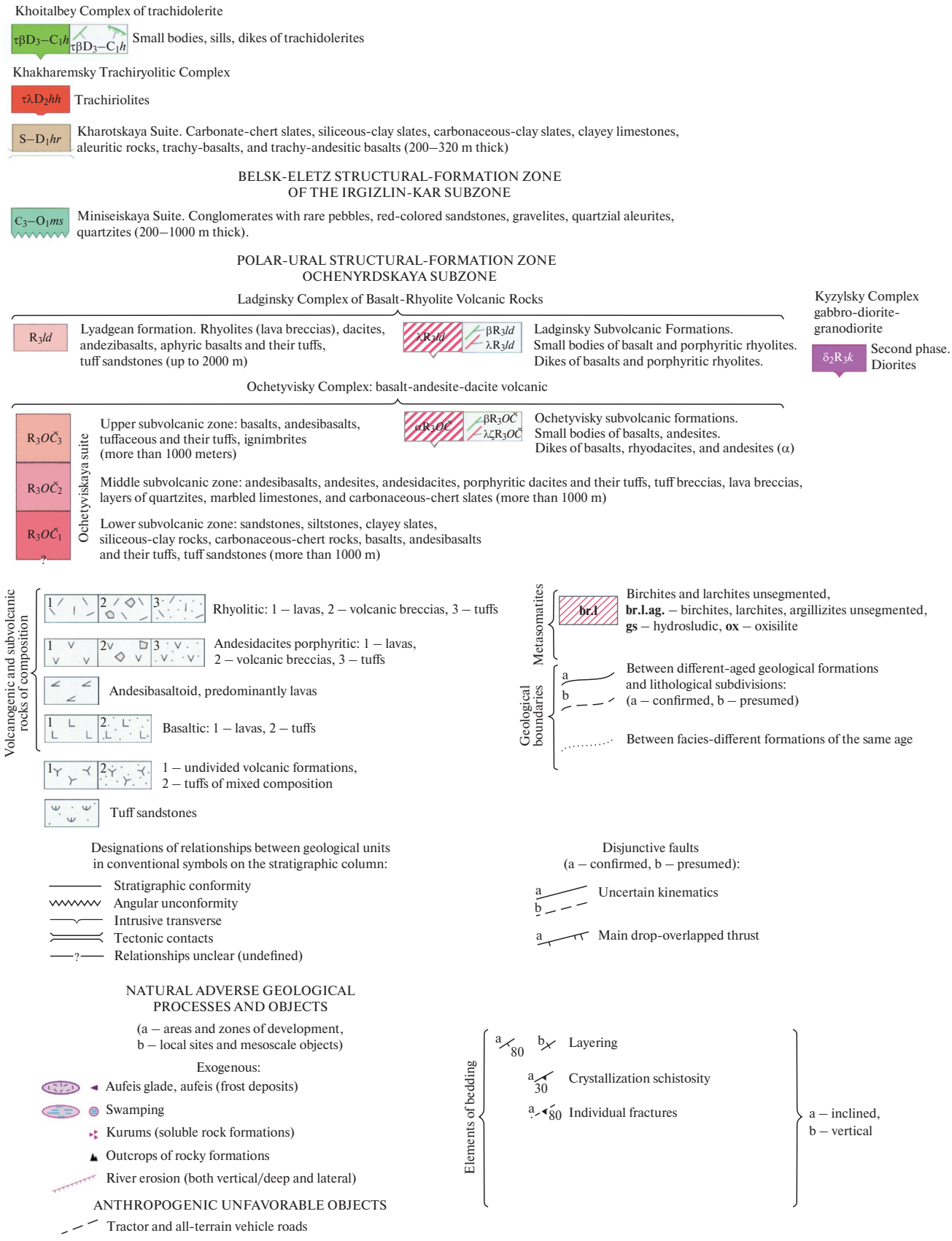

Fig. 4a. Notation to Fig. 4.

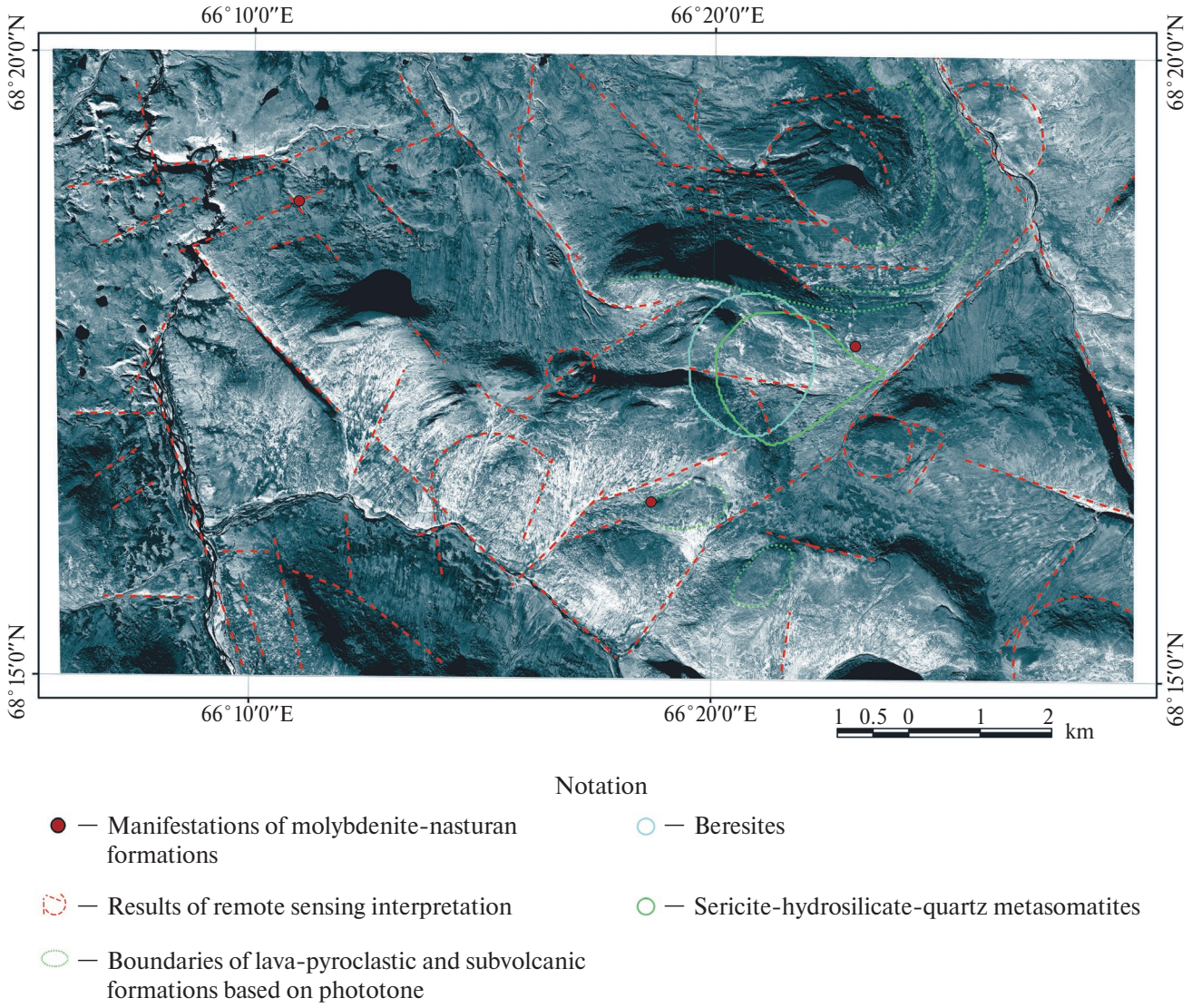

Fig. 5. Haharempe detail area. Space imagery Resurs-P route No. 9861_1. Channel 10. R-42-XXXI.

ore occurrence (III-2-1) gravitates to the northwest strike-slip fault in the area of contact between the Lyadgean and Minisean formations. In this area, the results of ASTER multispectral imaging suggest the presence of berezites and sericite-hydrosludic-quartz metasomatites. The Andriano-Pavlovskoye ore occurrence (III-2-3), as noted above, is confined to a sublatitudinal body of trachyryolites of the Khakharem complex. The contours of this body were delineated by phototone. The central part of the body is displaced by a northwestern strike-slip fault.

Thus, a comprehensive analysis of multi-area space imagery, including high-resolution Resurs-P imagery, has shown that a wide range of prospecting features can be used to predict mineralization on the scale of both ore fields and individual promising areas (deposits), including the structural factor (linear, arc, and ring structures of various grades), the lithological factor (assessment of the lithological composition of ore-bearing rocks by phototone), and the factor of hydrothermal changes (detection of metasomatites of various compositions).

GEOLOGICAL STRUCTURE AND RESULTS OF SPACE SURVEYING OF THE HADATINSKAYA AREA (CHROMITE-PLATINUM MINERALIZATION)

A detailed study of the Lower Tagil-type native platinum deposits discovered in the late 20th century

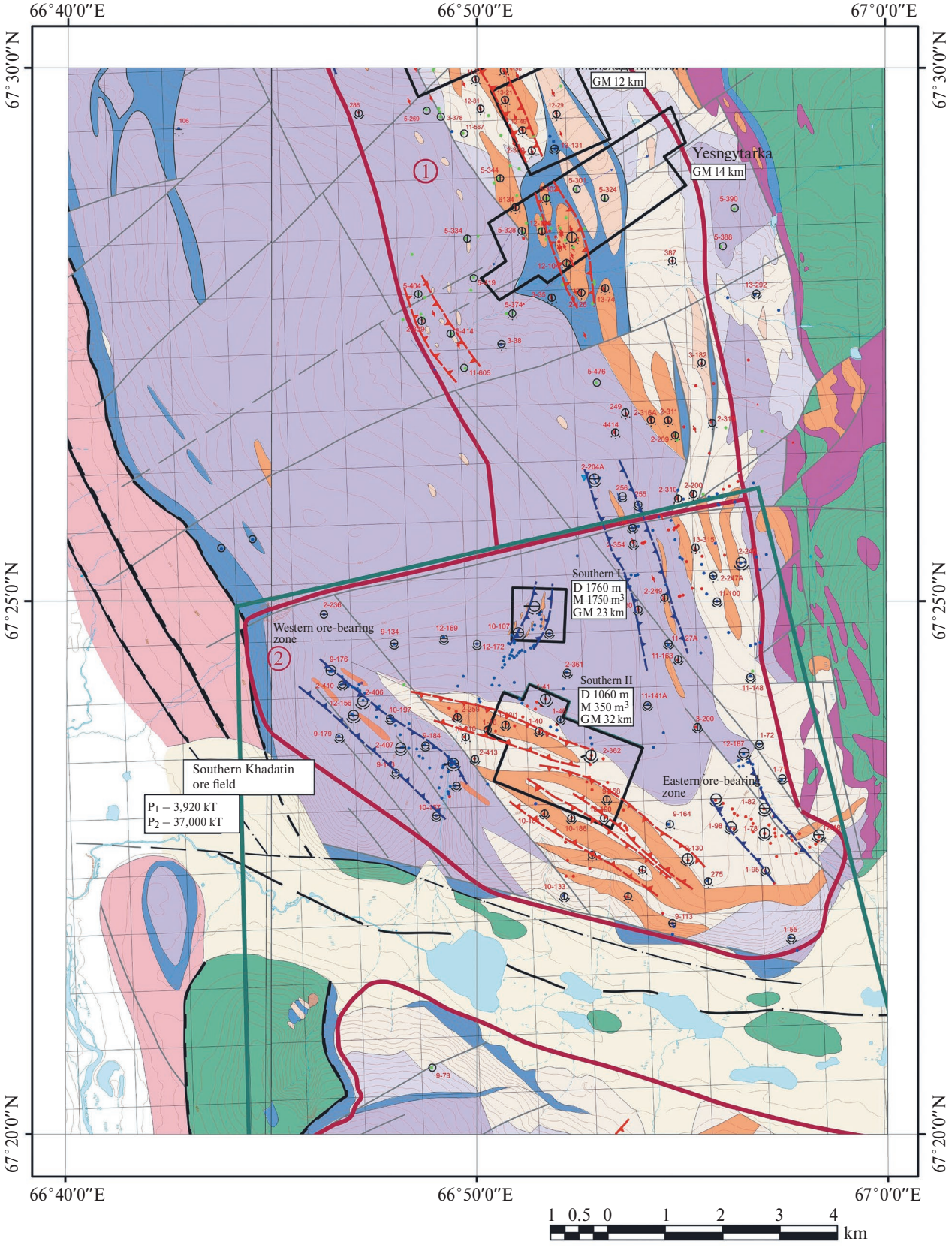

Fig. 6. Geological scheme of the southern part of the hyperbasite massif Syum-Keu with delineation of ore fields. Q-42-I. The notation in Fig. 6a.

NOTATION:

Quaternary undissected deposits (Q)

Nyarovey metamorphic complex (PR_3nr)

Kharampay-Maslovsky gabbro undissected complex ($O_3–S_1hm$)

MANTYH HYPERBASITIC COMPLEXES ($O_3–S_1$):
Dunite-verlite clinopyroxenite complex

Undissected dunites, verlites, and clinopyroxenites

Dunites with clinopyroxene

Clinopyroxenites and websterites

Dunite-Gartzburgite complex

Gartzburgites with linear and schlieric dunite segregations up to 10%

Gartzburgites with schlieric-striped dunite segregations 10–30%

Gartzburgites with schlieric-striped dunite segregations over 30%

Dunites

Serpentinite brucite-antigorite varieties

Gradation of chromite ore objects:

1–107 Manifestations (1–107)

1–95 Mineralization points (1–95)

The morphology of ore bodies is flattened-lenticular

Characteristics of chromite ores based on the density of mineralization:

Density-granular and solid

Rare to medium-granular

Sparse-granular

Mineral types of chromite ores:

High-chromium (Cr_2O_3 in chromshpinelide > 46%)

Alumina-rich (Cr_2O_3 in chromshpinelide < 46%, Al_2O_3 > 17%)

A. High-chromium type (red); B. Alumina-rich type (blue)

A B
2-109 5-97

Individual ore points (single fragments of chromite ores)

Over-scale images of jet-striped mineralization

Chromitite zones

Contours of ore fields, their numbers and names:
1. Khadatinskoye ore field
2. South Khadatinskoye ore field

Southern I Contours of detailed sections and their names

Types of geological exploration works:
D. Drilling of prospecting boreholes with a depth of up to 50–150 meters;
M. Mining works (excavation of trenches);
GM. Gravity-magnetic exploration works (observation interval of 20 (10) meters) in a profile setup

Fig. 6a. Notation to Figs. 6, 7, 8, 10.

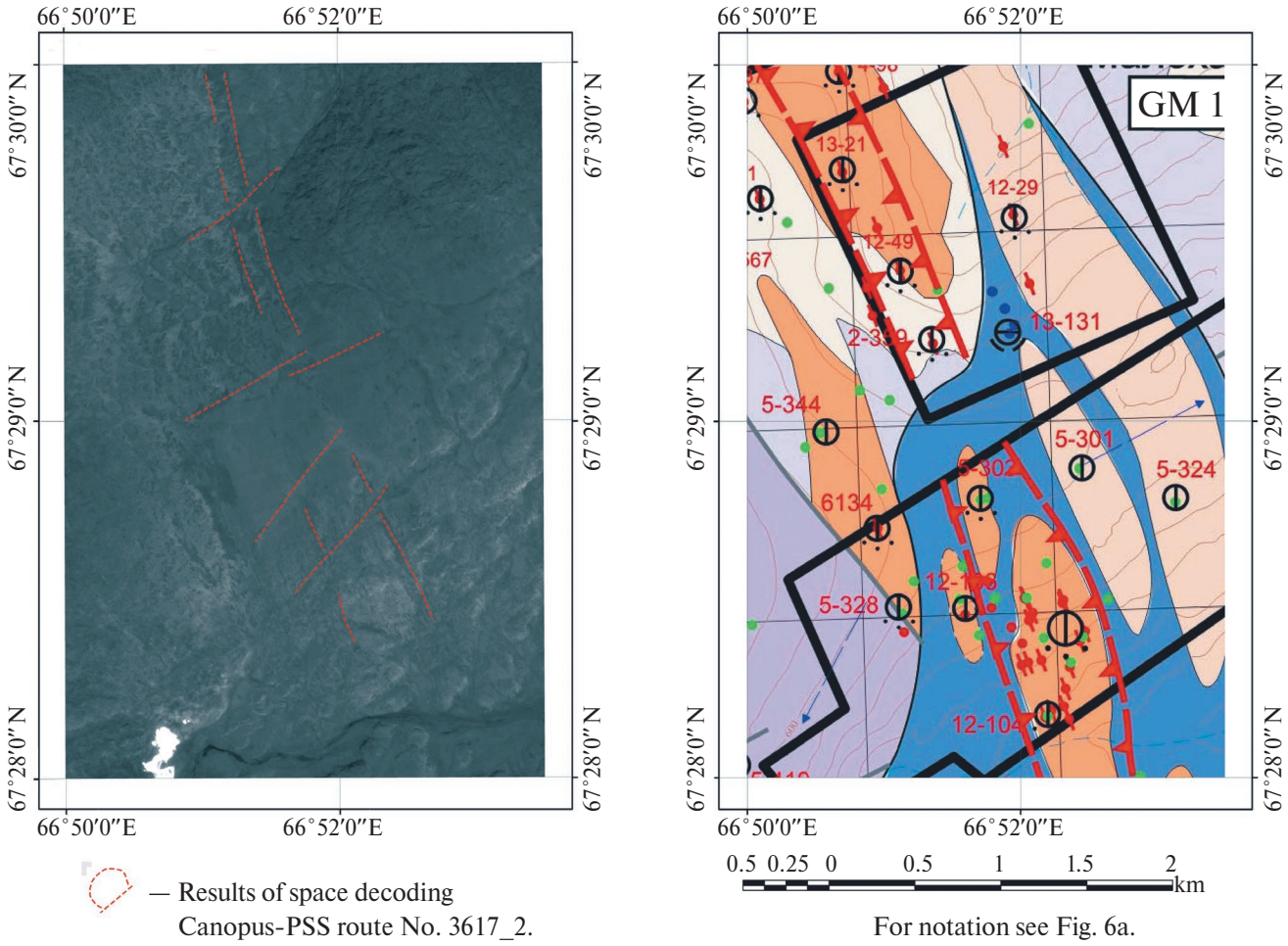

Fig. 7. Khadatinsky detailing site.

showed that the contents of the sum of platinum group metals (PGMs) are related to the iron content of dunite (Dodin et al., 2010). The amount of PGMs in ore zones is 2–10 g/t (sometimes Pt content reaches 20–50 g/t). The metallogenic potential of native platinum of the Lower Tagil type is 19000 tons. In terms of a number of parameters, the Nizhnetagilsky type is similar to the famous Bushveld type. A number of manifestations of this type are established in the Polar and Subpolar Urals, reaching the Rai-Iz and Syum-Keu massifs. The study of platinum content of the Syum-Keu ultramafic massif has revealed two types of platinometallic mineralization associated with chromite ores and sulfide occurrences (Gurskaya et al., 2003). Chromite ores are characterized by the development of three mineral associations: erlichmanite-laurite in high-magnesian chromite ores, sperrylite-irarsite-laurite in aluminous chromite ores, enriched with sulfides, and ferro-platinum in coarse-grained recrystallized dunites with poorly disseminated chromites of high-iron composition.

The Khadata area is located in the southern part of the Syum-Keu hyperbasite massif (Fig. 6). The Early Silurian Syum-Keu intrusion is represented by hyperbasites of the dunite-harzburgite formation (Geological..., 1984; State..., 2014). The Syum-Keu hyperbasite massif is confined to the arc-shaped conjugation in the zone of the Main deep fault separating the eastern wing of the Central Ural anticlinorium from the western wing of the Shchuchya synclinorium. The structure of the Syum-Keu massif includes serpentinites, pyroxenites, peridotites and dunites. Serpentinites are developed on a small scale. They compose the western near-contact part of the Syum-Keu massif. Pyroxenites are mainly recorded in the eastern peripheral part of the Syum-Keu massif, where they compose relatively small bodies (up to 1.5 × 7 km). Inhabited pyroxenites occur quite frequently among peridotites and dunites of the Syum-Keu massif in the form of dikes up to 8–10 m thick. Peridotites are the most widespread rocks of the Syum-Keu massif. Banding in the peridotites is caused by alternation of sections of different compositions. Areas in the form of bands and elongated schlieres, consisting mainly of pyroxene, alternate with the same

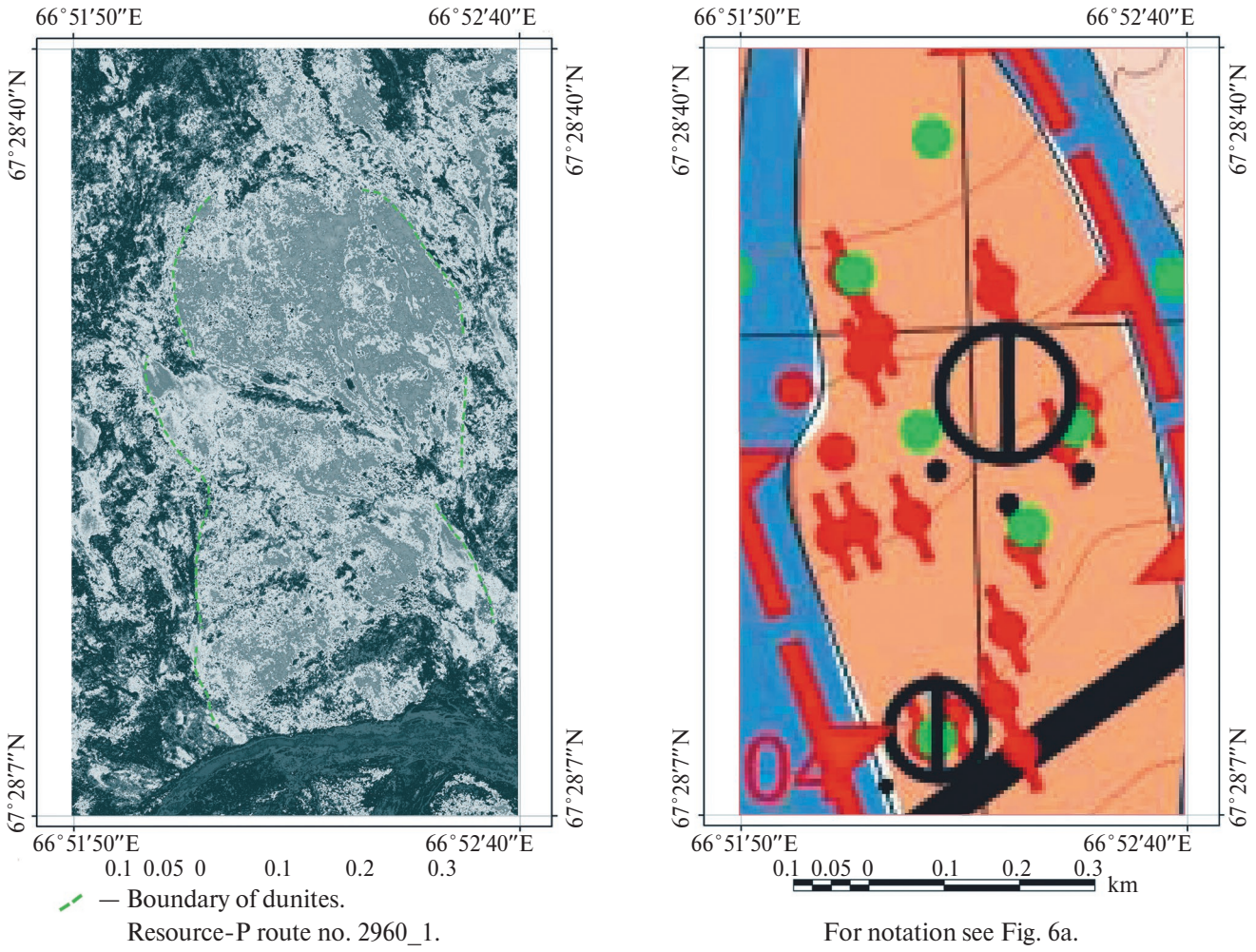

Fig. 8. Khadatinsky detailing site. Features of the structure of dunite bodies.

areas consisting of one olivine or almost one olivine. The thickness of bands and schlieres is measured in tens of centimeters or meters. Peridotites are represented almost exclusively by harzburgites and very rarely by verlites. The harzburgites consist of olivine (70–80%) and rhombic pyroxene (15–30%). Verlites occur occasionally in the eastern near-contact part of the Syum-Keu massif. The main rock-forming minerals are olivine and monoclinic pyroxene. Dunites are isolated among the harzburgites both as large elongated bodies and as thin bands and schlieres in banded harzburgites. In serpentinized varieties, a looped or reticulated structure is observed. Gabbro-norites occur in the form of small bodies intruding Syum-Keu hyperbasites and host gabbro-amphibolites.

Within the Khadatinskaya area, two areas — Khadatinsky and Yuzhno-Khadatinsky — representing chromite-bearing zones localized in structures of different spatial orientation have been selected for studies of multizone and high-resolution space imagery (SI) capabilities. The Khadatinsky section includes a discontinuous linear chromite-bearing zone with jet-banded mineralization. Interpretation of the Canopus SI confirmed the discontinuous nature of the ore-bearing zone, which may be due to displacements along northeastern strike-slip faults (Fig. 7). The chromite occurrences are confined to dunites; therefore, it is of interest to determine the boundaries of dunite bodies within the hyperbasite field using high-resolution SI materials. Figure 8 shows the results of delineation of dunite boundaries in the Khadati area using the Resurs SI phototone. Another procedure of the Resurs SI processing was aimed at clarifying the boundaries of the jet-band structure of mineralization within the dunite bodies. The capabilities of the high-resolution multizonal CW resource for predicting chromite mineralization are shown in Figure 9. Two chromite-bearing zones have been identified in the South Khadata area based on geological data. The Resurs SI analysis allows us to identify only one zone of northwest strike in this

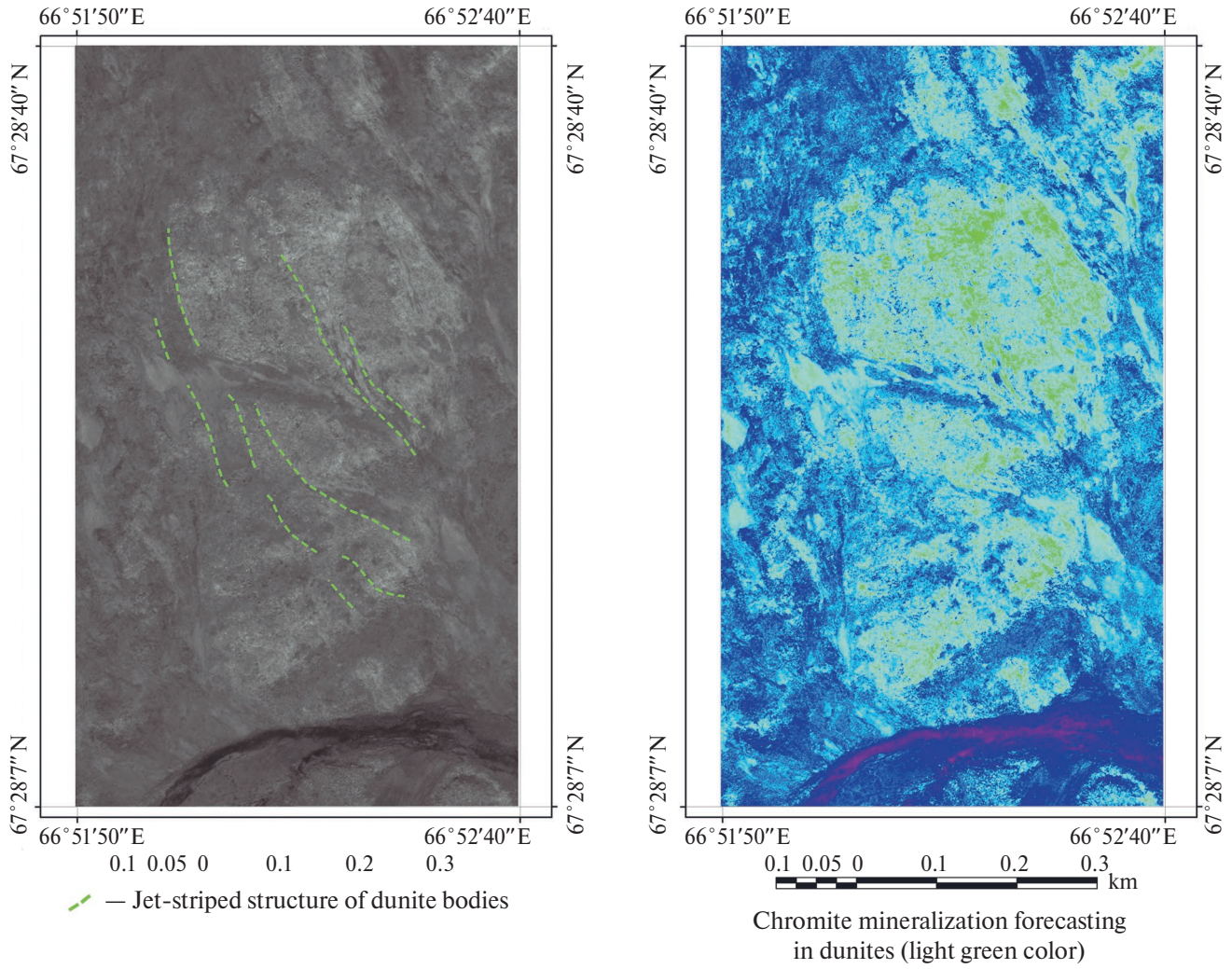

Fig. 9. Khadatinsky detailing section. Resource-P route No. 2960_1.

area, divided into three fragments by northeast-oriented disjunctives (Fig. 10).

CONCLUSION

On the basis of computer processing of infrared satellite imagery of the Hakharempe area, disjunctives controlling the location of molybdenite-nasturanic mineralization and areas of development of hydrothermally altered rocks (berezites, sericite-hydrosludic-quartz metasomatites) have been identified. The predominant development is dominated by northwestern strike-slip faults, which are complicated by shallow shear deformations of predominantly northeastern strike. Analysis of multizone space imagery, including high-resolution Resurs-P imagery, has shown that a wide range of prospecting attributes can be used to predict molybdenite-nasturanic mineralization on a scale for both ore fields and individual prospective areas (deposits), including structural factor (linear, arc, ring structures of various grades), lithological factor (delineation of lava-pyroclastic and subvolcanic formations boundaries by phototone) and hydrothermal alteration factor (detection of metasomatites of various compositions preceding and accompanying ore deposition process).

The use of high-resolution space imagery within the Khadata area of the Syum-Keu massif allowed us to determine the structural position of chromite-bearing zones and clarify the boundaries of ore-bearing dunites by phototone. As a result of interpretation of the space imagery of Canopus-PSS and Resurs-P, the discontinuous nature of the ore-bearing zone was established, which is caused by displacements along northeastern strike-slip faults, and the contours of dunite bodies within the hyperbasite field were determined. The processing of the Resurs-P space imagery allowed us to clarify the boundaries of the jet-strip structure of mineralization within the dunite bodies.

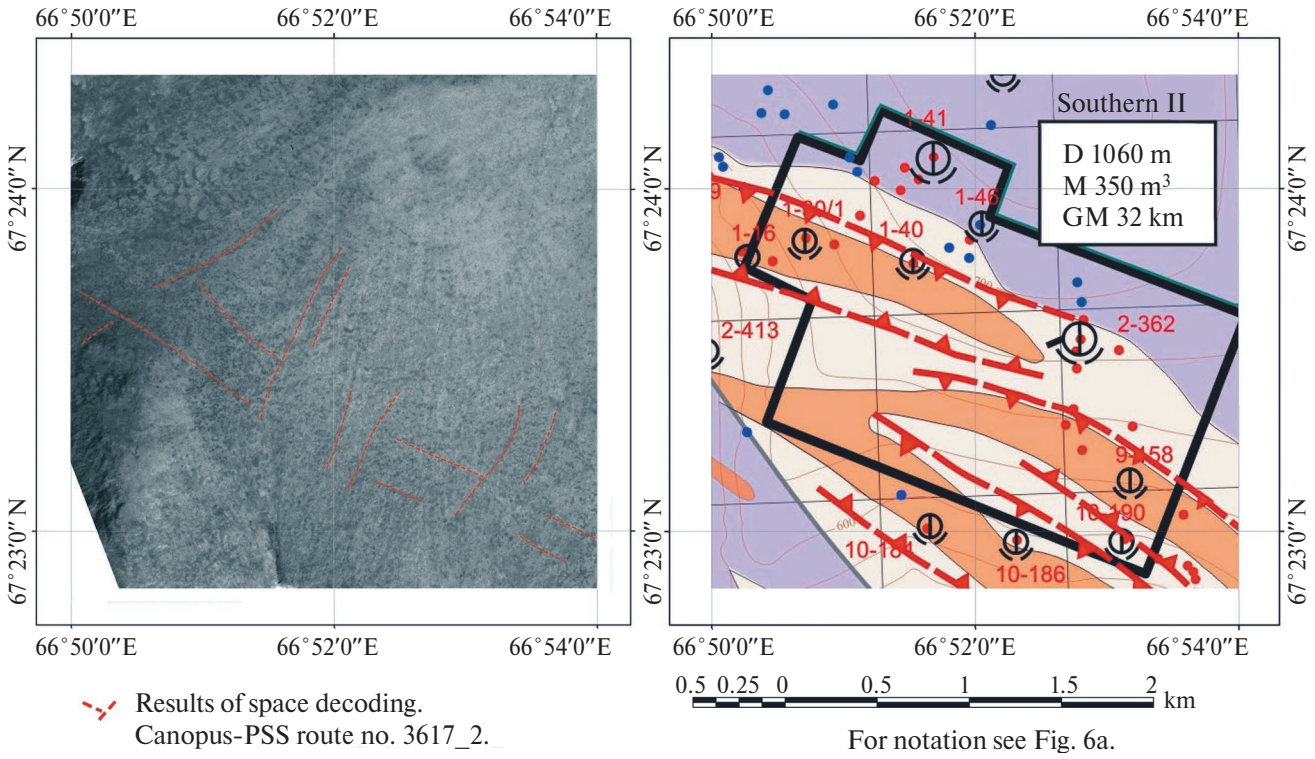

Fig. 10. Yuzhno-Khadatinsky detailing site.

FUNDING

The work was done under State Assignment No. 122040300015-6.

REFERENCES

1. *Boytsov V.E., Vercheba A.A.* Geologo-promyshlennye tipy mestorozhdenij urana: M.: KDU, 2008. 310 p.

2. Geologicheskaya karta SSSR. Masshtab 1:200000. Seriya Severo-Ural'skaya. List Q-42-I. Ob"yasnitel'naya zapiska. M.: VSEGEI, 1984. (Ministerstvo geologii SSSR, Glavnoe Tyumenskoe PGO).

3. Gosudarstvennaya geologicheskaya karta Rossijskoj Federacii. Masshtab 1:200000. Vtoroe izdanie. Seriya Polyarno-Ural'skaya. List R-42-XXXI, XXXII. Ob"yasnitel'naya zapiska. SPb., VSEGEI, 2003. (MPR Rossii po Yamalo-Neneckomu AO).

4. Gosudarstvennaya geologicheskaya karta Rossijskoj Federacii. Masshtab 1 : 1000000 (tret'e pokolenie). Seriya Zapadno-Sibirskaya. List Q-42 Salekhard: Ob"yasnitel'naya zapiska. SPb.: VSEGEI, 2014. 396 p.

5. *Gurskaya L.I., Smelova L.V.* Platinometal'noe mineraloobrazovanie i stroenie massiva Syum-Keu (Polyarnyj Ural) // Geologiya rudnyh mestorozhdenij. 2003. 45. 4. Pp. 353–371.

6. *Dodin D.A., Dodina T.S., Zoloev K.K., Koroteev V.A., Chernyshov N.M.* Platina Rossii: sostoyanie i perspektivy // Litosfera. 2010. No. 1. Pp. 3–36.

7. *Mashkovtsev G.A., Konstantinov A.K., Michuta A.K., Shumilin M.V., Shchetochkin V.N.* Uran rossijskih nedr. M.: VIMS, 2010, 850 p.

8. *Milovsky G.A., Kirsanov A.A., Lipiyainen K.L., Aparin A.D.* Prognozirovanie zoloto-serebryanogo orudeneniya v predelah Pepenveemskoj rudnoj zony CHukotskogo poluostrova na osnove kosmicheskoj s"emki Resurs, Kanopus i ASTER // Issled. Zemli iz kosmosa. 2023. No. 4. Pp. 26–41.

9. *JPL* (https://speclib.jpl.nasa.gov/library).

10. *USGS* (https://crustal.usgs.gov/speclab/QueryAll07a.php).

EARTH RESEARCH FROM SPACE, 2025, No. 1, pp. 62–73

USING SATELLITE INFORMATION ABOUT THE EARTH

STRUCTURE OF WATER DURING THE FEEDING MIGRATION PERIOD OF THE PACIFIC SQUID IN THE SEA OF JAPAN ACCORDING TO SATELLITE DATA

©2025 A. A. Nikitin*, I. L. Tsypyshcheva, and N. M. Mokrin

Pacific Branch of VNIRO (TINRO), Vladivostok, Russia

**e-mail: aleksandr.nikitin@tinro.vniro.ru*

Received August 01, 2024

Abstract. According to the sea surface temperature archive for the years 2018–2023, reconstructed from data obtained by the AQUA and TERRA satellites (MODIS spectroradiometer) with a spatial resolution of 1 km, analyzed and processed at the Shared Use Center of the Regional Satellite Environmental Monitoring of the Far East Branch of the Russian Academy of Sciences, the thermal and dynamic conditions of the waters in the northwestern part of the Sea of Japan were examined, along with the areas for jigging Pacific squid in the Sea of Japan. The analysis of satellite data allowed for the identification of elements of thermal structure within the spatial distribution field of sea surface temperature, where successful catches of Pacific squid were made. Primarily, the formation of squid fishing areas depended on the development or weakening of the branches of the Tsushima and Primorsky currents, as well as the presence of mesoscale eddy structures in their waters. Squid aggregations were mostly associated with areas of eddy upwelling. Maximum catches were concentrated on the periphery of subtropical anticyclonic eddies bordering subarctic waters. If the eddy had a spiral structure, aggregations were primarily focused in the center of the eddy. If the inflow of subtropical waters took the form of a mushroom-shaped current, large catches were mainly observed in the current's jet and in the zones of anticyclonic and cyclonic eddies of the dipole. In the frontal zone of subtropical and subarctic waters, squid fishing areas were located on the warm side of the Subarctic (Polar) front.

Keywords: *Sea of Japan, Pacific squid (Todarodes pacificus), satellite information, temperature, eddies, advection, jet currents, mushroom currents*

DOI: 10.31857/S02059614250106e9

INTRODUCTION

The Pacific squid (Todarodes pacificus) is one of the mass species of the epipelagial Northwest Pacific Ocean, which is of important commercial importance in the APR countries. In years of high abundance, the biomass of the species in the Russian exclusive economic zone (EEZ) of the Sea of Japan amounted to 79–97% of the total recorded stock of nekton (Shuntov, 2016). This species is characterized by a short life cycle (about 1 year), the presence of long migrations (Fig. 1), covering the East China Sea, the Sea of Japan, the Sea of Okhotsk and the Pacific waters of Japan and the Kuril Islands, as well as significant fluctuations in abundance (Mokrin and Hen, 2004; Gong at al., 2007; Kidokoro at al., 2010; Sakurai at al., 2013). As squid abundance decreased, the geography of fishing areas also changed.

Previously, the main characteristics of the environment for the formation of squid aggregations were studied only by means of contact oceanological measurements (Mokrin and Slobodskoy, 1998; Dyakov, 2003; Savinykh et al., 2003; Mokrin at al., 2002; Novikov et al., 2007). With the appearance of new algorithms for processing satellite signals, it became possible to provide not only qualitative but also quantitative assessment of water temperature in the seas on the basis of satellite measurements (Aleksanin and Aleksanina, 2006). Satellite images of the sea surface and the results of their processing are used as information sources characterizing the hydrological features of the habitat of hydrobionts, primarily water temperature. The important ecological significance of water temperature is explained by its significant influence on all biological processes in the sea, from the production of primary organic matter to the behavior of commercial accumulations of hydrobionts. Maps of the Sea of Japan surface temperature (SST), based on satellite monitoring data, make it possible, first of all, to assess the state and dynamics of temperature conditions in the fishing area, to evaluate the spatial and temporal variability of ocean circulation manifestations: currents, frontal zones, meanders and eddies of various

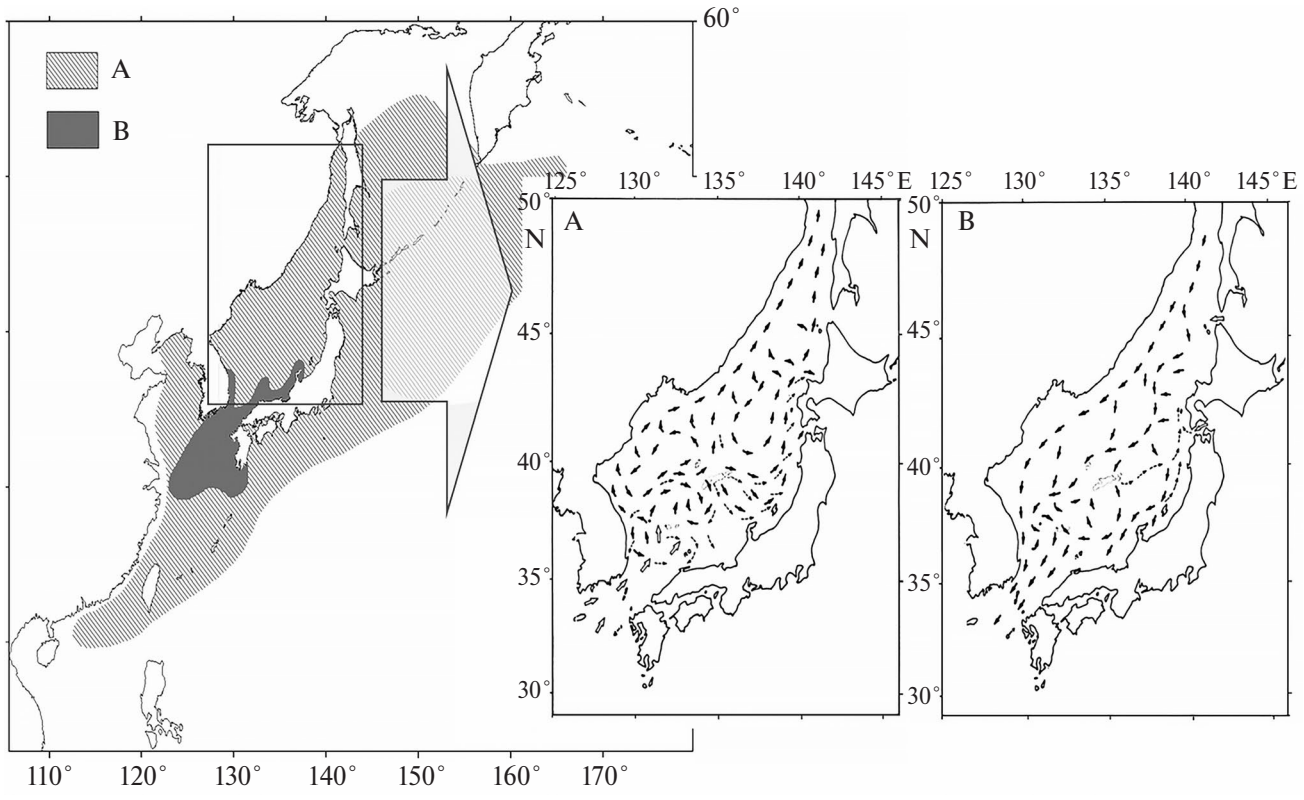

Fig. 1. Distribution of the Pacific squid in the Northwest Pacific Ocean: *a* – areal base, *b* — breeding area, migration routes of the Pacific squid in the Sea of Japan in spring-summer (*c*) and fall (*d*) periods (according to Kasahara, 1978).

scales (Ginzburg et al., 1998; Nikitin, 2006; Nikitin, Yurasov, 2008). Eddy upwelling, which occurs at the eddy boundary, has been considered as a mechanism for creating favorable conditions for the formation of commercial aggregations of saury (Belonenko and Kozub, 2018), but this mechanism can also be considered for commercial aggregations of Pacific squid.

The position of warm eddies determines the migration paths not only of pelagic fish species, but also affects the distribution of squid. The eddy formation can indicate the beginning of migration and determine the timing of its end (Nikitin et al., 2004; Bulatov et al., 2008; Samko, Bulatov, 2014). The purpose of this work was to identify from satellite information the elements of water structure, in which the largest catches of TCs were observed, to improve short-term forecasting of areas of fishing aggregations during the poutine season.

MATERIALS AND METHODS

To achieve this goal, we compared the areas of longline (jigging) fishing for TC in the Primorye subzone of the Sea of Japan (according to the vessel daily data of the CSMS system of Rosrybolovstvo, vessel daily catches are given in tons) and elements of the hydrological situation in the Sea of Japan, obtained as a result of interpretation of infrared satellite images during the 2018–2023 fishing season. The archive of sea surface temperature (SST) reconstructed from MODIS spectroradiometer data (AQUA, TERRA satellites) in the infrared spectral range with a spatial resolution of 1 km was used. The data were obtained and processed at the Collective Use Center of Regional Satellite Environmental Monitoring of the Far Eastern Branch of the Russian Academy of Sciences (RAS). Additionally, monitoring and research in the Sea of Japan was carried out by analyzing daily satellite data of TPM and its anomalies. The data were obtained at Copernicus Marine Service (URL: http://marine.copernicus.eu). The anomalies were calculated based on the norm for 1981–2010.

To analyze the temperature regime of the waters in the northwestern part of the Sea of Japan, meridional sections were selected at 132°E (S. 1), 135°E (S. 2), 138°E (S. 3), and 141°E (S. 4), as well as zonal sections at 42°N (S. 5) and 47°N (S. 6) (Fig. *2a*, *b*). The principle of selecting transects was related to the position of intensive warm flows, which coincide with the passage of feeding migration flows of pelagic fish species and squid, as well as associated with fishing areas. Characteristics of the temperature regime

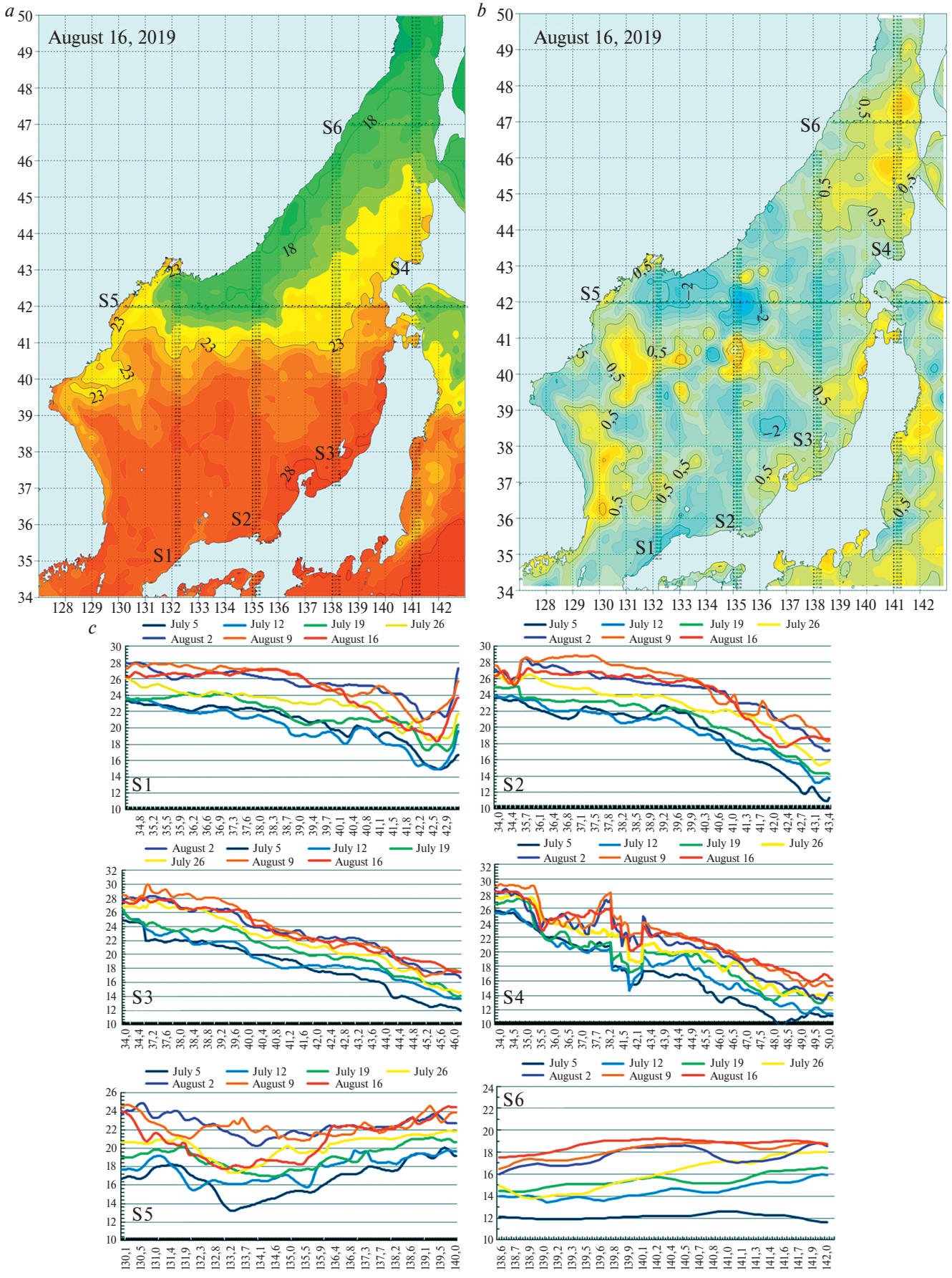
a
August 16, 2019
S1
S2
S3
S4
S5
S6
b
August 16, 2019
c
July 5
July 12
July 19
July 26
August 2
August 9
August 16

← **Fig. 2.** Spatial distribution of water surface temperature (*a*) and its anomaly (*b*) on 16.08.2019 (URL: http://marine.copernicus.eu/services-portfolio/access-to-products/) and July-August water temperature distribution (*c*) on meridional transects at 132°E (S. 1), 135°E (S. 2), 138°E (S. 3), 141°E (S. 4) and on zonal transects at 42°N (S. 5) and 47°N (S. 6).

of the fishing areas in the northwestern part of the Sea of Japan were analyzed based on the graphs of water temperature changes at the indicated transects in each decade (Fig. *2c*).

Having identified the position of intensive warm flows (Fig. *3a*), which may coincide with the passage of migratory flows of pelagic fish and squid species, we further identified hydrological elements of water structure in the temperature field, in the areas where commercial fishing for TC was conducted (Fig. *3b*). Glance 1.95 software was used to visualize the spatial distribution of TPO from satellite information. During visual-manual interpretation, by correcting the brightness thresholds of the images using the histogram, we achieved color manifestation of water masses. Anomalies of the sea surface state such as mesoscale eddies and jet mushroom-shaped currents with a eddy dipole at the end, thermal inhomogeneities of upwelling phenomena were observed. For example, Figure *4a* shows a clearer structure of the spiral anticyclonic eddy (swirling eddy) in the satellite image when the lower temperature barrier of 16 °C is established. A map-scheme was constructed from this image (Fig. *4b*).

However, eddy structures were not always clearly distinguished in the water temperature field

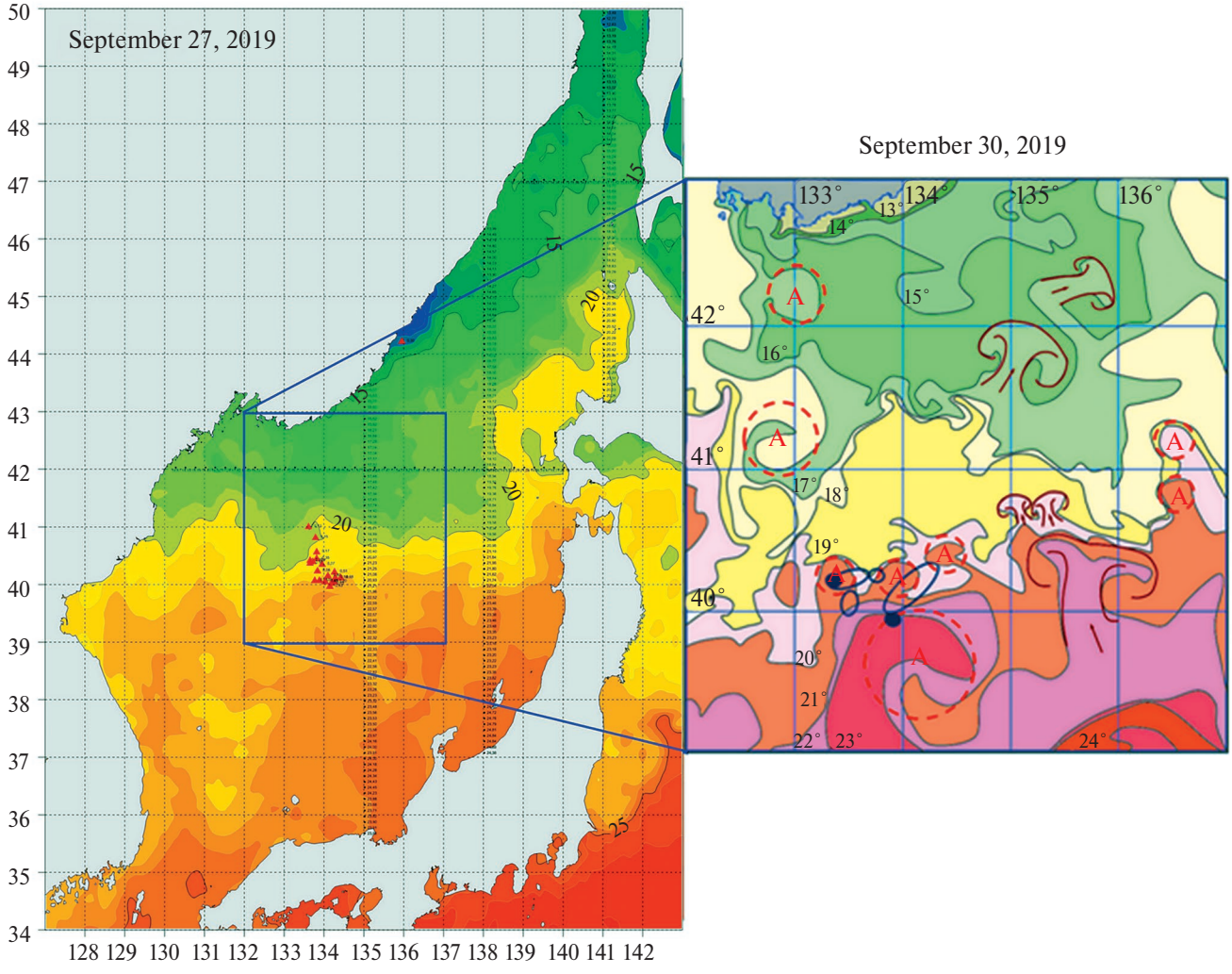

Fig. 3. Spatial distribution of sea surface temperature and fishing grounds of Pacific squid (left) (URL: http://marine.copernicus.eu/services-portfolio/access-to-products) and map-scheme of the thermal structure of waters constructed from satellite observations with squid fishing grounds in the Sea of Japan (right). Symbols: A – anticyclonic eddy; ○ — areas of TC catches; ● — places of maximum catches (t).

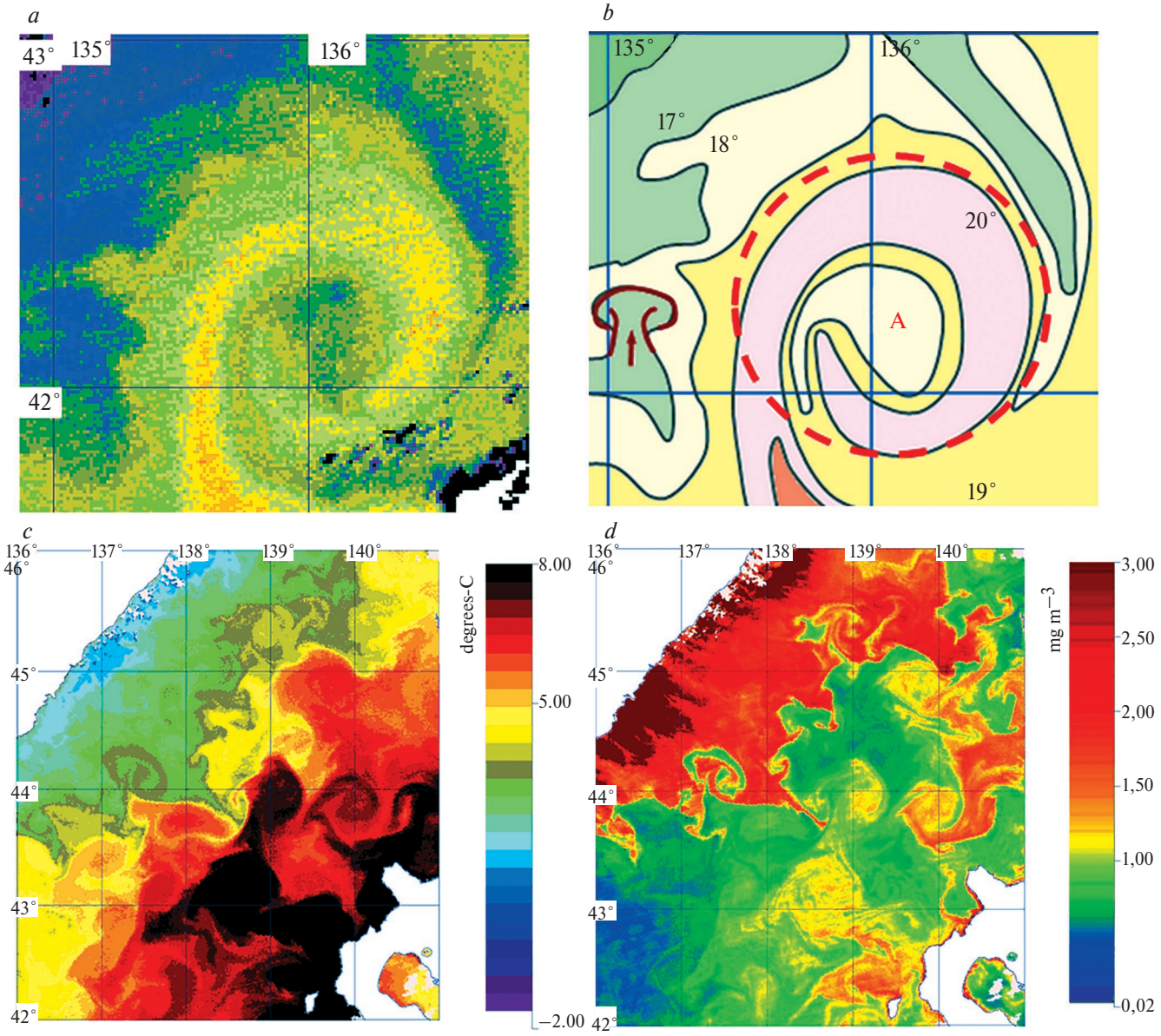

Fig. 4. Fragment of the spatial distribution of sea surface temperature reconstructed from MODIS/Terra satellite data for 19.09.2020. 12:38 UTC (*a*), fragment of the map-scheme constructed from the results of satellite image interpretation for 19.09.2020 (*b*); spatial distribution of sea surface temperature (*c*) and chlorophyll-a (*d*) for 20.04.2021. 3:36 UTC (MODIS/Aqua).

due to the warming of the surface layer of the ocean; in this case, the information of the optical range of the spectrum — the spatial distribution of *chlorophyll-a* — was additionally used to distinguish eddy boundaries when constructing map schemes. Such parameter of the upper layer of sea water is also a good enough indicator of currents, eddy formations and serves for characterization of water masses. We observed abundant phytoplankton development in cool subarctic waters of the Primorsky Current and weak in subtropical warm waters of the Tsushima Current (Fig. 4c, *d*). In the frontal zone, eddy formation is observed in satellite images during the interaction of these waters.

Based on the results of satellite imagery interpretation, schematic maps of surface water thermal structure distribution were constructed and the position of fishing vessels was plotted on them. On the maps trawling sites with maximum catch are marked with shaded circles, ovals — areas where several vessels operated.

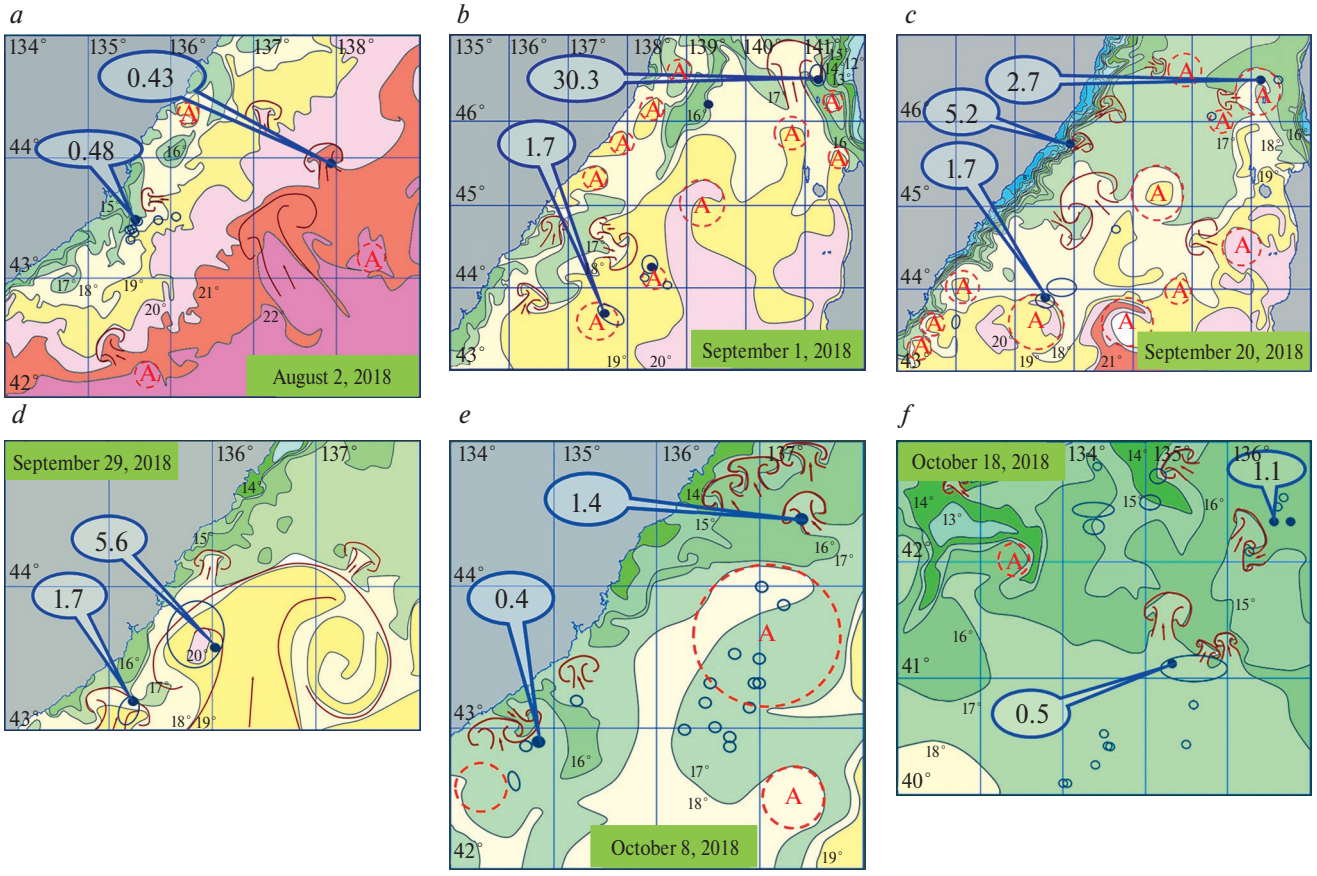

Fig. 5. Maps-schemes of the thermal structure of waters constructed from satellite observations with squid fishing areas in the Sea of Japan for August-October 2018: Notation: A – anticyclonic eddy; ○ — TC catches (t); ● — locations with maximum catches (t).

RESULTS AND DISCUSSION

Long-term satellite observations show that the dynamics of water masses is carried out by jet currents, at the top of which a eddy dipole is formed (cyclonic eddy on the left side of the motion, anticyclonic on the right). Such a coherent structure is called a mushroom current (Fedorov and Ginzburg, 1988). The Pacific squid fishery in July-August 2018–2023 began when the advection of subtropical waters intensified with the exit of tropical cyclones into the Sea of Japan zone. The branches of the Tsushima and East Korean currents were oriented in the northern, northwestern direction. The jet currents penetrated both to the area of Peter the Great Bay (PGB) and to the coast of the middle and northern Primorsky area and to the southern part of the Tatar Strait.

At the beginning of August 2018, the TC fishery was mainly conducted both at the coastal front at the seaward end of Olga Bay (0.55 t) at a temperature of 17–18 °C and to the east in the anticyclonic eddy of the mesoscale mushroom current (0.43 t). Olga Bay (0.55 t) at 17–18 °C, and to the east, in the anticyclonic eddy of the mesoscale mushroom current (0.43 t), departing from the main flow of the Tsushima Current, at 20–21 °C (Fig. *5a*). In early September 2018, commercial aggregations of TC (catches up to 1.7 t) were observed in quasi-stationary anticyclonic eddies. The intrusion of the Tsushima Current waters into the southeastern part of the Tatar Strait resulted in the formation in the area of Moneron Island. A mesoscale anticyclonic eddy of the mushroom-shaped current, in which successful fishery of TC from 13 to 31 t was noted (Fig. *5b*). Commercial accumulations of TCs were observed in the anticyclonic eddy near Moneron Island. Moneron Island, which had a spiral shape, with the largest catch of 5.6 t recorded inside the eddy at 18 °C. After the impact of northwesterly winds, the coastal front was aggravated and upwelling phenomena were manifested (Fig. *5c*). The catch of TC on this front was 5.2 tons. At the end of September 2018, the fishery continued on the coastal front with increasing advection of subtropical waters. A significant catch of 5.6 t was recorded in the cyclonic eddy of a large dipole formed near the coast (Fig. *5g*). Another fishing area was observed to the southwest in the anticyclonic

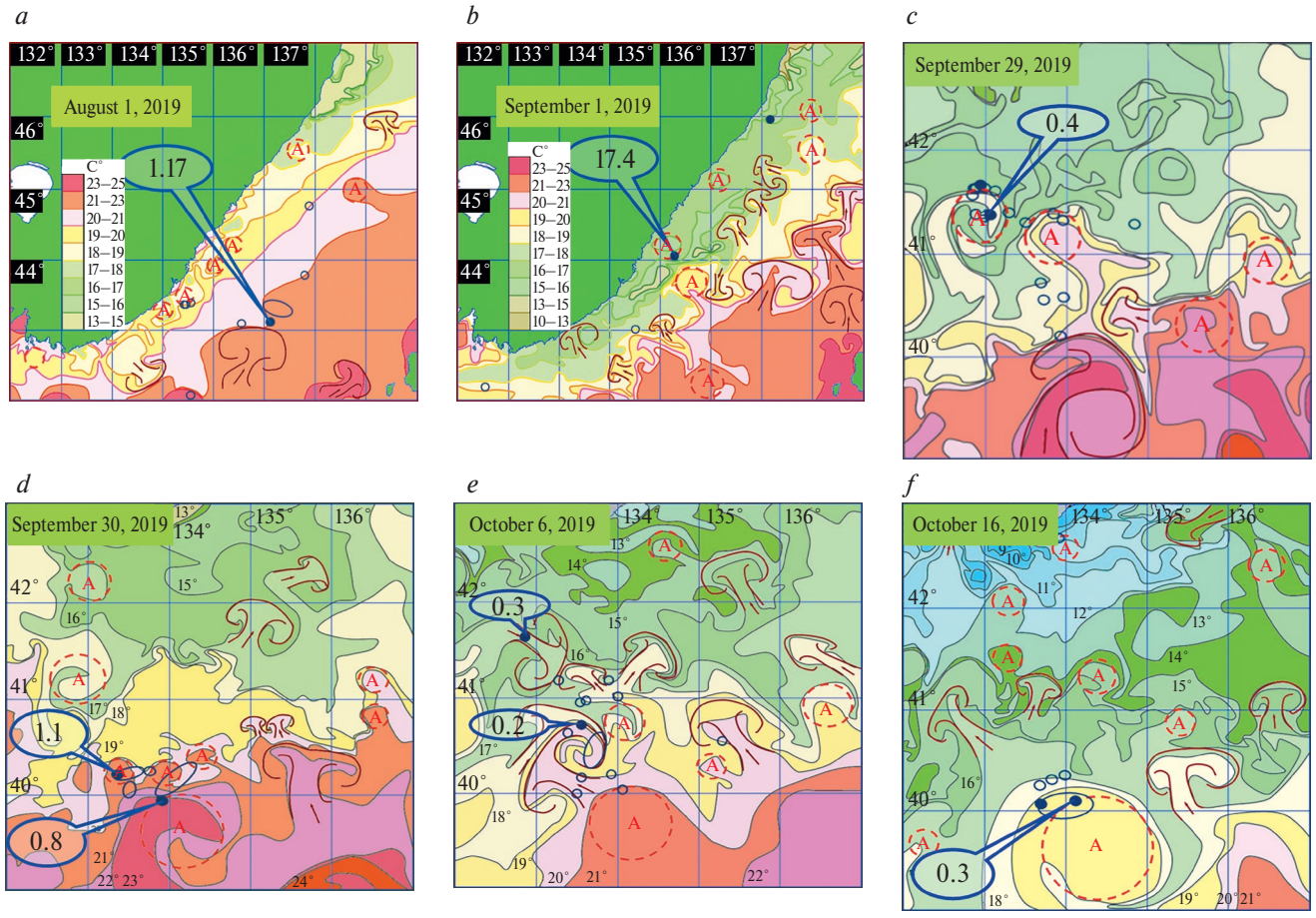

Fig. 6. Maps-schemes of the thermal structure of waters, constructed from satellite observations with squid fishing areas in the Sea of Japan for August-October 2019. Notations: see Fig. 5.

eddy of a mesoscale mushroom current at the boundary with subarctic coastal waters. The maximum catch was 1.7 tons on the "mushroom cap".

In the first decade of October 2018, the squid fishing area in northern Primorye remained in the warm current flow in a large anticyclonic eddy and near the jet feeding it (Fig. *5d*). Catches ranged from 0.2 to 0.5 t. The maximum catch of 1.5 t was observed in the cyclonic eddy of a mesoscale mushroom-shaped current directed toward the shore in a northwesterly direction (water temperature 17 °C). Catches of squid were observed near the mesoscale packing of mushroom eddies (maximum catch of 0.5 t) and near the anticyclonic eddy closer to shore at a water temperature of 17 °C. The fishing areas subsequently shifted southward (Fig. *5e*). The maximum squid catch of 1.1 t was observed in the waters of the stream from the east. Smaller catches (0.7 t) were observed further south, around . In the jet currents of warm waters (14–17 °C) approaching the coast, squid catches were 0.1–0.5 t.

In 2019, the main reason for weak squid feeding approaches to the coastal areas of Primorsky Krai and the Tatar Strait was related to the intensive Primorsky Current and weak advection of subtropical waters to the coast in summer and fall. Thus, in early August 2019, the TC fishery was conducted south of Olga Bay. Olga at the southern periphery of the mesoscale anticyclonic eddy and in the warmer waters of the Tsushima Current (Fig. *6a*). The largest catch of 0.17 t was recorded at the "cap" of the eddy dipole, while smaller catches were recorded in the frontal zone. In early September, significant catch of 17.4 t of TC was recorded in the area of the middle Primorsky Krai at the southern periphery of a mesoscale anticyclonic eddy (Fig. *6b*). Successful fishing was conducted north of on the coastal front. In late September, with the retreat of subtropical waters southward, the fishing area also shifted southward. Fishing for TC (catches of 0.3–0.4 tons) was conducted in the moray zone south of Nakhodka Bay. Finding not only in the center of the anticyclonic eddy at the top of the warm jet current, but also at its northern periphery (Fig. *6c*). The eddy had a spiral structure, and relatively cold subarctic waters were observed flowing into it. The TC catches

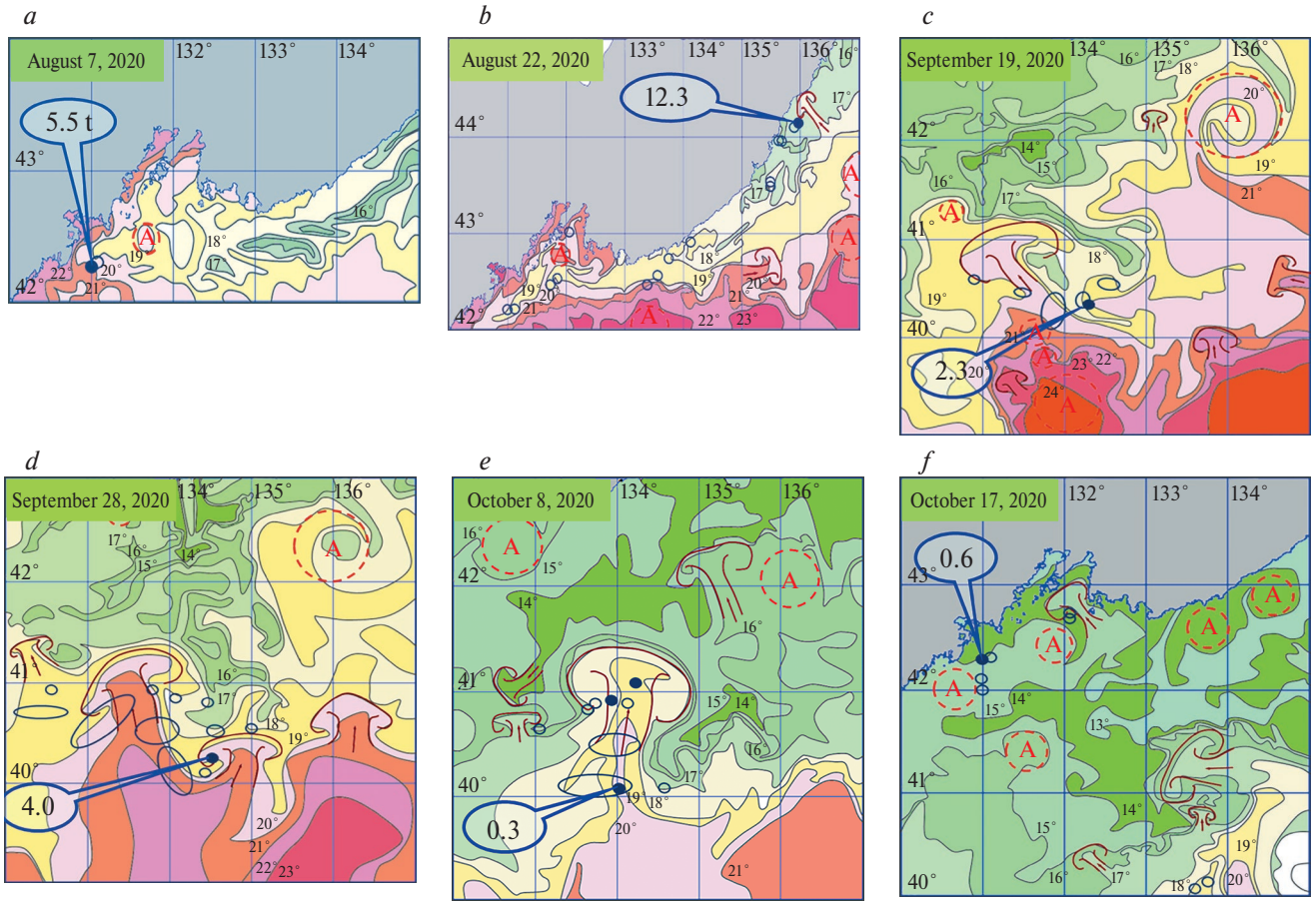

Fig. 7. Maps-schemes of the thermal structure of waters constructed from satellite observations with squid fishing areas in the Sea of Japan for August-October 2020. Notation: see Fig. 5.

associated with the frontal zone were at the northern periphery of the neighboring mesoscale eddy, which ended the jet invasion of subtropical waters at 134°E. The squid fishing was conducted at the northwestern periphery of the mesoscale anticyclonic eddy at the top of the warm subtropical water inlet with a temperature of 23 °C (Fig. *6d*). There was a catch of 0.88 t at its northwestern periphery, but the largest catch of 1.1 t was observed in the center of the mesoscale anticyclonic eddy with center coordinates 40°12'N, 133°25'E. The mesoscale anticyclonic eddy (Fig. *6d*), in which the maximum catch was observed on September 30, increased and its spiral structure was manifested. The eddy was fed by water from a large anticyclonic eddy and a jet current from the west. The marked eddy appeared to be common in the packing of the two mushroom-shaped currents, within which a catch of 0.22 t was observed. To the north, 0.3 t were caught in the main jet of a mushroom-shaped structure from the waters of the East Korea Current, whose eddy dipole located between 41–42°N and 133°E. Some small catches were associated with eddy interaction zones. In mid-October, the general temperature background decreased, and commercial aggregations were again found at the northern periphery of a large anticyclonic eddy at 18 °C (Fig. *6e*).

The hydrological conditions in 2020 differed significantly from the two previous years. In summer, the intensity of the Primorsky Current was high and the East Korean Current was low. Only some insignificant jet currents reached the Peter the Great Bay. Only some insignificant jet currents reached Peter the Great Bay. In general, the squid fishing areas were connected with subtropical water flows, anticyclonic eddies, mushroom-shaped currents in their tops and also in the zone of interaction of eddy structures. Thus, in the top of a warm current at a temperature of 19–20 °C, a catch of 5.5 tons of TC was recorded (Fig. *7a*). The map for August 22 shows the coordinates of fishing sites from August 21 to 31 (Fig. *7b*). Compared to the beginning of August, the advection of warm waters to the north increased, and squid fishing was conducted on the coastal front, in the zone of interaction between warm and relatively cold waters of the PGB (catches from 0.3 to 1.5 t). A large catch

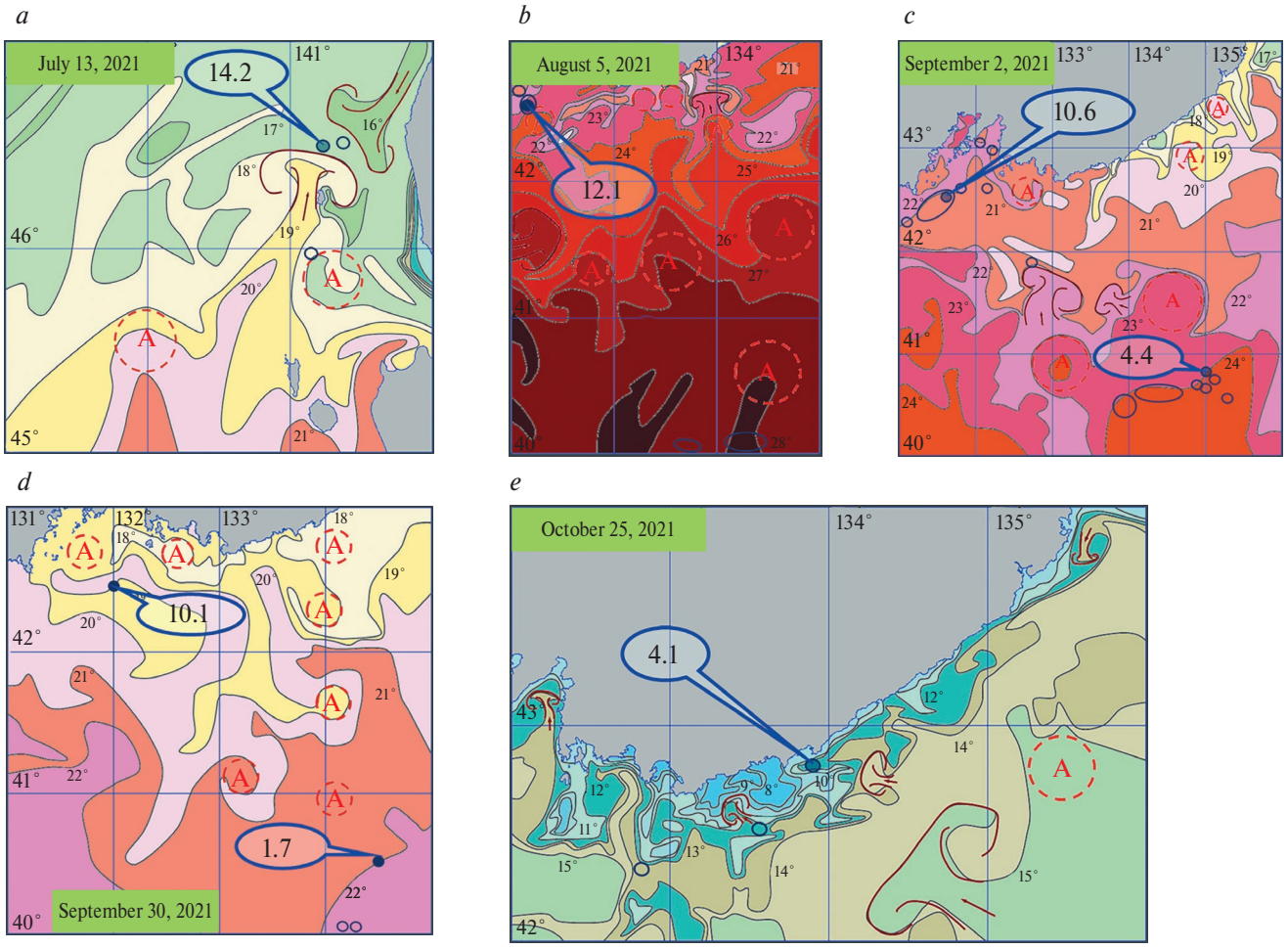

Fig. 8. Maps-schemes of the thermal structure of waters constructed from satellite observations and with squid fishing areas in the Sea of Japan for July-October 2021. Symbols: see Fig. 5.

of 12.3 t was recorded only in the vicinity of the cyclonic eddy of the mushroom-shaped mesoscale current near the coastal front. In September, the fishery was in the intrusions of warm waters of the second branch of the Tsushima Current at water temperatures of 19–21 °C, where the maximum catch was 2.3 t (Fig. *7c*). The entire fishery was conducted between 133–135° E in heterogeneities of the moribund branch of the warm current (Fig. *7d*). The largest catch of 4 t was recorded in the cyclonic eddy of the mushroom-shaped current, which separated from the main flow in the northeastern direction. In early October, fishing areas were in the main jet of the moribund branch of the warm current at 134° E, where catches were 0.3 t at water temperatures of 19–20° C (Fig. *7d*). Insignificant catches were observed in the cyclonic eddy of the dipole formed at the top of the dipole and in the anticyclonic eddy of the mesoscale mushroom current. In mid-October, small catches of squid were observed in the PGB (Fig. *7e*), and one fishing area was located in the zone of interaction of the established anticyclonic eddy with relatively warm waters of the East Korean Current and subarctic coastal waters.

The largest catch was 0.6 tons. Fishing was also conducted in the southern part of the Ussuriysky Bay at the periphery of the cyclonic eddy of the mushroom-shaped current with water temperature of 15 °C.

In 2021, the squid fishery started earlier than in previous years because the Tsushima Current and its branches were already intense in June. The main squid fishing areas were: the PGB and the moribund branch of the Tsushima Current between 133–134°E. (Figure 8). In July, squid was also caught in the southern part of the Tatar Strait. The intrusion of the Tsushima Current waters into the southeastern part of the Tatar Strait resulted in the formation of a mesoscale mesoscale in the area of Moneron Island. A mesoscale mushroom-shaped current was formed near Moneron Island (Fig. *8a*). Commercial accumulations of TC were observed in the anticyclonic eddy near Moneron Island. The largest catch of 14.2 tons was recorded

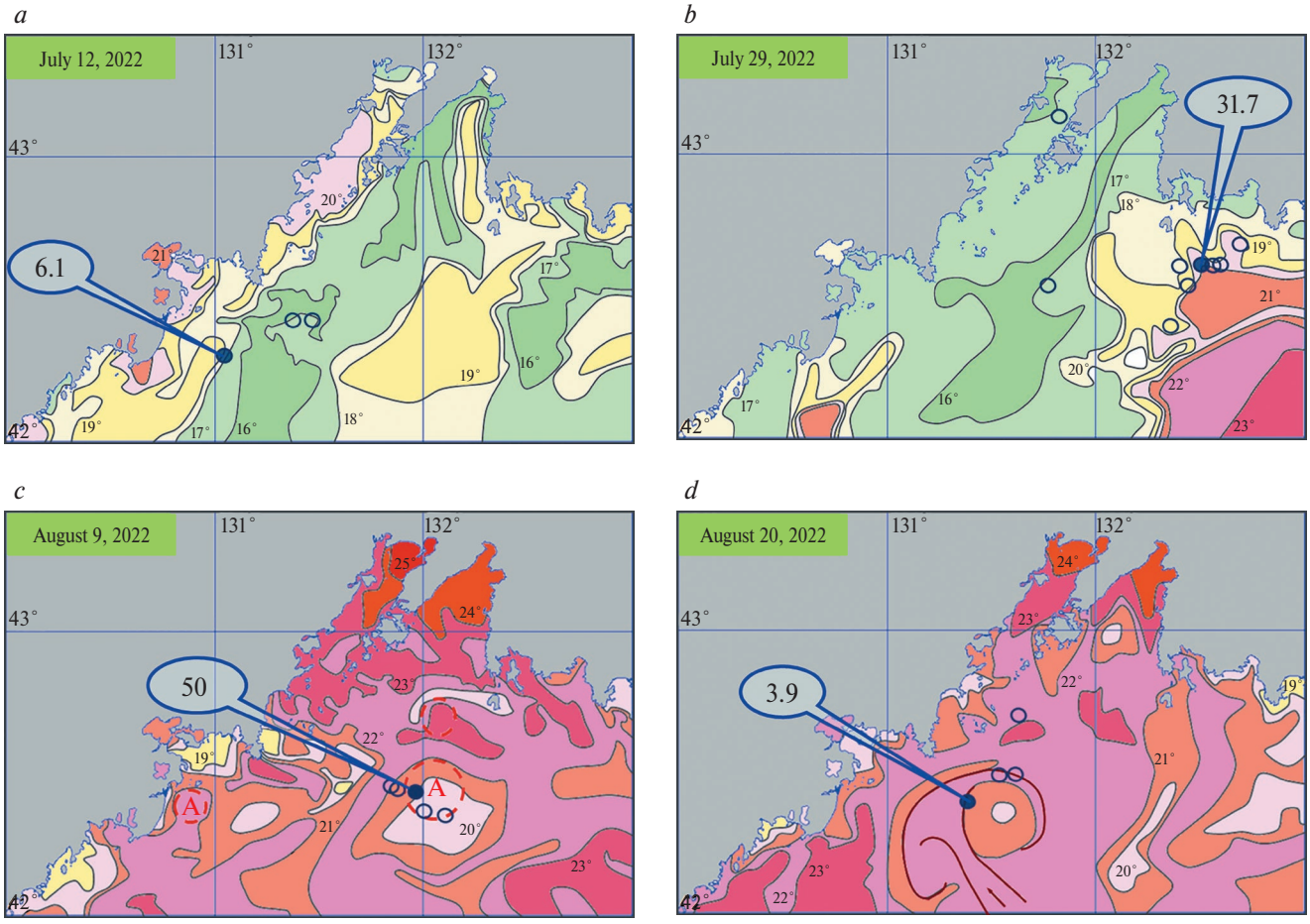

Fig. 9. Maps-schemes of the thermal structure of waters constructed from satellite observations with squid fishing areas in the Sea of Japan for July-August 2022. Symbols: (see Fig. 5).

at the top of the "cap" of the mushroom-shaped current at 17–18 °C. In general, fishing areas were associated with subtropical water flows and their interaction with subarctic waters (Fig. 8d, *e*).

During the 2022 fishing season, the main areas of fishing for TC were the PGB, its central and northeastern parts (Fig. 9), which were connected with warm water inlets by the East Korean and moribund currents (Fig. 9a, *b*). Fishing was mainly observed in the central part of the bay in the subtropical water inlets on the low-gradient front and in the zone of small-scale eddies (Fig. 9c, *d*). In the middle of August, with the retreat of warm waters and weakening of the moribund branch of the warm current against the background of strengthening of the Seaside Current, the TC fishery ended. Further, the squid approaches to the PGB were insignificant

In 2023, the squid fishery began in the PGB in the third decade of July with the approach of warm waters of the East Korean Current to the bay and their interaction with the waters of the Primorsky Current, which was characterized by strong intensity (Fig. *10a*). Its waters occupied the entire coastline of Primorsky Krai. The advection of the Tsushima Current was weak. In late August and early September, Russian vessels continued fishing for TC at the southern boundary of the PGB in the warm water inlets, while foreign vessels fished in the moribund zone (40,5°N, 135,2°E) (Fig. 10b, *c*).

The distribution of Pacific squid fishing areas in September 2018–2023 showed that in 2018squid aggregations were observed in the northern area and in the southern part of the Tatar Strait (Fig. *11a*). In subsequent years, fishing areas were observed much further south (Fig. 11b, *c, d, e*). Despite favorable hydrological conditions in the Sea of Japan, no significant northward migration of TCs was observed, which may indirectly indicate low TC abundance in the Sea of Japan, since in years of high abundance the Pacific squid fishing areas reach the Tatar Strait, while in years of low stock levels the fishing areas reach Olga Bay at best, and in recent years — Peter the Great Bay.

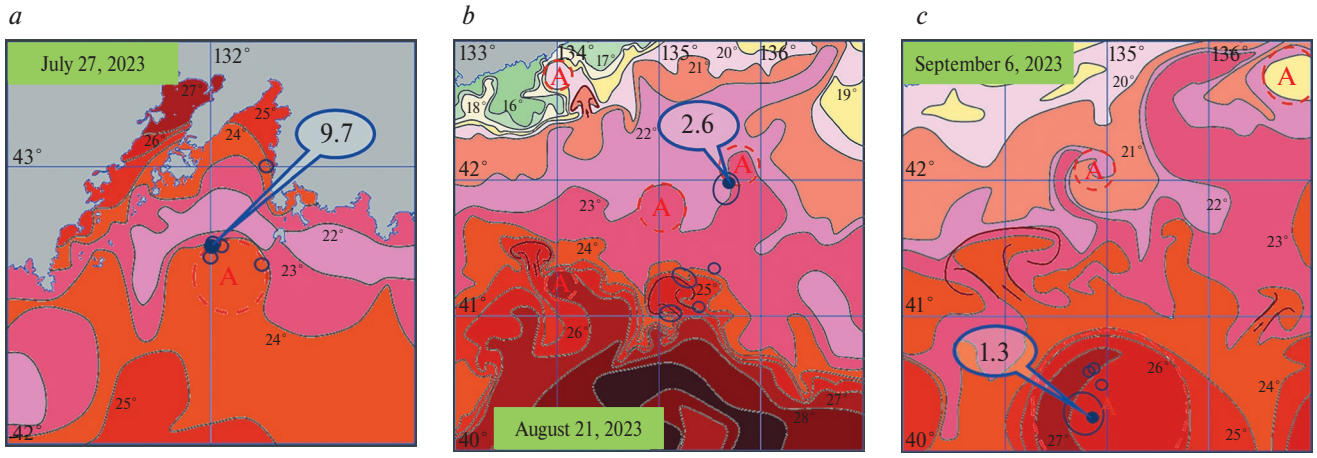

Fig. 10. Maps-schemes of the thermal structure of waters constructed from satellite observations with squid fishing areas in the Sea of Japan for July-September 2023. Symbols: (see Fig. 5).

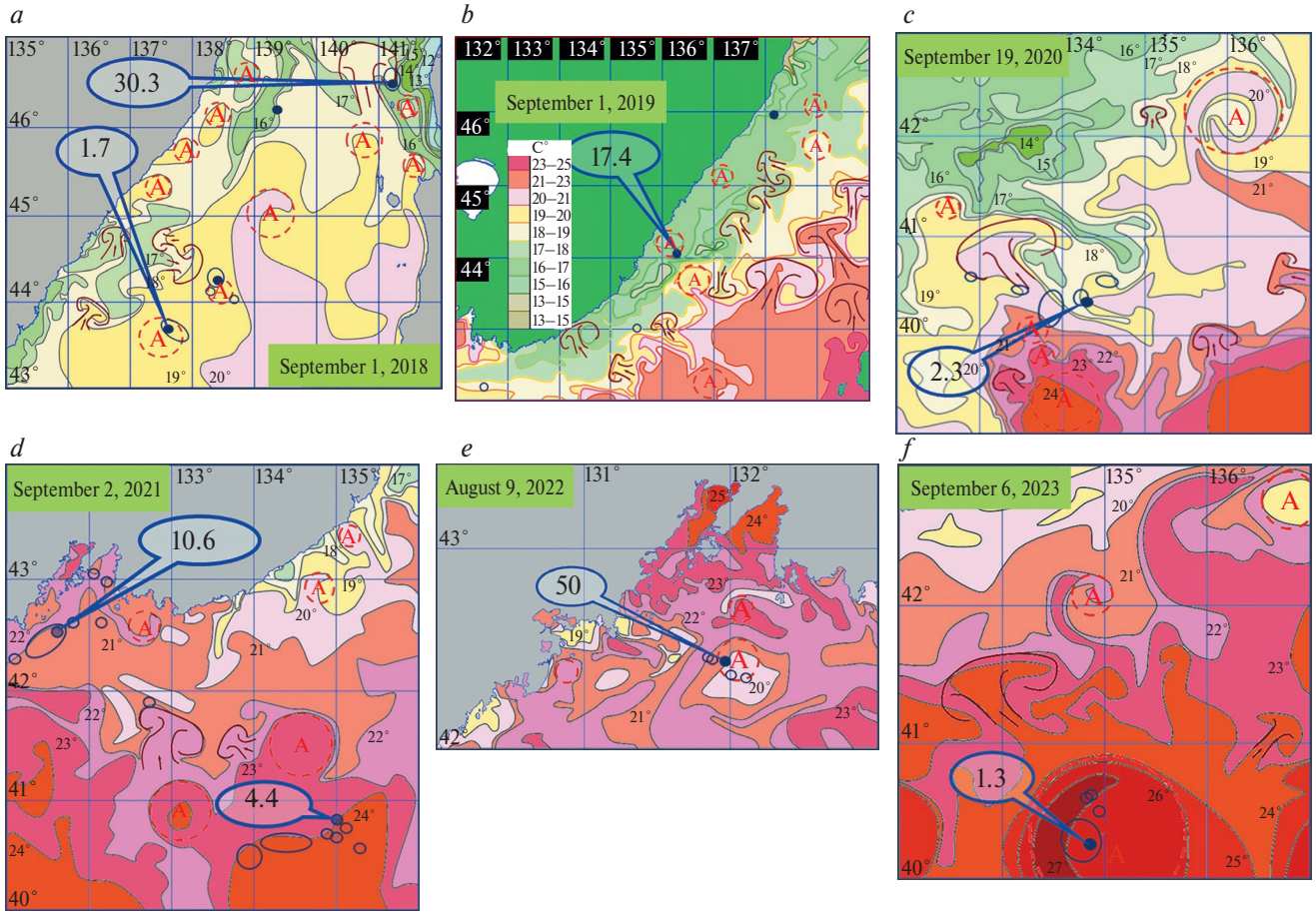

Fig. 11. Maps-schemes of the thermal structure of waters constructed from satellite observations with squid fishing areas in the Sea of Japan in September 2018–2023. Notation: (see Fig. 5).

CONCLUSION

In the field of spatial distribution of ocean surface temperature, elements of the structure of waters in which the Pacific squid fishery was successful were determined. Comparison of the elements of hydrological situation, interpreted from infrared satellite images, with fishing areas allowed to establish that the formation of TC fishing areas depended on the development or weakening of branches of the Tsushima and

Primorsky currents, the presence of mesoscale eddy structures in their waters. The accumulations of TCs in most cases were confined to areas of eddy upwelling. The maximum catches were concentrated at the periphery of subtropical anticyclonic eddies bordering subarctic waters. If the eddy had a spiral structure, the accumulations are mainly concentrated in the center of the eddy. If the outflow of subtropical waters took the form of a mushroom-shaped current, large catches were mainly noted in the jet stream and in the zone of anticyclonic and cyclonic eddies of the dipole. In the frontal zone of subtropical and subarctic waters, squid fishing areas were located on the warm side of the Subarctic (Polar) front. It was noted that with the decrease of squid abundance the geography of fishing areas also changed.

This work was carried out to accumulate statistical data on the location of commercial aggregations of TC in a particular hydrological structure identified from satellite data and to improve short-term forecasting during the fishing season.

REFERENCES

1. *Aleksanin A.I., Aleksanina M.G.* Monitoring termicheskih struktur poverhnosti okeana po dannym IK-kanala sputnikov NOAA na primere Prikuril'skogo rajona Tihogo okeana // Sovremennye problemy distancionnogo zondirovaniya Zemli iz kosmosa. Fizicheskie osnovy, metody i tekhnologii monitoringa okruzhayushchej sredy, potencial'no opasnyh yavlenij i ob"ektov. Iss. 3. Vol. II. Moskva, OOO «Azbuka-2000». 2006. Pp. 9–15 (In Russian).

2. *Belonenko T.V., Kozub P.K.* Vihrevoj apvelling kak mekhanizm sozdaniya blagopriyatnyh uslovij skoplenij sajry v YUzhno-Kuril'skom rajone // Sovremennye problemy distancionnogo zondirovaniya Zemli iz kosmosa, 2018. Vol. 15. No. 1. Pp. 221–232. 18

3. *Bulatov N.V., Samko E.V., Cypysheva I.L.* Okeanologicheskie obrazovaniya, blagopriyatnye dlya koncentracii pelagicheskih ryb po infrakrasnym dannym ISZ NOAA / Sovremennye problemy distancionnogo zondirovaniya Zemli iz kosmosa. 2008. Vol. 2. No. 2. Pp. 49–61 (In Russian).

4. *Ginzburg A.I., Kostyanoj A.G., Ostrovskij A.G.* Poverhnostnaya cirkulyaciya YAponskogo morya (sputnikovaya informaciya i dannye drejfuyushchih buyov) // Issledovaniya Zemli iz kosmosa. 1998. No. 1. Pp. 66–83 (In Russian).

5. *D'yakov B.S.* Vliyanie cirkulyacii vod na prostranstvennoe raspredelenie promyslovyh skoplenij tihookeanskogo kal'mara v YAponskom more // Izv. TINRO. 2003. Vol. 134. Pp. 258–265 (In Russian).

6. *Mokrin N.M., Slobodskoj E.V.* Rukovodstvo po poisku i promyslu pelagicheskih kal'marov v Yaponskom more i Yuzhno-Kuril'skom rajone. Vladivostok. TINRO-centr. 1998. P. 61 (In Russian).

7. *Mokrin N.M., Hen G.V.* Okeanologicheskie osnovy raspredeleniya, migracii i dinamiki chislennosti tihookeanskogo kal'mara // Gidrometeorologiya i gidrohimiya morej: Vol. VIII. Yaponskoe more. Iss. 2. SPb.: Gidrometeoizdat. 2004. Pp. 248–255 (In Russian).

8. *Nikitin A.A.* Osnovnye cherty prostranstvennogo raspredeleniya frontov v vodah Yaponskogo morya i ih izmenchivost' // Issledovaniya Zemli iz kosmosa. 2006. No. 5. Pp. 49–62 (In Russian).

9. *Nikitin A.A., Yurasov G.I.* Sinopticheskie vihri YAponskogo morya po sputnikovym dannym // Issledovanie Zemli iz kosmosa. 2008. No. 5. Pp. 1–16 (In Russian).

10. *Nikitin A.A., Danchenkov M.A., Lobanov V.B.* Puti perenosa subtropicheskih vod v rajon Dal'nevostochnogo Morskogo zapovednika. /In: Dal'nevostochnyj morskoj biosfernyj zapovednik. Issledovaniya. Kollektivnaya monografiya. Otv. red. A. N. Tyurin. Vol. 1. Vladivostok. Dal'nauka. 2004. Glava V. Gidrologiya i meteorologiya rajona zapovednika. 2004. Pp. 314–319 (In Russian).

11. *Novikov Yu.V., Slobodskoj E.V. Shevcov G.A.* Vliyanie okeanologicheskih uslovij na raspredelenie i biologicheskie osobennosti massovyh vidov kal'marov v YUzhno-Kuril'skom rajone. Okeanologiya. Morskaya biologiya. 2007. Vol. 47. No. 2. Pp. 259–265 (In Russian).

12. *Savinyh V.F., Shevcov G.A., Karyakin K. A. Slobodskoj E.V., Novikov Yu.V.* Mezhgodovaya izmenchivost' migracij nektonnyh ryb i kal'marov v tihookeanskie vody yuzhnyh Kuril'skih ostrovov // Voprosy ihtiologii. Vol. 43. No. 6. 2003. Pp. 759–771 (In Russian).

13. *Samko E.V., Bulatov N.V.* Issledovanie svyazi polozheniya ringov Kurosio s teplym yadrom i raspredeleniya promysla sajry po sputnikovym dannym // Issledovaniya Zemli iz kosmosa. No. 2. 2014. Pp. 18–26 (In Russian).

14. *Fedorov K.N., Ginzburg A.I.* Pripoverhnostnyj sloj okeana // Leningrad, Gidrometeoizdat. 1988. P. 303 (In Russian). 19

15. *Shuntov V.P.* Biologiya dal'nevostochnyh morej Rossii. Vladivostok: TINRO-Centr. Vol. 2. 2016. P. 604 (In Russian).

16. *Gong Y., Jeong H.D., Suh Y.S., Park J.H., Seong K.T., Kim S.W., Choi K.H., An I.S.* Fluctuation of Pelagic Fish Populations in Relation to the Climate Shifts in the Far-East Region // J. Ecol. Field Biol. 2007. No. 30 (1). Pp. 23–38.

17. *Kasahara S.* Descriptions of offshore squid angling in the Sea of Japan, with special reference to the distribution of common squid (Todarodes pacificus Steenstrup); and on the techniques for forecasting fishing conditions // Bull. Jap. Sea Reg. Fish. Res. Lab. — 1978. — Vol. 29. — Pp. 179–199.

18. *Kidokoro H., Goto T., Nagasawa T., Nishida H., Akamine T., and Sakurai Y.* 2010. Impact of a climate regime shift on the migration of Japanese common squid (Todarodes pacificus) in the Sea of Japan. — ICES Journal of Marine Science, 67: 1314–1322.

19. *Mokrin N.M., Novikov Yu. V., Zuenko Yu.I.* Seasonal Migrations and oceanographic conditions for concentration of rhe Japanese flying squid (todarodes pacificus steenstrup, 1980) in the northwestern Japan Sea. Bulletin of marine science. 2002. Vol. 71(1). Pp. 487–499.

20. *Sakurai Y., Kidokoro H., Yamashita N., Yamamoto J., Uchikawa K., H. Takahara.* Todarodes pacificus, Japanese common squid // Rosa R. Pierce G. O'Dor R. (ads.). Advances in squid biology, ecology and fisheries. Pt. 2: Oegopsid squids. New York: Nova Science Publishers. 2013. Pp. 250–270.

EARTH RESEARCH FROM SPACE, 2025, No. 1, pp. 74–86

USING SATELLITE INFORMATION ABOUT THE EARTH

SEASONAL AND INTERANNUAL VARIATIONS IN OCEAN SURFACE TEMPERATURE IN THE AREA OF THE NORTHERN KURIL ISLANDS ACCORDING TO SATELLITE DATA

© 2025 G. V. Shevchenko[a, b, *], Zh. R. Tshay[a], and D. M. Lozhkin[a]

[a] *Sakhalin Branch of "VNIRO" ("SakhNIRO"), Yuzhno-Sakhalinsk, Russia*

[b] *Institute of Marine Geology and Geophysics Far Eastern Branch Russian Academy of Sciences, Yuzhno-Sakhalinsk, Russia*

**e-mail: shevchenko_zhora@mail.ru*

Received May 06, 2024

Abstract. The average monthly values of ocean surface temperature in the area of the North Kuril Islands for 1998–2022 are analyzed. On the basis of a 25-year series of observations, the norms are calculated for each month — the average long-term distributions. It is shown that in the coastal area from the Simushir Island to the Fourth Kuril Strait, a cold spot area with very low temperatures (about 6 °C) and small annual cycle amplitudes (about 3 °C) is formed in summer. Seasonal fluctuations are characterized by an annual cycle with maximum values in August–September and minimum values in February–March. In general, they are well described in the region by a combination of annual and semi-annual harmonics with amplitudes of 4.9 and 1.1 °C, respectively. The interannual variability is reflected in variations of summer maxima with a period of about six years. In the summer and autumn period, outside the cold spot area, there is a steady trend towards an increase in temperature, the most significant in the northwestern Pacific Ocean (about 1 °C in 25 years). In the winter-spring season in the Sea of Okhotsk, the reverse situation is observed with a tendency to decrease of thermal parameters. When calculating deviations of average monthly temperatures from normal values, it was revealed that large-scale zones with significant temperature anomalies, mainly negative ones, can be formed in the area of the North Kuril Islands, which can pose a serious danger to aquatic organisms.

Keywords: *thermal regime, temperature anomalies, linear trend, harmonic analysis, method of natural orthogonal functions, Kamchatka Peninsula, Sea of Okhotsk, Northwestern Pacific Ocean*

DOI: 10.31857/S02059614250107e4

INTRODUCTION

The waters adjacent to the North Kuril Islands and southeastern Kamchatka are of major commercial importance. A significant number of commercial fish species and invertebrates — Pacific salmon, pollock, cod, herring, saffron cod, saffron cod, flounder, crabs (Kamchatka crab, blue crab, Bairdi strigun), etc. are caught here. For this reason, the study of hydrological regime peculiarities of this area, seasonal and interannual variability of oceanological conditions is of considerable interest.

Comparatively few studies are based primarily on the results of ship-based oceanological surveys (Kono, Kawasaki, 1997; Kantakov, 2000; Samko, Novikov, 2004). Significantly more works are devoted to the wider Northwest Pacific Ocean (NWPO), where a wide range of data, including meteorological information, is analyzed (Joyce, Dunworth-Baker, 2003; Hen et al., 2004; Rogachev, Shlyk, 2005; Glebova et al., 2009; Byshev et al., 2016; Rostov et al., 2020, 2021; Tskhai et al., 2022). A number of papers are devoted to climatic changes in the Sea of Okhotsk (Hydrometeorology..., 1998; Hen et al., 2008, 2022; Rostov et al., 2017; Zuenko et al., 2019; Lozhkin and Shevchenko, 2019, 2022). In their article, V.I. Byshev et al. (2016) stated a very complex character of thermal variations in the NWPO.

A similar conclusion can be made with respect to the Sea of Okhotsk, where, according to oceanological soundings, an increase in heat content in various layers, a decrease in the depth of winter convection and the intensity of geostrophic flows were detected (Zuenko et al., 2019). This conclusion applied predominantly to the eastern part of the basin, where TINRO *in situ* studies are the most detailed. At the same time, according to satellite observations, a steady decrease in the surface layer temperature in winter and spring was observed in the western part of the Sea of Okhotsk (Lozhkin and Shevchenko, 2019),

which was attributed by the authors to an increase in the depth of winter convection due to a decrease in ice cover. These features determine the interest in studying the thermal regime of the area adjacent to the North Kuril Islands.

Due to the great remoteness of this area, oceanological data collection was carried out by SakhNIRO only three times — in spring 2013, 2015 and 2016, in the mode of accompanying ichthyoplankton surveys, which did not allow us to consider the peculiarities of the thermal regime on the basis of expeditionary soundings.

Unlike traditional ship-based surveys, satellite observations of ocean surface temperature (OST) are characterized by full coverage of the area and regularity of data availability. Therefore, they are the most suitable material for characterizing the spatial and temporal variations of SST in modern conditions, when the number of marine expeditions is decreasing.

MATERIALS AND METHODOLOGY

SakhNIRO has accumulated a significant amount of satellite observations of the surface temperature of the Sea of Okhotsk and adjacent waters thanks to the TeraScan® satellite receiving station (https://www.seaspace.com) installed in 1997. Since 1998, regular reception of incoming data and formation of a database, based on daily SST distributions with a spatial resolution of about 2 km, have been organized.

This study used monthly average SST data for 1998–2022 (25 years) in the region bounded by coordinates 47–52°N and 152–160°E. (Fig. 1). The initial matrix consisted of 300 temporal layers of dimension 285×284 points. For each month and spatial cell, long-term averages, which were considered as norms characterizing typical thermal regime parameters, and standard deviations σ were calculated. Anomalies as the difference between the current monthly averages and the norm were considered significant if the absolute value exceeded twice the σ value (Tskhai and Shevchenko, 2013).

The decomposition of the initial matrix by natural orthogonal functions (Bagrov, 1959) was used to determine the nature of interannual variations of SST. The amplitudes and phases of the annual and semiannual harmonics were obtained by the least squares method when analyzing seasonal temperature variations. A similar calculation was performed for the values averaged over the entire area. Also, linear trend coefficients (LTC), characterizing unidirectional trends in the interannual changes in SST, were calculated at all points of space (Lozhkin and Shevchenko, 2019). When assessing the contribution of cyclic components, the amplitude and phase of the harmonic with a given period were calculated

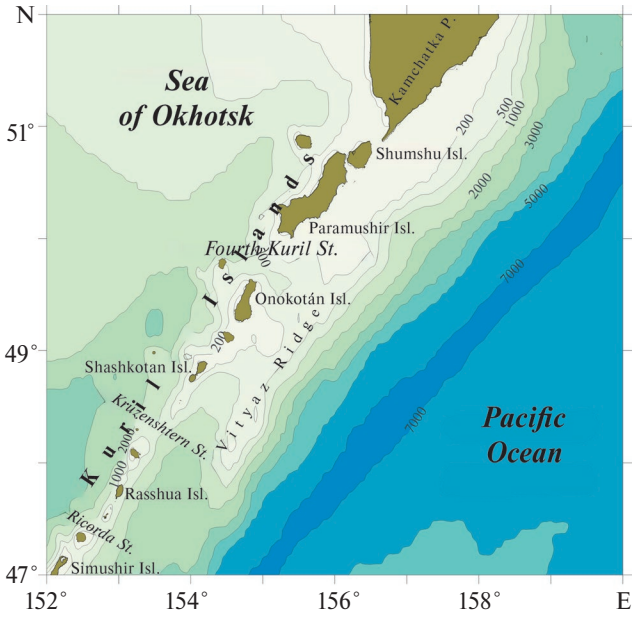

Fig. 1. Map of the study area.

from samples for August (envelope by maxima). Then this component was subtracted from the initial series; the significance of the harmonic contribution was determined by the ratio of the variance of the residual series to the variance of the initial series summed over the entire area. Periods of cyclic components were set from three to 12 years with a step of three months (Lozhkin and Shevchenko, 2020).

RESULTS AND DISCUSSION

Mean monthly SST distributions. Fig. 2 presents the mean multiyear distributions of ocean surface temperature in the area of the North Kuril Islands. In January-March, the coldest conditions are observed, characterizing, as in other Far East seas and the adjacent part of the Pacific Ocean, the winter thermal regime (Hydrology and Meteorology..., 1998). During this period over most of the area the values of SST fluctuate from 0 to +2 °C. On the shelf of the Shumshu and Paramushir Islands and also off the southeastern coast of Kamchatka they fall below zero. In general, the temperature in the Okhotsk Sea water is lower than in the Pacific Ocean.

In April, the spring processes of surface layer warming are hardly noticeable, the zone of negative temperatures over the mainland slope of southeastern Kamchatka and the northernmost Kuril Islands disappears. In May, in the waters off the Kuril Islands, SST values increase to +2 °C, and in the rest of the water area — to +3 °C. The increase in thermal indices becomes noticeable only in June, most of the area warms up to

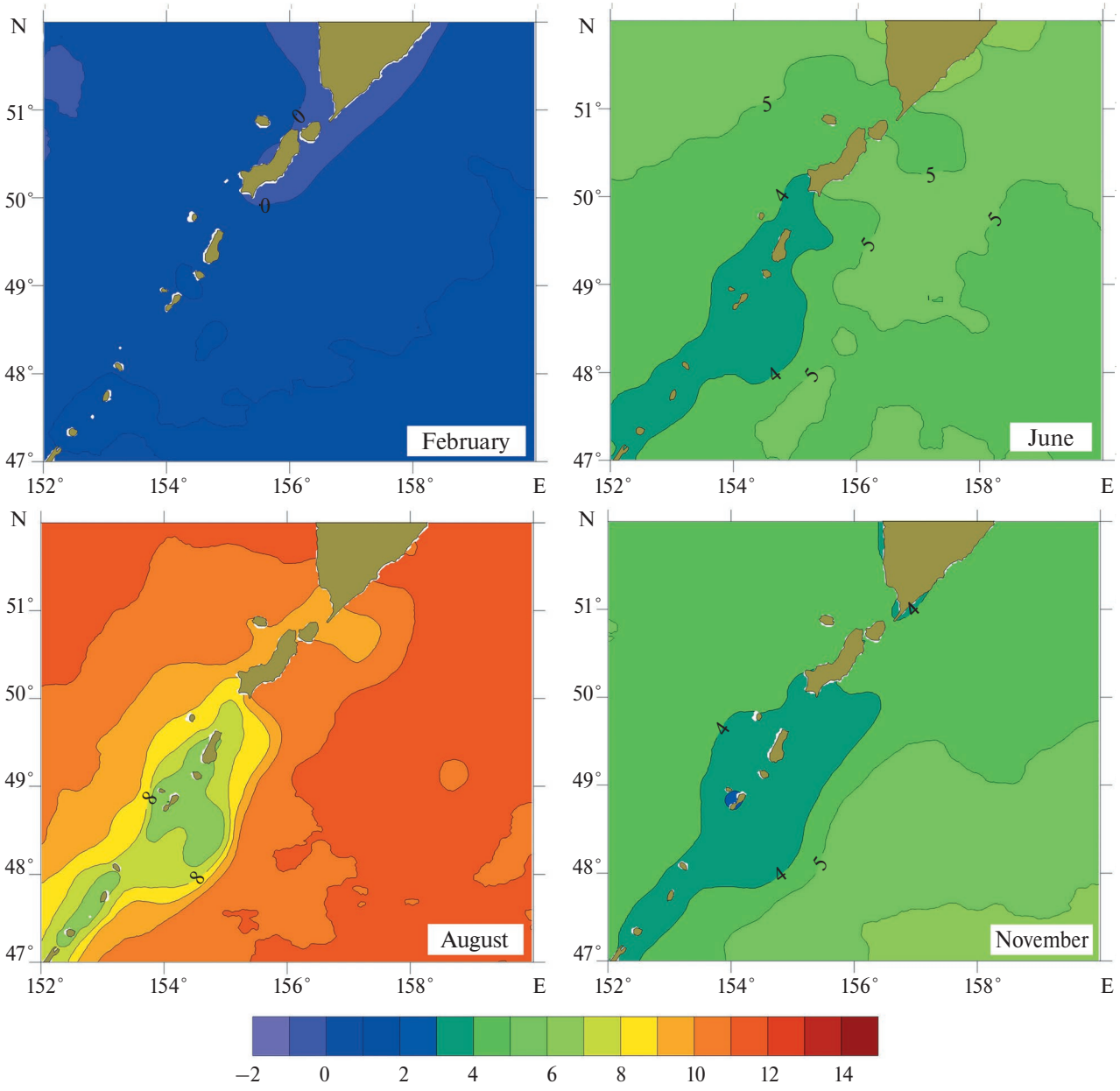

Fig. 2. Mean multiyear distribution of SST (in °C) in the area of the North Kuril Islands in winter (February), spring (June), summer (August) and fall (November).

+5–6 °C, but at the same time near the Kuril Islands to the south of Paramushir Island, the formation of the area of the Kuril Islands begins. An area of lower temperatures from +3 to +4 °C begins to form near the Kuril Islands south of Paramushir Island.

During the summer months, the spatial distribution of SST generally has the same features as in June: the coldest water is observed in the pre-Kurilian waters south of 50°N, with temperature values increasing with distance from the islands both into the open ocean and the Sea of Okhotsk. The widest area of cold water is observed in the vicinity of Shiashkotan Island. The widest area of cold water is observed near Shiashkotan Island, where a second spot appears near the sharply defined northern spur of the Vityaz Ridge. This peculiarity emphasizes the determinant role of the bottom relief in the appearance of the cold zone in this part of the Kuril Ridge covering the area from Simushir Island to the Fourth Kuril Islands. Simushir Island to the Fourth Kuril Strait.

In July, as in June, the warmest water (+9–10 °C) is mainly located to the north of the 51st parallel,

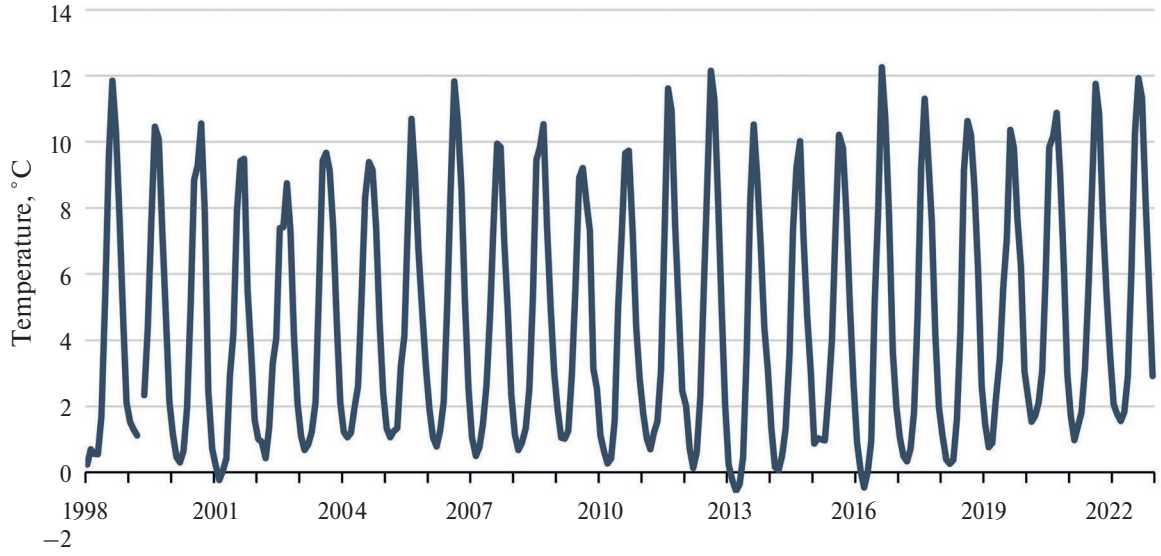

Fig. 3. Graph of SST variations (in °C) averaged over the water area off the North Kuril Islands.

and near the western boundary of the study area it extends southward to 50°N. In the main part of the area SST values vary within fairly narrow limits — +8–9 °C. As one approaches the Kuril Islands, the temperature gradient increases, and colder water (below 6 °C) is occurred in coastal areas. In August-September near the coast the values remain the same, while in the rest of the area they increase to 10–12 °C.

In October-November, the temperature distribution is similar to summer. In October, in the areas with the warmest water in the north-west and south-east of the area, the water temperature decreases most rapidly — to 8–9 °C. The area near the islands cools down to the least extent, where the minimum values drop to 4 °C. In November, the temperature does not exceed 4–6 °C in most of the area. The spatial distribution of SST is significantly transformed in December, when as a result of surface layer cooling it becomes more homogeneous and the area near the islands is no longer distinguished. Thermal indices in the coastal areas decrease to 1–2 °C, in the moribund areas — to 3 °C.

The dynamics of average monthly values of SST is presented in Fig. 3. These fluctuations are dominated by the annual variations and interannual variations are clearly visible, which are expressed primarily in the envelope of both maxima and minima (although significant changes of the latter are less typical for sea water temperature). There is also a unidirectional tendency for the SST increase, and in recent years it is clearly increasing. While the linear trend coefficient for the whole series is about 0.04 °C/year, which means an increase of 1 °C for 25 years, it is almost an order of magnitude higher (about 0.3 °C/year) when calculated for the last seven to eight years.

The graph shows well-defined variations of thermal conditions in the summer period (envelope along the maxima). In 1998, 2006, 2012, 2016 and 2022, the areas adjacent to the North Kuril Islands experienced significantly warmer conditions than in "normal" years, when water temperatures are close to long-term averages. Cold conditions in 2002, 2009, 2014 and 2019, differences in mean SST values by area reached 3.5 °C.

Quasi-rhythmic components can be traced in the variations of the SST maxima. The smallest share of the residual variance was obtained for the harmonic with a period of six years. The amplitude value of this component was close to 1 °C, the highest values were recorded in the southern part of the study area (up to 1.7 °C), the lowest — on the southeastern shelf of Kamchatka and on the ocean shelf of the North Kuril Islands.

Seasonal variations of SST. Table 1 shows statistical characteristics of seasonal variations: multiyear average values of SST for each month, the value of standard deviation σ, maximum and minimum values for the entire observation period. The maximum heating is observed in August (10.4 °C) and September (10.0 °C), the minimum — in February-March (0.7 °C).

The fluctuations are well described by a combination of the annual and semiannual harmonics. The annual variation is relatively weakly expressed, the amplitude of the annual component was 4.9 °C and its phase was 224°, which corresponds to the maximum in the middle

Table 1. Multiyear averages, standard deviation σ and extreme values of SST by months (°C)

Month	Average	Sigma	Minimum	Maximum
January	1.3	0.6	0.2	2.3
February	0.7	0.5	−0.2	1.8
March	0.7	0.6	−0.6	1.7
April	1.1	0.7	−0.4	2.2
May	2.3	0.8	0.5	3.4
June	4.8	0.8	3.1	6.0
July	8.4	0.9	7.1	10.2
August	10.4	1.2	7.4	12.3
September	10.0	0.8	8.2	11.3
October	7.5	0.7	5.5	9.0
November	4.7	0.9	2.5	6.3
December	2.5	0.6	0.7	3.5

of August. The amplitude of the semiannual harmonic is four times smaller (1.1 °C), and its phase corresponds to the maxima in early February and August. The amplitude of the annual harmonic differed significantly in different years — the lowest value was recorded in cold 2002 (4.0 °C), the highest — in warm 2016 (5.8 °C).

Let us consider the spatial distributions of amplitude and phase of annual and semiannual harmonics for the period from 1998 to 2022 (Fig. 4). It follows from the figures that the intensity of seasonal variations of SST varies not only in time, but also in space. Over most of the area both in the NWPO and in the Sea of Okhotsk, the amplitude of the annual harmonic varies from 5 to 6 °C. As it approaches the Kuril Islands, its values decrease and reach their minimum values (from 2.3 to 2.6 °C) in the areas from Onekotan Island to Shiraya Island. Onekotan Island to Shiashkotan Island and from Rasshua Island to Simu Island. Rasshua Island to Simushir Island. The phase of the annual harmonic varies within small limits — from 214 to 234°. Its minimum values, indicating a slightly earlier onset of the summer temperature maximum, are observed near the Kuril Islands and on the shelf of the Kamchatka Peninsula, while its maximum values are observed in the southeast of the study area.

Variations in the amplitude of the semiannual component are small, its values increasing from 0.7 °C in the coastal zone of the Kuril Islands to 1.4 °C in other areas. The phase of this component is also minimal in the coastal zone of the archipelago and on the southeastern shelf of Kamchatka (about 42°), and increases to 95° as one moves out to the Pacific Ocean.

Interannual variability of thermal conditions. In modern conditions, when global warming plays the main role in climate changes on the Earth, when studying variations of thermal conditions in marine areas, the question of unidirectional trends (trends) in them most often arises. Fig. 5 presents the results of calculations for different seasons of the year, where the linear trend coefficients are summarized to the values for 10 years.

The character of the spatial distribution of SST in winter (January-March) is rather complex and mosaic, but in general, a decreasing trend in SST prevails in the Sea of Okhotsk, while in the NWPO, on the contrary, an increasing trend prevails. The most significant negative trends are observed along the western boundary of the area (up to 0.5 °C/10 years or 1 °C over 20 years). The rate of increase in the Pacific Ocean adjacent to the Kuril Islands is about half as large.

In spring, the area with negative values of LTC expands at the expense of a significant part of the NWPO; positive trends are observed only in the northeastern section adjacent to the southeastern coast of Kamchatka. At the same time, the SST decrease rate decreases as compared to the winter period, while the increase rate increases up to 0.4 °C/10 years.

In summer, a warming trend prevails over most of the water area, with very high growth rates in the open ocean — up to 1.1 °C/10 years. The exception is the above-mentioned cold spot off the coast of the Kuril Islands, where a decrease in SST is observed with rather high rates (from 0.2 to 0.4 °C/10 years). In the fall, the tendency to increase the temperature of the surface water layer prevails, and the rate of increase varies from 0.3 to 0.7 °C/10 years, which can also be considered significant.

Significant SST anomalies. In fact, the warm and cold years shown above are visual estimates. At the same time, the identification of SST anomalies (deviations

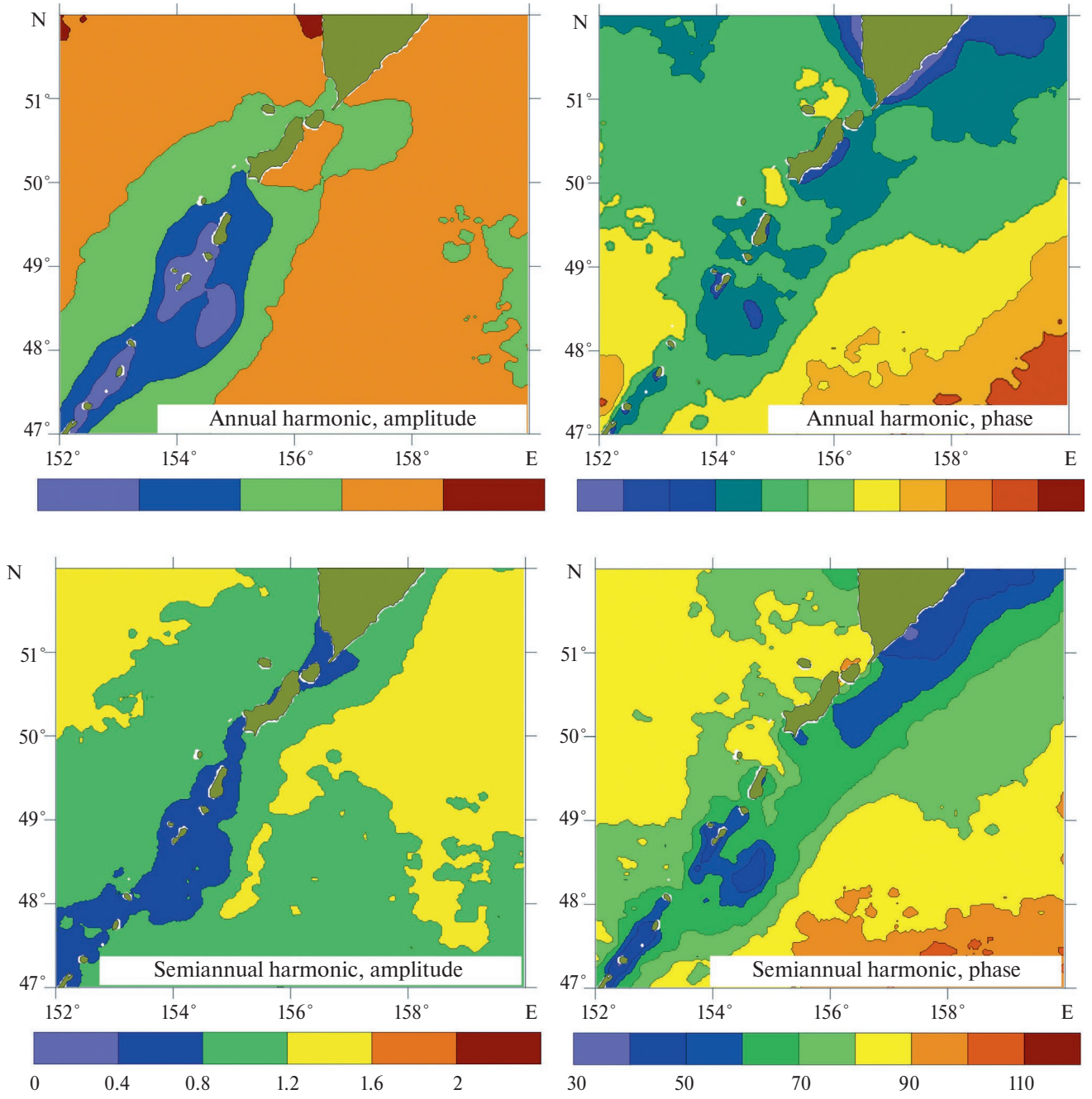

Fig. 4. Spatial distribution of the amplitude (in °C) and phase (in °C) of the annual and semiannual harmonics of SST in the area of the North Kuril Islands.

from multiyear averages, called "norms") that are large-scale in both magnitude and area is of considerable interest. Usually, deviations from the norms obey a normal distribution, for which the 2σ value corresponds to the boundary within which 95% of values lie, and going beyond it indicates extraordinary thermal conditions (some experts even use the term "thermic catastrophe") of the environment (Ustinova, 2021). If such anomalies spread over a large part of the water area, the situation becomes really dangerous for the life of hydrobionts, especially at the early stage of their development, and deserves careful study. Figure 6 presents a graph showing the proportion of the area of significant anomalies in relation to the entire study area.

Of greatest interest were the situations when such anomalies occupied a significant part of the study basin. In most cases, they appeared in small areas of 2–5% of the study area and relatively rarely exceeded

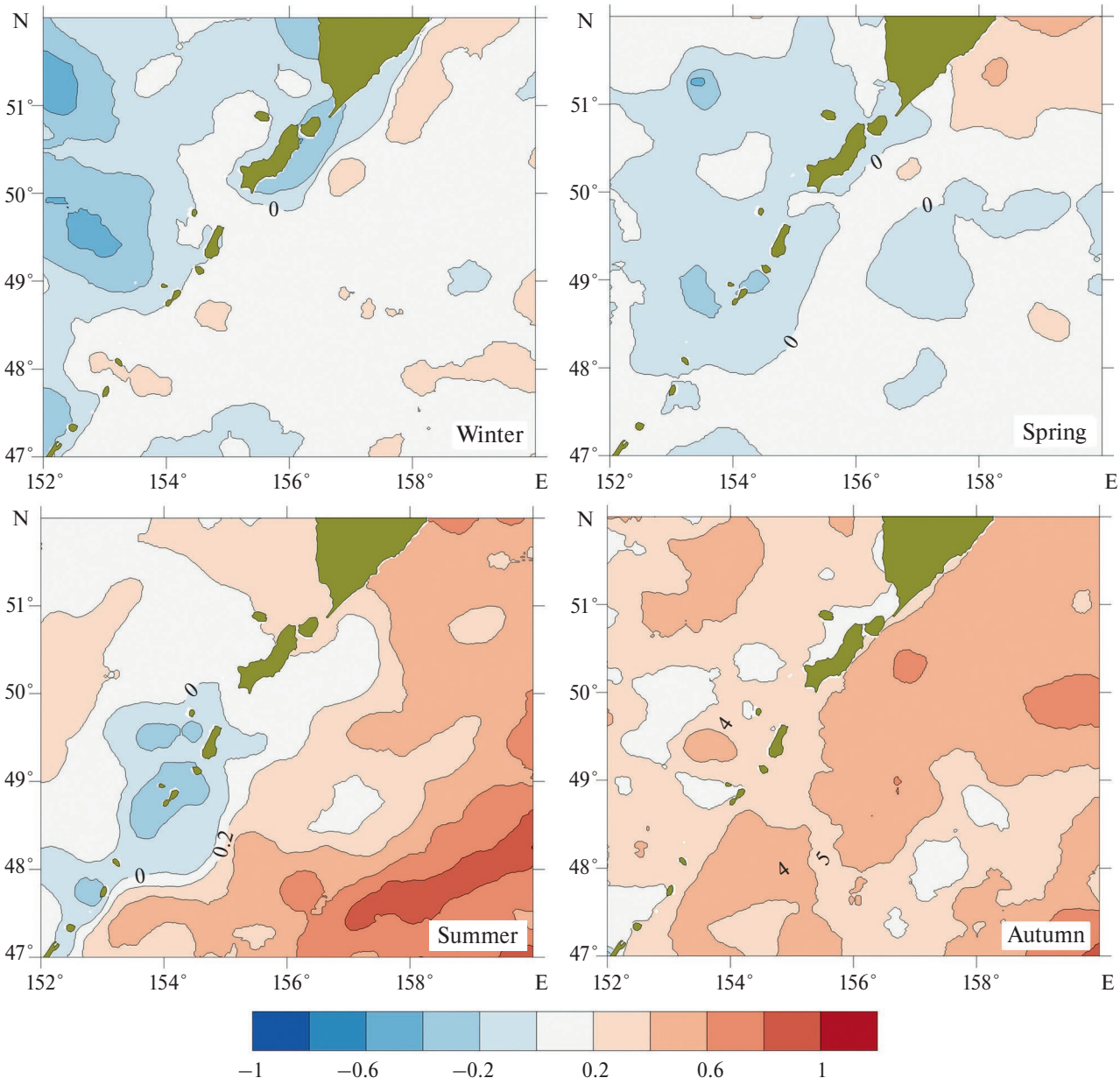

Fig. 5. Spatial distribution of linear trend coefficients in SST variations (in °C/10 years) in different seasons of the year in the area of the North Kuril Islands.

the 10% mark. Interestingly, this was not observed once during a number of years (from 2003 to 2009), and in some years repeatedly (e.g., in 2013 for six months). Note that a linear trend was not subtracted from the data when calculating the anomalies, which could have led to an increase in the number of positive anomalies in recent years. However, as can be seen from Fig. 6, this did not happen; apparently, the effects associated with the presence of a tendency to an increase in SST did not significantly affect the phenomenon under consideration.

For a more thorough analysis, situations where the area of significant anomalies was higher than 20% were selected (Table 2). There were ten of them, in nine of them negative and only in one case positive anomalies were observed. In four of them the areas of extreme temperatures occupied more than 40% and in eight cases more than a quarter of the total area. This indicates that deviations of the thermal regime from the "norm" in the North Kuril Islands can be large-scale. At the same time, cases of extremely cold conditions

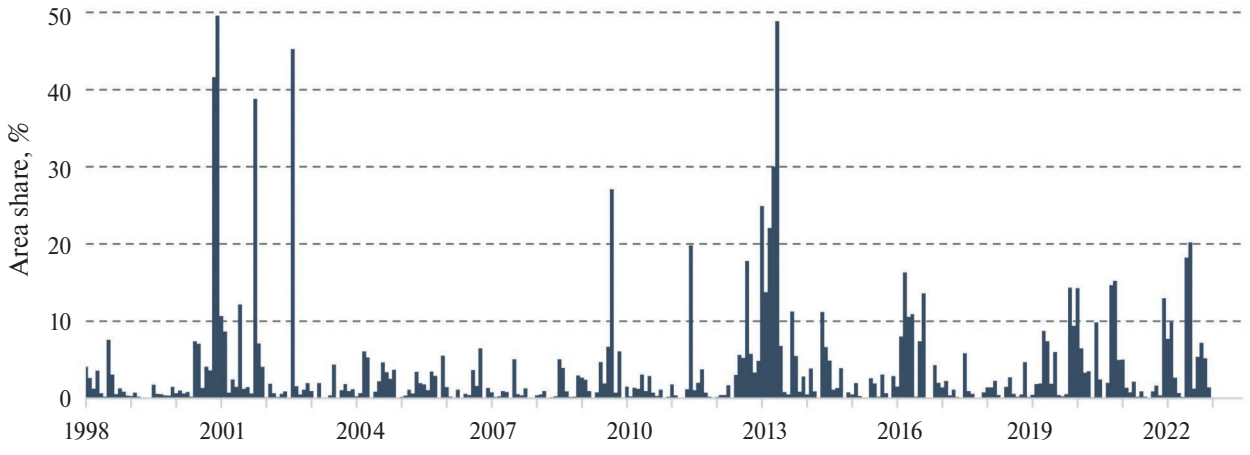

Fig. 6. Fractions of the area of extreme SST anomalies exceeding 2σ in the area of the North Kuril Islands.

clearly predominate. This disproportion is highly unusual, its physical causes are unclear and require further study.

Fig. 7 presents the spatial distributions with the most significant SST anomalies. In December 2000, the temperature in most of the area was 2 °C and in some areas 2.5 °C below the mean multiyear average. Usually, such indicators are considered as regular events, but in December, the SST variability is relatively low with the value of standard deviation of 0.6 °C (see Table 2).

In August 2002, the negative anomalies covered practically the entire area, and at the areas remote from the coast both in the Sea of Okhotsk and in the Pacific Ocean, they had a significant value from −4 to −6 °C. Near the coast of Kamchatka and the Kuril Islands, they were much smaller and did not exceed 1–2 °C.

In the spring of the "anomalous" 2013, the area of deviations exceeding 2σ in magnitude comprised more than 20% of the area during the three following months — from March to May (see Table 2). In May, almost half of the study area (49%) was in the zone of significant negative anomalies (up to 3 °C).

In August 2022, the only case when significant positive SST anomalies were recorded over a sufficiently large area was recorded. In some areas, the water temperature was 4 °C above the multiyear average. In the coastal areas of southeastern Kamchatka and Kuril Islands, the thermal indices generally corresponded to the mean multiyear average.

Decomposition of the SST field by EOF. Important features of seasonal and interannual variability can be determined using decomposition of hydrometeorological fields by natural orthogonal functions (Novinenko and Shevchenko, 2007).

Table 2. Information on the most significant SST anomalies in the area of the North Kuril Islands

Period	Share of area, %	Anomaly sign
November 2000	41.64	Negative
December 2000	49.61	Negative
October 2001	38.81	Negative
August 2002	45.25	Negative
September 2009	27.09	Negative
January 2013	24.91	Negative
March 2013	22.07	Negative
April 2013	30.03	Negative
May 2013	48.86	Negative
July 2022	20.22	Positive

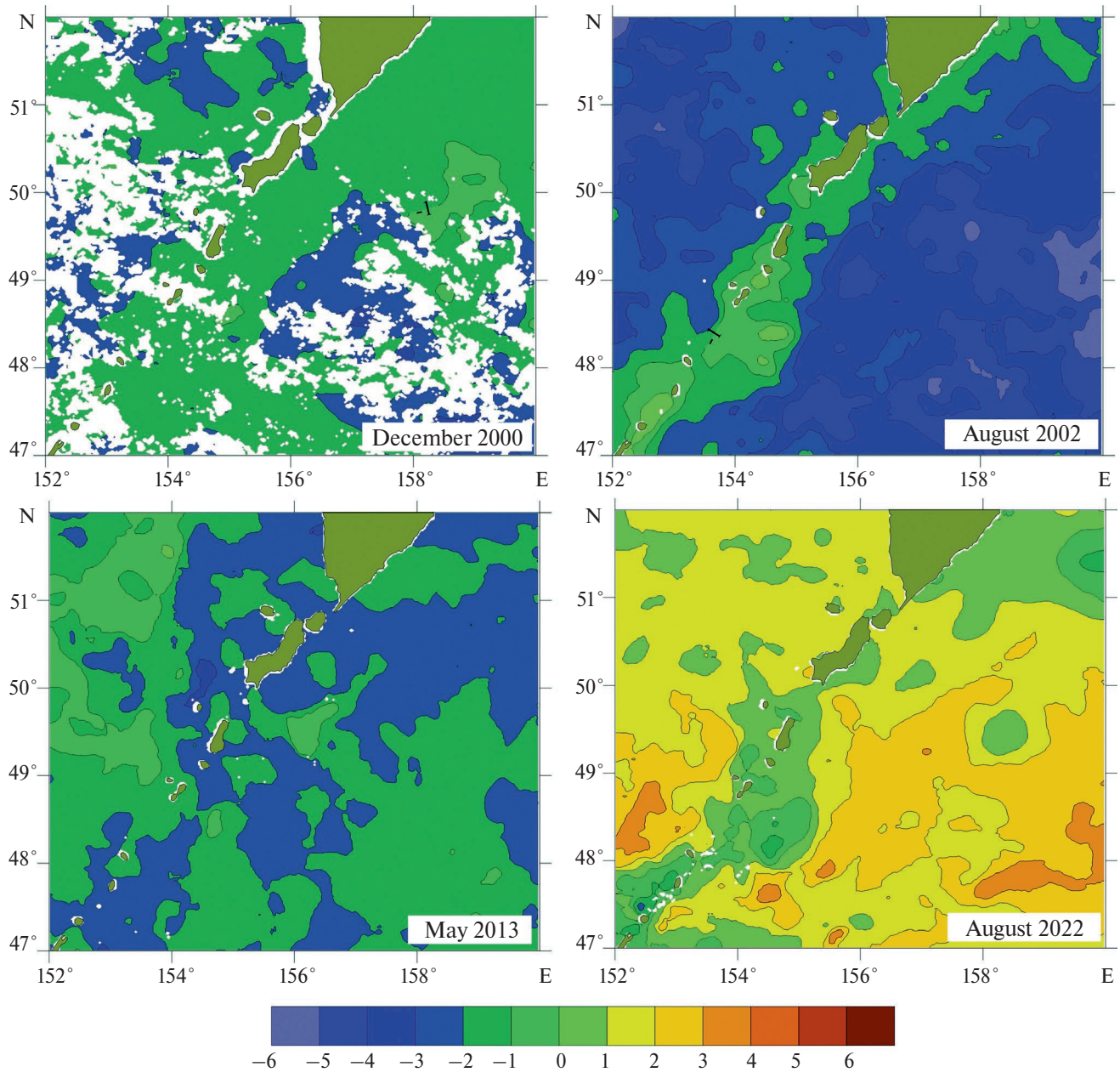

Fig. 7. Spatial distribution of the most significant SST anomalies (in °C) in the area of the North Kuril Islands.

The calculation results in the form of spatial distributions of the first three main modes (they account for 96.65; 0.51 and 0.25% of the total variance) and their corresponding time functions are presented in Fig. 8.

When the EOF method decomposes hydrometeorological fields with a pronounced seasonal course (variations in sea water or atmospheric air temperature are among the most striking examples of this kind), the first mode gives an overwhelming contribution to the total parameter dispersion, which, however, does not devalue the role of higher components.

The spatial structure of the first mode is practically identical to the averaged distribution of SST in summer (low values near the coast of the Kuril Islands and high values in the open ocean and in the remote part of the Sea of Okhotsk), and its temporal function has a very high correlation (r = 0.996) with the mean monthly temperature values. For this reason, there is no point in considering the main component

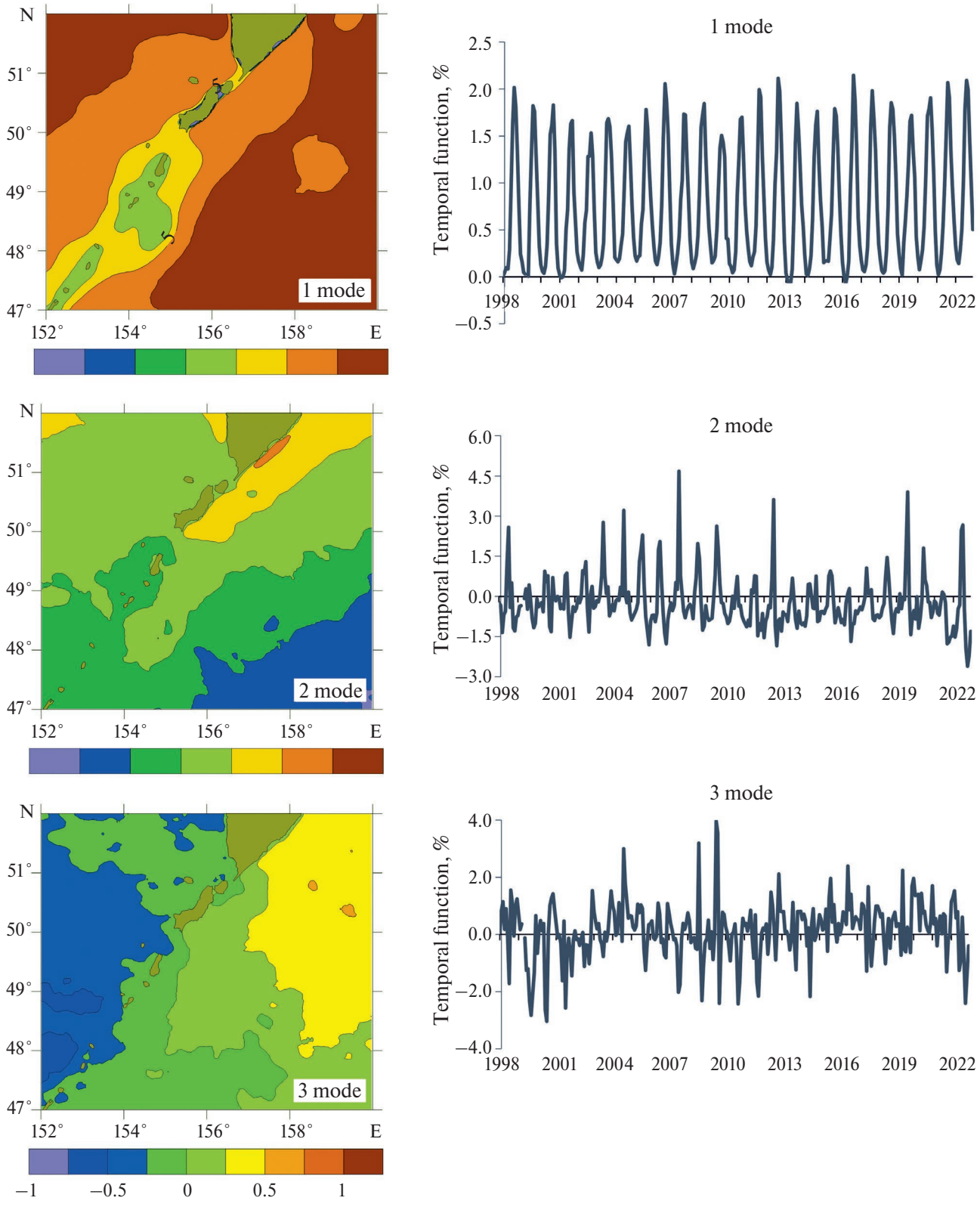

Fig. 8. Spatial distribution (dimensionless) and plots of time functions (in °C) of the first three modes of the SST field decomposition by EOF in the area of the North Kuril Islands.

of the EOF in detail. Let us only note that the time function is well approximated by a combination of annual and semiannual harmonics with amplitudes of 0.9 and 0.2 °C, reaches maximum values in August-September and minimum in February-March. The first mode describes the parameter oscillations, which occur in-phase in the entire region, although with different intensity in the areas characterized by the spatial function.

The second mode reflects the variations of SST which do not fit into the idea of an identical course of the parameter. Therefore, the spatial distribution shows zones with different signs separated by a nodal line near which the contribution of this mode is insignificant. This line passes in the vicinity of the 49th parallel, to the north of which the mode values are positive (up to 1.2 near the southeastern coast of Kamchatka), and to the south — negative (up to –1.1 at the southeastern site).

The averaged curve of the time function has positive values from June to August with a pronounced maximum in July. In other months, the values are negative, with minima in October-November. This means that in summer the second mode gives a correction to the main component, positive in the northern part of the area and negative in the southern areas. In the cold period of the year, the situation is opposite — its contribution is negative in the north and positive in the southern areas.

Significant interannual variations are noticeable in the temporal function of this mode; the 11–year cycle is significantly emphasized, and to a lesser extent — the 6–year cycle, while its annual course is generally preserved. The highest positive values and, consequently, the maximum contribution of the mode to the total SST field, are observed in July 2007, 2012, and 2019. In some years (e.g., 1999 and 2016), the summer maximum is weakened, with values of the time function an order of magnitude smaller than in cases of a pronounced maximum. Negative values are more stable, with extreme minima identified in the fall of 2022 (below –2 °C).

While the second mode gives a zonal correction to the main component, the third mode introduces a meridional correction. Its spatial function took negative values practically over the entire Okhotsk Sea section of the study area. In the NWPO, the nodal line was approximately along the 155th meridian with positive values in the eastern part of the water area and negative values in the western partThe variation of values was from –0.6 to +0.5 °C.

Unlike the first two modes, the time function of the third mode did not have a stable recurring seasonal character. Its averaged values for 1998–2022 for different months of the year were positive in January-June, August and December. In case of positive values of the time function, the positive correction took place in the eastern part of the study area, and the negative correction — in the western part. In case of negative values, the correction acquired the opposite character. The greatest total change in SST due to the contribution of the third mode was observed in July 2009, which amounted to about +2 °C in the eastern part of the basin and –2.5 °C in the western part of the basin.

CONCLUSION

Calculation of averaged SST distributions by seasons has established the main feature of the thermal regime in the area of the North Kuril Islands, expressed in the presence of a permanently existing area with low water temperature values. It covers the coastal water area of the archipelago from Simushir Island to the Fourth Kuril Islands. It covers the coastal water area of the archipelago from Simushir Island to the Fourth Kuril Strait and does not include waters near Shumshu and Paramushir Islands. Thermal indices increase as one moves away from it into both the open ocean and the Sea of Okhotsk. The cold water zone becomes most extensive near Shiashkotan Island, where the temperature in the vicinity of the Shumshu and Paramushir Islands increases. Shiashkotan Island, where second spot is formed near the northern spur of the Vityaz Ridge. This feature emphasizes the key role of the bottom relief in the formation of the cold zone.

Seasonal SST fluctuations are characterized by a distinct annual variations with maximum values in August-September and minimum values in February-March. They are well described by a combination of annual and semiannual harmonics with amplitudes of 4.9 and 1.1 °C, the fluctuations of which decrease in the zone of cold waters and increase as one moves away from the islands to the moribund regions. The interannual variability of the thermal regime is revealed mainly in the modulation of the annual variations with a period of about six years.

In the time functions of the two main modes of the decomposition of the SST field by the EOF in the envelope by summer maxima, cycles with periods of about 11 and six years are manifested. In the spatial structure of the first mode, the area of low values near the Kuril Islands is distinguished. The second mode indicates differences in thermal conditions in the northern and southern parts of the study area, and the third mode — in the waters of the Sea of Okhotsk and the NWPO.

Calculation of linear trend coefficients determined the direction of temperature increase in the whole area at a rate of about 1 °C over 25 years. The warming trend is most noticeable in the adjacent part of the NWPO in summer and to a somewhat lesser extent in the fall.

In the cold spot area, the opposite trend is predominantly observed in winter and spring.

The analysis of the SST fields for 25 years of observations showed that at times significant temperature anomalies exceeding twice the value of the standard deviation can be formed in the area of the North Kuril Islads. In ten cases out of 300, the proportion of the area over which such anomalies were observed was more than 20%, and in four of them — more than 40%. This indicates that deviations of the thermal regime can be large-scale, occur over a significant part of the area and pose a serious threat to the hydrobionts living there. At the same time, cases of anomalously cold conditions clearly prevailed. Such disproportion is very unusual, its physical causes are unclear and require further study.

REFERENCES

1. *Bagrov N.A.* Analiticheskoe predstavlenie posledovatel'nosti meteorologicheskikh polei posredstvom estestvennykh ortogonal'nykh sostavlyayushchikh [Analytical representation of a sequence of meteorological fields by means of natural orthogonal components] // Tr. Tsentral'nogo instituta prognozov. 1959. Issue 74. Pp. 3–24 (in Russian).

2. *Byshev V.I., Figurkin A.L., Anisimov I.M.* Sovremennye klimaticheskie izmeneniya termohalinnoj struktury vod SZTO [Recent climate changes of thermohaline structure in the North-West Pacific] // Izv. TINRO. 2016. Vol. 185. Pp. 215–227. (in Russian).

3. Gidrometeorologiya i gidrohimiya morej. Vol. IX. Ohotskoe more. Vyp. 1. Gidrometeorologicheskie usloviya [Hydrometeorology and hydrochemistry of the seas. Volume IX. The Sea of Okhotsk. Issue 1. Hydrometeorological conditions] / Pod red. F. S. Terzieva i dr. SPb.: Gidrometeoizdat, 1998. 342 p. (in Russian).

4. *Glebova S.Yu., Ustinova E.I., Sorokin Yu.D.* Dolgoperiodnye tendencii v hode atmosfernyh processov i termicheskogo rezhima dal'nevostochnyh morej za poslednij 30-letnij period [Long-period trends in the course of atmospheric processes and thermal regime of the Far Eastern seas over the last 30 years] // Izvestiya TINRO. 2009. Vol. 159. Pp. 285–298. (in Russian).

5. *Zuenko Yu.I., Aseeva N.L, Glebova S.Yu., Gostrenko L.M., Dubinina A.Yu., Dulepova E.P., Zolotov A.O., Loboda S.V., Lysenko A.V., Matveev V.I., Muktepavel L.S., Ovsyannikov E.E., Figurkin A.L., Shatilina T.A.* Sovremennye izmeneniya v ekosisteme Ohotskogo morya (2008–2018) [Modern changes in the ecosystem of the Sea of Okhotsk (2008–2018)] // Izvestiya TINRO. 2019. Vol. 197. Pp. 35–61. DOI: 10.26428/1606-9919-2019-197-35-61

6. *Kantakov G.A.* Okeanograficheskij rezhim tihookeanskogo shel'fa i materikovogo sklona Severnyh Kuril i ego vliyanie na raspredelenie promyslovyh ob"ektov [The oceanographic regime of the Pacific shelf and the continental slope of the North Kuril Islands and its impact on the distribution of fishing facilities] // Promyslov-biologicheskie issledovaniya ryb v tihookeanskih vodah Kuril'skih ostrovov i prilezhashchih rajonah Ohotskogo i Beringova morej v 1992–1998. M.: VNIRO, 2000. Pp. 54–64. (in Russian).

7. *Lozhkin D.M., Shevchenko G.V.* Trendy temperatury poverhnosti Ohotskogo morya i prilegayushchih akvatorij po sputnikovym dannym 1998–2017 [Trends in sea `surface temperature of the Sea of Okhotsk and adjacent water areas according to satellite data 1998–2017] // Issled. Zemli iz kosmosa. 2019. Iss. 1. Pp. 55–61. DOI: 10.31857/S0205-96142019155-61 (in Russian).

8. *Lozhkin D.M., Shevchenko G.V.* Ciklicheskie variacii temperatury poverhnosti Ohotskogo morya i prilegayushchih akvatorij po sputnikovym dannym v 1998–2018 [Cyclic variations of the sea surface temperature of the Sea of Okhotsk and adjacent areas according to satellite data in 1998–2018] // Issled. Zemli iz kosmosa. 2020. Iss. 1. Pp. 44–51. DOI: 10.31857/S0205961420010066 (in Russian).

9. *Novinenko E.G., Shevchenko G.V.* Prostranstvenno-vremennaya izmenchivost' temperatury poverhnosti Ohotskogo morya po sputnikovym dannym [Spatial and temporal variability of the sea surface temperature of the Sea of Okhotsk according to satellite data] // Issled. Zemli iz kosmosa. 2007. Iss. 5. Pp. 50–60 (in Russian).

10. *Rogachev K.A., Shlyk N.V.* Mnogoletnie izmeneniya vihrya vetra i uroven' morya v Kamchatskom techenii [Long-term changes in the wind vortex and sea level in the Kamchatka current] // Okeanologiya. 2005. Vol. 45. Iss. 3. Pp. 339–348. (in Russian).

11. *Rostov I.D., Dmitrieva E.V., Rudyh N.I., Voroncov A.A.* Klimaticheskie izmeneniya termicheskih uslovij okrainnyh morej zapadnoj chasti Tihogo okeana [Climatic changes in the thermal conditions of the marginal seas of the Western Pacific Ocean] // Meteorologiya i gidrologiya. 2020. Iss. 3. Pp. 44–57 (in Russian).

12. *Rostov I.D., Dmitrieva E.V., Rudyh N.I.* Klimaticheskie izmeneniya termicheskih uslovij v tihookeanskoj subarktike v usloviyah sovremennogo global'nogo potepleniya [Climatic changes in thermal conditions in the Pacific Subarctic in the context of modern global warming] // Morskoj gidrofizicheskij zhurnal. 2021. Vol. 37. Iss. 2. Pp. 162–178. https://doi.org/10.22449/0233-7584-2021-2-162-178. (in Russian, English translation).

13. *Rostov I.D., Dmitrieva E.V., Voroncov A.A.* Tendencii klimaticheskih izmenenij termicheskih uslovij pribrezhnyh rajonov Ohotskogo morya za poslednie desyatiletiya [Trends in climatic changes in thermal conditions of the coastal areas of the Sea of Okhotsk in recent decades] // Izvestiya TINRO. 2017. Vol. 191. Pp. 176–195 (in Russian).

14. *Samko E.V., Novikov Ye.V.* Srednemnogoletnyaya geostroficheskaya cirkulyaciya vod prikuril'skogo rajona Tihogo okeana [Average long-term geostrophic water circulation in the Kuril Islands region of the Pacific Ocean] // Okeanologiya. 2004. Vol. 44. Iss. 1. Pp. 5–10. (in Russian, English translation).

15. *Khen G.V., Ustinova E.I., Figurkin A.L., Zuenko Yu.I., Novikov Yu.V., Sorokin Yu.D., Gamanyuk M.V.* Gidrologicheskie usloviya severo-zapadnoj chasti Tihogo okeana i dal'nevostochnyh morej v nachale XXI veka i ozhidaemye tendencii [Hydrological conditions of the Northwestern Pacific Ocean and the Far Eastern seas at the beginning of the XXI century and expected trends] // Voprosy promyslovoj okeanologii. 2004. Iss. 1. Pp. 40–58.

16. *Khen G.V., Basyuk E.O., Sorokin Yu.D., Ustinova E.I., Figurkin A.L.* Termicheskie usloviya na poverkhnosti Beringova i Okhotskogo morei v nachale 21–go veka na fone poluvekovoi izmenchivosti [Surface thermal conditions in the Bering and Okhotsk Seas in the early 21 Century against previous semi-centennial changes] // Izv. TINRO. 2008. Vol. 153. Pp. 254–263 (in Russian).

17. *Khen G.V., Ustinova E.I., Sorokin Yu.D.* Mnogoletnie izmeneniya termicheskikh uslovii na poverkhnosti dal'nevostochnykh morei i SZTO i ikh svyaz' skrupnomasshtabnymi klimaticheskimi protsessami [Long-term changes in thermal conditions on the surface of the Far-Eastern Seas and North-West Pacific and their relationship with large-scale climate processes] // Izv. TINRO. 2020. Vol. 202, Issue 1. Pp. 187–207. DOI: 10.26428/1606-9919-2022-202-187-207 (in Russian).

18. *Tskhai Zh.R., Shevchenko G.V., Lozhkin D.M.* Analiz termicheskikh uslovii v severo-zapadnoi chasti Tikhogo okeana po sputnikovym dannym [Analysis of Thermal Conditions in the Northwest Pacific Ocean from Satellite Data] // Issledovanie Zemli iz kosmosa. 2022. Iss. 1. Pp. 30–37. DOI: 10.31857/S0205961422010079. EDN HRSJAX (in Russian).

19. *Joyce T., Dunworth-Baker J.* Long-term hydrographic variability in the Northwest Pacific Ocean // Geophysical Research Letters. 2003. Vol. 30. Is. 2. P. 043. https://doi.org/10.1029/2002GL015225.

20. *Kono T., Kawasaki Y.* Modification of the western subarctic water by exchange with the Okhotsk Sea // Deep Sea Res. Part I. 1997. Vol. 44. Is. 4. Pp. 689–711.

21. *Ustinova E.* Extreme events in the thermal state of the Far-Eastern Seas and adjacent waters of the Northwestern Pacific // PICES-2021 Virtual Annual Meeting. Book of Abstract. — Victoria, BC, Canada. — 2021. — P. 26.